INTERNATIONAL JOURNAL OF
IJCOE
COASTAL, OFFSHORE &
ENVIRONMENTAL ENGINEERING

Volume 2 | Issue 1 | Apr 2017

www.ijcoe.org **info@ijcoe.org**

www.ijcoe.org

International Journal of Coastal, Offshore & Environmental Engineering (IJCOE)

Vol. 2 / Issue. 1 / Apr 2017

5

International Journal of
Coastal, Offshore
& Environmental
Engineering

ISSN: 2980-8731 (online)

Since 2015

Volume 2 | Issue 1| Apr 2017

IJCOE

Editor-in-Chief: Prof. Hamid S.Bahai

International Journal of
Coastal, Offshore
& Environmental
Engineering
Since 2015
ISSN: 2980-8731 (online)

In The Name of God

Message from the Editor-in-Chief

The IJCOE journal office was established in 2015,and its first issue was published in 2016. TheIJCOE covers a wide range of research in thefields of oceanography & ocean technology, aswell as marine industries & marine engineering.The editorial board of IJCOE consists of nearly130 of the greatest scientists and researchersfrom over 30 countries worldwide, and thejournal's review board comprises 1,000 membersfrom all five continents. The membership andapplication process for joining the editorial andreview boards of this journal is ongoing. IJCOE isa research-academic quarterly journal that haspublication and distribution permissions fromthe Press Organization and permission topublish scientific-research articles from theMinistry of Science, Research, and Technology(MSRT) with an "A" rating. It also holds a "Q1"rating from the ISC institute with an impactfactor (IF) of approximately 0.43 and isconsidered a "core journal" (prestigious andoutstanding journal). IJCOE is an open-accessjournal and allows the download and receipt ofaccepted articles in full text for free. It respectsand adheres to copyright and COPE regulations.The journal's office operates 24/7, providingservices to researchers. In addition to publishinga regular quarterly journal, IJCOE has 16 specialissues on specific topics in preparation. It alsoprovides conditions for publishing specializedbooks, references, and handbooks. Moreover, itis ready to cooperate with the secretariats ofreputable international conferences to publishtheir selected and outstanding articles. IJCOEevaluates, appraises, and publishes books,articles, and the scientific achievements andfindings of esteemed researchers and scientistsworldwide who are innovating and conductingin-depth research in the "important and strategicfield of the maritime technology & Oceanengineering." It welcomes any form of jointcooperation with universities, research institutes,and related research centers at the national,regional, and international levels, and extends ahand for collaboration.

Classification of Editorial Board in IJCOE

- Editor-in-Chief
- Director-in-Chief
- Deputy Editor
- Executive Managers
- English Text Editor
- Technical Editor
- International Editorial Board
- National Editorial Board
- Editorial Board Associate
- Editorial Board Assistant
- Guest Editorial Board
- Advisory Board
- Administrative Coordinator
- Honorary Board Member
- Methodology Advisor

Author Benefits

- Open Access
- Rapid Publication
- Thorough Peer-Review
- No Copyright Constraints
- Coverage by Leading Indexing Services
- Discounts On Article Processing Charges (APC)
- No Space Constraints, No restriction on the maximum length of the papers, number of figures or colors

Aims of IJCOE

Hydrodynamics

Marine equipment

Structural mechanics

Ocean environmental predictions

Stochastic calculations Experimental

Automatic Control of Marine Systems

Scope of IJCOE

Marine Hazards

Ocean Acoustics

Naval Architecture

Ocean Engineering

Coastal Engineering

Marine Meteorology

Marine Earth Sciences

Underwater Technology

Marine Renewable Energy

Polar & Arctic Engineering

Marine Renewable Energy

Marine Geography & Geodesy

Marine Environmental Engineering

Automatic Control of Marine Systems

Hydro Physics & Physical Oceanography

Type of papers

- Case Studies
- Book Reviews
- Review Article
- Letters to the Editor
- Methodology Papers
- Editorials and Commentaries
- Response or Rejoinder Papers
- Perspective or Opinion Papers
- Conceptual or Theoretical Papers
- Meta-Analysis and Systematic Reviews
- Short Communications or Brief Reports
- Research Articles (Original Research Papers)

Scientific Research Journal

Ministry of Science, Research And Technology (MSRT)

Jurnal Ranking 2023: A

Ministry Of Science, Research And Technology (ISC)
Citation Impact 2022: 0.429
Quartile 2022 : Q1
Core Collection

IJCOE is a Member of

- We Respect the Science CIVILICA
- Google Scholar
- Jouroscope
- COPE 20TH ANNIVERSARY 1997-2017 cc BY NC SA
- ISC
- JREF.IR Journals Reference
- DOAJ DIRECTORY OF OPEN ACCESS JOURNALS
- ISSN INTERNATIONAL STANDARD SERIAL NUMBER INTERNATIONAL CENTRE
- Researcher.Life
- doi Crossref EScience Press mEDRA
- iThenticate
- magiran
- OPEN ACCESS
- pistotn
- RG ResearchGate
- Regional Information Center for Science and Technology RICEST
- ScienceGate
- Scilit
- SID
- website.informer.com
- WEBrate

Cantact Us

Office 1 | Research Institute of Meteorology and Atmospheric Science

Address | Tehran, Shahid Kharrazi Highway, Pajoohesh Blvd, Research Institute of Meteorology and Atmospheric Science, Sand and Dust Storm International Research Center (SDS-IRC), No. 13, 1st floor.

Phone | +982144787652

Postal code | 13611-14977

website | www.rimac.ac.ir

Office 2 | Iranian National Institute for Oceanography and Atmospheric Science

Address | Tehran, Dr. Fatemi Gharbi St., Shahid Etemadzade St., No. 3, third floor.

Phone | +982166944873

Postal code | 13389 – 14118

website | www.inio.ac.ir

Email | Info@ijcoe.org

Website | www.ijcoe.org

Follow Us

www.ijcoe.org

INTERNATIONAL JOURNAL OF
IJCOE
COASTAL, OFFSHORE & ENVIRONMENTAL ENGINEERING

Volume & Issue:

Volume 2, Issue 1, April 2017

Number of Articles: 6

Content

INTERNATIONAL JOURNAL OF
COASTAL & OFFSHORE ENGINEERING
IJCOE Vol.2/No. 1/Spring 2017 (1-7)

Available online at: http://ijcoe.org/browse.php?a_code=A-10-37-1&sid=1&slc_lang=en

A Numerical Model of Vortex-Induced Vibration on Marine Risers

Hamed Ashuri[1], Keyvan Sadeghi[2*], Saeid Niazi[3]

[1] MSc, Hormozgan University; Hamedashuri@gmail.com
[2*] Corresponding author: Assistant professor, Buein Zahra Technical University; keyvan.sadeghi@bzte.ac.ir
[3] Assistant professor, Hormozgan University, s.niazi@hormozgan.ac.ir

ARTICLE INFO

Article History:
Received: 10 Sep. 2016
Accepted: 9 Mar. 2017

Keywords:
Vortex-Induced Vibration
RANS Equation
Turbulence Model
Lift Coefficient

ABSTRACT

The Steger and Warming flux vector splitting implicit scheme is used to numerically solve two dimensional Reynolds Averaged Navier–Stokes (RANS) equations governing the vortex induced vibration of a flexible riser laterally supported by a spring and a damper. The *k*–*ε* model is used as turbulence model to simulate the turbulent flow in the wake of the riser. To update the new position of the riser, the lift coefficient obtained from the previous RANS iteration is coupled by the body motion equation. The proposed numerical solution is able to provide fair results in terms of lift coefficient, amplitude of oscillation and the effect of reduced velocity on it. The numerical results are compared with the available experimental and computational data where fairly good agreement even at the lock-in regime has been obtained. Taking wider external boundary, using conservative form of the equations, applying *k*-*ε* turbulence model for the separated flow and finally using the variable time step as the lock–in region approaches, are main features of the proposed numerical model.

1. Introduction

Vortex-induced vibration (VIV) is a vibration due to oscillatory lift force caused by alternating vortex shedding from opposite sides of slender bluff bodies. VIV can have damaging effects on structures when the frequency of vortex shedding is in vicinity of one of the natural frequencies of the structure. VIV can be present in many engineering situations including marine and offshore applications such as in drilling and production risers. Due to its occurrence in diverse engineering applications, VIV has been the subject of extensive experimental and computational research including review articles in [1–5]. In studies of vortex-induced vibration, the physical model is usually a relatively long rigid or elastic cylinder placed normal to an incident uniform flow where the cylinder can vibrate transverse to the flow direction.

For a flexible and/or moving cylinder like a marine riser, the fluid interacts strongly with the riser motion and the vortex shedding frequency is captured by the body frequency over a wider range of flow speed [6]. Such a phenomenon is known as lock-in and the extent of the range of speed depends on the damping and mass of the riser [7]. Figure 1 presents a schematic sketch of three distinct branches obtained in experimental model of Khalak and Williamson [8]. The range of Reynolds number used here is 500–10000 which corresponds to the reduced velocity range of 0.5–10 and is included in the experimental data of [8]. The Steger and Warming [9] implicit factorization scheme is used to solve the RANS equations. The *k*-*ε* two equation turbulence model is used to simulate the turbulent flow in the wake. A similar computational study to duplicate the experimental results of [8] is reported by Wanderley and Levi [7]. The difference between the present numerical model with that of [7] is summarized in Table 1.

Table 1. Comparison of numerical models

	Present Model	Wanderley and Levi [7]
Turbulence Model	*k*-*ε*	Baldwin-Lomax
Numerical ‖Scheme	Steger-Warming	Beam-Warming
Factorization	Approximate	-------
Stretching Parameter	1.02	1.025

The numerical model used here is sufficiently accurate and robust and was able to duplicate experimental results of [8] with a success similar to that achieved by [7], i.e., the Karman's vortex street effects on the lift and drag coefficients and the build-up and top part of the upper branch in Figure 1 were captured.

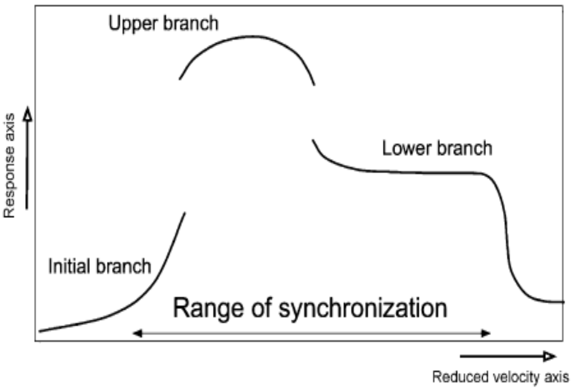

Figure 1. Sketch of three branches response model of Khalak and Willaimson (1996)

2. Governing Equations

The derivation of RANS equations in this section follows that of [7] closely. By breaking down the dependent variables into time averaged and varying parts, and also by using the mass-weighted averaging procedure of Farve [10] the RANS equations are derived. To present a general scheme of RANS equations, we first state them in a 3-D form although the simulations will be carried out in 2-D. Following the mass–weighted averaging procedure of Favre [10] the x-component of RANS equation can be written as follows:

$$\rho\left[\frac{\partial}{\partial x}(\bar{u}^2+\overline{u'^2})+\frac{\partial}{\partial y}(\bar{u}\bar{v}+\overline{u'v'})+\frac{\partial}{\partial z}(\bar{u}\bar{w}+\overline{u'w'})\right]=-\frac{\partial \bar{p}}{\partial x} \quad (1)$$
$$+\mu\left[\frac{\partial^2\bar{u}}{\partial x^2}+\frac{\partial^2\bar{u}}{\partial y^2}+\frac{\partial^2\bar{u}}{\partial z^2}\right]$$

This equation appears to be very similar to the steady-state, x-direction Navier-Stokes equation aside from terms involving the fluctuating velocities. It is conventional to transport these terms to the right-hand side so as to make the left-hand side b consistent with the steady state, Navier-Stokes x-direction equation:

$$\rho\left[\frac{\partial}{\partial x}(\overline{u^2})+\frac{\partial}{\partial y}(\bar{u}\bar{v})+\frac{\partial}{\partial y}(\bar{u}\bar{w})\right]=-\frac{\partial \bar{p}}{\partial x} \quad (2)$$
$$+\mu\left[\frac{\partial\bar{u}}{\partial x}(\mu\frac{\partial\bar{u}}{\partial x}-\rho\overline{u^2})+\frac{\partial\bar{u}}{\partial y}(\mu\frac{\partial\bar{u}}{\partial y}-\rho\overline{u'v'})+\frac{\partial\bar{u}}{\partial z}(\mu\frac{\partial\bar{u}}{\partial y}-\rho\overline{u'w'})\right]$$

The terms that appear in the last bracket of Eq. (1) are called Reynolds Stresses. This designation, while being traditional, is somewhat illogical because the terms in question arise from momentum flow rate terms. These "stresses" are the source that creates the turbulent disturbance of the otherwise steady Navier-Stokes equations. An often-cited form of the RANS equation:

$$\rho\left[\frac{\partial}{\partial x}(\overline{u^2})+\frac{\partial}{\partial y}(\bar{u}\bar{v})+\frac{\partial}{\partial y}(\bar{u}\bar{w})\right]=-\frac{\partial \bar{p}}{\partial x}$$
$$+\mu\left[\frac{\partial^2\bar{u}}{\partial x^2}+\frac{\partial^2\bar{u}}{\partial y^2}+\frac{\partial^2\bar{u}}{\partial z^2}\right]-\left[\frac{\partial}{\partial x}(\overline{\rho u'^2})+\frac{\partial}{\partial y}(\overline{\rho u'v'})+\frac{\partial}{\partial z}(\overline{\rho u'w'})\right]$$

(3)

Here the mass averaged parameters are obtained by following formula:

$$\tilde{f}=\frac{\overline{\rho f}}{\bar{\rho}} \quad (4)$$

The viscous stress tensor $\tilde{\tau}_{ij}$ can be written as follows:

$$\tilde{\tau}_{ij}=\mu\left[\left(\frac{\partial\tilde{u}_i}{\partial x_j}+\frac{\partial\tilde{u}_j}{\partial x_i}\right)-\frac{2}{3}\delta_{ij}\frac{\partial\tilde{u}_k}{\partial x_k}\right] \quad (5)$$

Writing the mean variables and the additional Reynolds stress terms such as indicated in Eq. (6), will yield the continuity and momentum terms of RANS equations.

$$\sigma_{ij}=-\overline{\rho u_i' u_j'} \quad (6)$$

Now, decomposing the components of the equation in two coordinate directions and considering the incompressible, turbulent momentum flow, the RANS equation can be written as follows:

$$\frac{\partial\tilde{u}}{\partial t}+\frac{\partial(\tilde{u}^2+\bar{p}/\rho_\infty)}{\partial x}+\frac{\partial\tilde{u}\tilde{v}}{\partial y}+\frac{\partial\tilde{u}\tilde{w}}{\partial z}-$$
$$\frac{1}{\rho_\infty}\left[\frac{\partial\tilde{\tau}_{xx}}{\partial x}+\frac{\partial\tilde{\tau}_{xy}}{\partial y}+\frac{\partial\tilde{\tau}_{xz}}{\partial z}\right]$$
$$+\frac{1}{\rho_\infty}\left[\frac{\partial\sigma_{xx}}{\partial x}+\frac{\partial\sigma_{xy}}{\partial y}+\frac{\partial\sigma_{xz}}{\partial z}\right]=0 \quad (7)$$

$$\frac{\partial\tilde{v}}{\partial t}+\frac{\partial\tilde{u}\tilde{v}}{\partial x}+\frac{\partial(\tilde{v}^2+\bar{p}/\rho_\infty)}{\partial y}+\frac{\partial\tilde{v}\tilde{w}}{\partial z}-$$
$$\frac{1}{\rho_\infty}\left[\frac{\partial\tilde{\tau}_{xy}}{\partial x}+\frac{\partial\tilde{\tau}_{yy}}{\partial y}+\frac{\partial\tilde{\tau}_{yz}}{\partial z}\right]$$
$$+\frac{1}{\rho_\infty}\left[\frac{\partial\sigma_{xy}}{\partial x}+\frac{\partial\sigma_{yy}}{\partial y}+\frac{\partial\sigma_{yz}}{\partial z}\right]=0 \quad (8)$$

$$\frac{\partial\tilde{w}}{\partial t}+\frac{\partial\tilde{u}\tilde{w}}{\partial x}+\frac{\partial\tilde{v}\tilde{w}}{\partial y}+\frac{\partial(\tilde{w}^2+\bar{p}/\rho_\infty)}{\partial z}-$$
$$\frac{1}{\rho_\infty}\left[\frac{\partial\tilde{\tau}_{xz}}{\partial x}+\frac{\partial\tilde{\tau}_{yz}}{\partial y}+\frac{\partial\tilde{\tau}_{zz}}{\partial z}\right]$$
$$+\frac{1}{\rho_\infty}\left[\frac{\partial\sigma_{xz}}{\partial x}+\frac{\partial\sigma_{yz}}{\partial y}+\frac{\partial\sigma_{zz}}{\partial z}\right]=0 \quad (9)$$

To solve the RANS governing equations, the approximate factorization method, which is a stable approach in 2-D problems, is implemented. To estimate the convective terms and diffusion terms, the forward central difference and second order central difference schemes are used, respectively. Writing the RANS equation in 2-D curvilinear coordinates and in the conservative and dimensionless form will result in a more convenient and straight forwarded shape of the equation as follows:

$$Q_t + (E_e - E_v)_\xi + (F_e - F_v)_\eta = 0 \tag{10}$$

where Q is the unknown vector, E and F are the flux vectors, and the subscript "*v*" is used to denote the viscous flux vectors. The transformed form of the vectors are presented as follows:

$$Q = \frac{1}{J}\begin{Bmatrix} p \\ u \\ v \end{Bmatrix}, E_e = \frac{1}{J}\begin{Bmatrix} pU \\ uU + p\xi_x \\ vU + p\xi_y \end{Bmatrix}, F_e = \frac{1}{J}\begin{Bmatrix} pV \\ uV + p\eta_x \\ vV + p\eta_y \end{Bmatrix} \tag{11}$$

$$E_v = \frac{1}{J}\left(\frac{1}{Re} + \mu_t\right)\begin{Bmatrix} 0 \\ A_1 u_\xi + A_2 u_\eta + A_3 v_\xi + A_4 v_\eta \\ A_3 u_\xi + A_5 u_\eta + A_6 v_\xi + A_7 v_\eta \end{Bmatrix}$$

$$F_v = \frac{1}{J}\left(\frac{1}{Re} + \mu_t\right)\begin{Bmatrix} 0 \\ A_2 u_\xi + A_{10} u_\eta + A_5 v_\xi + A_{11} v_\eta \\ A_4 u_\xi + A_{11} u_\eta + A_7 v_\xi + A_{12} v_\eta \end{Bmatrix} \tag{12}$$

$$\text{Re} = \frac{\rho_\infty U_\infty d}{\mu_\infty}$$

$$U = \xi_t + u\xi_x + v\xi_y \tag{13}$$

$$V = \eta_t + u\eta_x + v\eta_y$$

$$J = \xi_x \eta_y - \eta_x \xi_y$$

$$A_1 = \frac{4}{3}\xi_x^2 + \xi_y^2 \qquad A_6 = \xi_x^2 + \frac{4}{3}\xi_y^2$$

$$A_2 = \frac{4}{3}\xi_x\eta_x + \eta_y\xi_y \qquad A_7 = \eta_x\xi_y + \frac{4}{3}\eta_y\xi_y$$

$$A_3 = \frac{\xi_x\xi_y}{3} \qquad A_{10} = \frac{4}{3}\eta_x^2 + \eta_y^2$$

$$A_4 = \eta_x\xi_y - \frac{2}{3}\eta_y\xi_x \qquad A_{11} = \frac{\eta_x\eta_y}{3}$$

$$A_5 = \xi_x\eta_y - \frac{2}{3}\eta_x\xi_y \qquad A_{12} = \eta_x^2 + \frac{4}{3}\eta_y^2 \tag{14}$$

Wanderley and Levi [7] used Baldwin-Lomax turbulent model to calculate the dynamic viscosity of modeled system. Here, the *k–ε* model [11], which is a two–equation turbulence model is used. The zero–equation models lack generality although they need minimum computer time, while two–equation models, have less limitations. As the boundary layer becomes separated, the zero–equation models are no longer relevant. As indicated in [12], the shear stress has qualitatively the same turbulent structure when it is detached as it is attached and the length scale is the height of the separated region. Here using this assumption, the *k–ε* model is based on eddy–viscosity concept given by:

$$v_t = C_\mu \frac{K^2}{\varepsilon} \tag{15}$$

where *Cμ* is a constant of dynamic turbulence and *K* and ε are obtained from differential equations representing transport of turbulence kinetic energy *K*, and the rate of dissipation *ε*. The transport equations are:

$$\bar{u}\frac{\partial K}{\partial x} + \bar{v}\frac{\partial Y}{\partial y} =$$

$$\frac{\partial}{\partial y}\left(\frac{\upsilon_t}{\sigma_k}\frac{\partial K}{\partial y}\right) + \upsilon_t\left(\frac{\partial \bar{u}}{\partial y}\right)^2 - \varepsilon \tag{16}$$

$$\bar{u}\frac{\partial \varepsilon}{\partial x} + \bar{v}\frac{\partial \varepsilon}{\partial y} = \frac{\partial}{\partial y}\left(\frac{\upsilon_t}{\sigma_c}\frac{\partial \varepsilon}{\partial y}\right) +$$

$$C_{\varepsilon 1}\frac{\varepsilon}{K}\upsilon_t\left(\frac{\partial \bar{u}}{\partial y}\right)^2 - C_{\varepsilon 2}\frac{\varepsilon^2}{K} \tag{17}$$

The three terms on the right hand side of Eq. (16), are turbulent diffusion, turbulent energy production and viscous dissipation, respectively. The values of constants in the equations are given by [11]: *Cμ*=0.09*, Cε₁*=1.44*, Cε₂*=1.92, *σk*=1.0, *σc*=1.3.

Considering three conditions of initial, boundary of the body surface and free stream boundary given in Eq. (18):

$$u = 1 \qquad v = 0 \qquad p = 1/M_\infty^2$$

$$u = 0 \qquad v = \dot{y} \qquad \partial p/\partial \eta = 0$$

$$u = 1 \qquad v = 0 \qquad p = 1/M_\infty^2$$

$$M_\infty = \textit{practical range for incompressible flow} \tag{18}$$

The Eq. (11) is solved to obtain the flow variables. For the body motion equation, the dimensionless form of the Newton's second law for a cylinder can be written as follows:

$$\ddot{y} + C_\zeta \dot{y} + C_K y = \frac{C_L(Re)}{2C_\mu} \tag{19}$$

Where

$$C_\mu = \frac{m}{\rho D^2}, \quad C_K = \frac{4\pi^2}{U_r^2},$$

$$C_\zeta = \frac{4\pi\zeta}{U_r}, \quad U_r = \frac{U}{f_n d}$$

and subscripts *L*, *k* and *ζ* are used to denote lift, stiffness and damping coefficients, respectively, and $y, \dot{y}, \ddot{y}$ are displacement, velocity and acceleration of the riser. The initial conditions are:

$$y(0) = 0, \quad \dot{y}(0) = 0 \tag{20}$$

3. Numerical formulation

A simple algebraic grid generator method (using geometrical progression) is used to generate the computational space around the riser. To capture more information at area adjacent to the wall, the stretching parameter of q=1.02 is used. In [7] this parameter is equal to 1.025. Then the RANS and body motion equations were solved simultaneously, to obtain C_L and in turn the position of riser. To obtaining the C_L coefficient an integration of pressure and skin friction distribution around the riser surface is conducted. The pressure distribution is obtained in the previous RANS formulation. The governing equations were solved as follows:

3.1. RANS equation

Eq.(10) can be written in the implicit form as follows:

$$\frac{Q^{n+1}-Q^{n}}{\Delta\tau}+\left(\frac{\partial E}{\partial\xi}\right)^{n+1}+\left(\frac{\partial F}{\partial\eta}\right)^{n+1}$$
$$-\left(\frac{\partial E_{v}}{\partial\xi}\right)^{n+1}-\left(\frac{\partial F_{v}}{\partial\eta}\right)^{n+1}=0 \qquad (21)$$

Since the scheme of solution is implicit, a linearization procedure is applied to the RANS equation. The linearization can yield efficient and more accurate results. So, a linearization process was applied on RANS equations in present study. Using the Taylor series, the viscous and inviscid flux vectors appeared in the left hand side of Eq. (21), can be written based on the Jacobin matrices of *A, B, A_v* and *B_v* (gradients of flux vectors with respect to the variable vector, *Q*) in the following form:

$$\frac{\Delta Q}{\Delta\tau}+\frac{\partial}{\partial\xi}\left(E^{n}+A\Delta Q\right)+\frac{\partial}{\partial\eta}(F^{n}+B\Delta Q)$$
$$-\frac{\partial}{\partial\xi}\left(E_{v}{}^{n}+A_{v}\Delta Q\right)$$
$$-\frac{\partial}{\partial\eta}(F_{v}{}^{n}+B_{v}\Delta Q)=0 \qquad (22)$$

which can be rewritten as follows:

$$\left\{I+\Delta\tau\left[\frac{\partial}{\partial\xi}(A)+\frac{\partial}{\partial\eta}(B)-\frac{\partial}{\partial\xi}(A_{v})-\frac{\partial}{\partial\eta}(B_{v})\right]\right\}\Delta Q=$$
$$-\Delta\tau\left[\frac{\partial E^{n}}{\partial\xi}+\frac{\partial F^{n}}{\partial\eta}-\frac{\partial E_{v}^{n}}{\partial\xi}-\frac{\partial F_{v}^{n}}{\partial\eta}\right] \qquad (23)$$

where *I* is the identity matrix. To increase the efficiency of solution of Eq.(23), the approximate factorization was applied. This procedure has reduced the process time of the developed code considerably. It converts the block penta-diagonal system of equations to a block three-diagonal system, which is more efficient and has potential to prevent expensive mathematical computations. Approximate factorization may create some instability in 3-D problems and may need artificial dissipation but it is quite stable for 2-D problems. In addition by splitting the Jacobin matrices based on their eigenvalues, the following two step form of equation can be obtained:

$$\left[I+\Delta\tau\frac{\partial}{\partial\xi}\left(A^{+}+A^{-}\right)-\Delta\tau\frac{\partial A_{v}}{\partial\xi}\right]\Delta Q^{*}=$$
$$-\Delta\tau\left[\frac{\partial}{\partial\xi}\left(E^{+}+E^{-}\right)+\frac{\partial}{\partial\eta}\left(F^{+}+F^{-}\right)-\frac{\partial E_{v}}{\partial\xi}-\frac{\partial F_{v}}{\partial\eta}\right] \qquad (24)$$

And

$$\left[I+\Delta\tau\frac{\partial}{\partial\eta}\left(B^{+}+B^{-}\right)-\Delta\tau\frac{\partial B_{v}}{\partial\eta}\right]\Delta Q=\Delta Q^{*} \qquad (25)$$

Simplifying the above equations and introducing the central difference approximation to inviscid terms, the compact forms of equations can be written as follows:

$$CAM=-\left[\frac{\Delta\tau}{\Delta\xi}A_{i-1j}^{+}+\frac{\Delta\tau}{2\Delta\xi^{2}}\hat{r}_{i-1j}R_{i-1j}\right]$$

$$CA=\left[I+\frac{\Delta\tau}{\Delta\xi}\left(A_{ij}^{+}+A^{-}{}_{ij}\right)+\frac{\Delta\tau}{2\Delta\xi^{2}}\hat{r}_{ij}R_{ij}\right]$$

$$CAP=\left[\frac{\Delta\tau}{\Delta\xi}A_{i+1j}^{-}-\frac{\Delta\tau}{2\Delta\xi^{2}}\hat{r}_{i+1j}R_{i+1j}\right]$$

$$CBM=-\left[\frac{\Delta\tau}{\Delta\eta}B_{ij-1}^{+}+\frac{\Delta\tau}{2\Delta\eta^{2}}\hat{s}_{ij-1}S_{ij-1}\right]$$

$$CB=\left[I+\frac{\Delta\tau}{\Delta\eta}\left(B_{ij}^{+}-B_{ij}^{-}\right)+\frac{\Delta\tau}{2\Delta\eta^{2}}\hat{s}_{ij}S_{ij}\right]$$

$$CBP=\left[\frac{\Delta\tau}{\Delta\eta}B_{ij+1}^{-}-\frac{\Delta\tau}{2\Delta\eta^{2}}\hat{s}_{ij+1}S_{ij+1}\right]$$

$$RHS=-\Delta\tau\left\{\begin{array}{l}\frac{1}{\Delta\xi}\left(E_{ij}^{+}-E_{i-1j}^{+}+E_{i+1j}^{-}-E_{ij}^{-}\right)+\frac{1}{\Delta\xi}\left(F_{ij}^{+}-F_{ij-1}^{+}+F_{ij+1}^{-}-F_{ij}^{-}\right)\\-\frac{1}{2\Delta\xi^{2}}\left[\hat{e}_{i+1j}\hat{E}_{i+1j}-\hat{e}_{ij}\hat{E}_{ij}+\hat{e}_{i-1j}\hat{E}_{i-1j}\right]\\-\frac{1}{2\Delta\eta^{2}}\left[\hat{f}_{ij+1}\hat{F}_{ij+1}-\hat{f}_{ij}\hat{F}_{ij}+\hat{f}_{ij-1}\hat{F}_{ij-1}\right]\end{array}\right\}$$

where *r, s, e, f* and corresponding capital letters, are functions of constants of Eqs. (24-25). Finally, by the Steger and Warming implicit scheme the RANS equations can be written as the following two equations:

$$CAM_{ij}\Delta Q_{i-1j}{}^{*}+CA_{ij}\Delta Q_{ij}{}^{*}+CAP_{ij}\Delta Q^{*}{}_{i+1j}=RHS_{ij} \qquad (26)$$

$$CBM_{ij}\Delta Q_{ij-1}+CB_{ij}\Delta Q_{ij}+CBP_{ij+1}\Delta Q_{ij+1}=\Delta Q^{*}{}_{ij} \qquad (27)$$

3.2. Body motion equation

To solve the body motion equation, two explicit methods were used. From Eq.(19), the acceleration term can simply be written as:

$$\ddot{y}^{n}=\frac{C_{L}^{n}}{2C_{\mu}}-C_{\zeta}\dot{y}^{n}-C_{K}y^{n} \qquad (28)$$

Applying the Lax–Wendroff and Euler methods, the position and velocity of riser can be obtained as follows:

$$\dot{y}^{n+1}=\dot{y}^{n}+\ddot{y}^{n}\Delta t \qquad (29)$$

$$y^{n+1}=y^{n}+\dot{y}^{n}\Delta t+\frac{1}{2}\ddot{y}^{n}\Delta t^{2} \qquad (30)$$

4. Results and Discussion

Results of the work and discussions are presented here. First, the laminar flow results for *Re=100* are compared with other results presented in the literature. Fig 2 shows the generated grid in the physical domain. In order to compare the results with those of Wanderley and Levi [7] a distance to free stream equal to 120 times of cylinder diameter is considered. Although this configuration increases the data points and the computational time, it ensures capturing the properties of vortices in long distances and all possible regions. Table 2 compares results of the present numerical model with other numerical and experimental results in the literature for the lift coefficient. The higher value of lift coefficient obtained in the present model, could be related to the special finite difference scheme used here. However, the main reason of overestimation of C_L needs more investigations in future works.

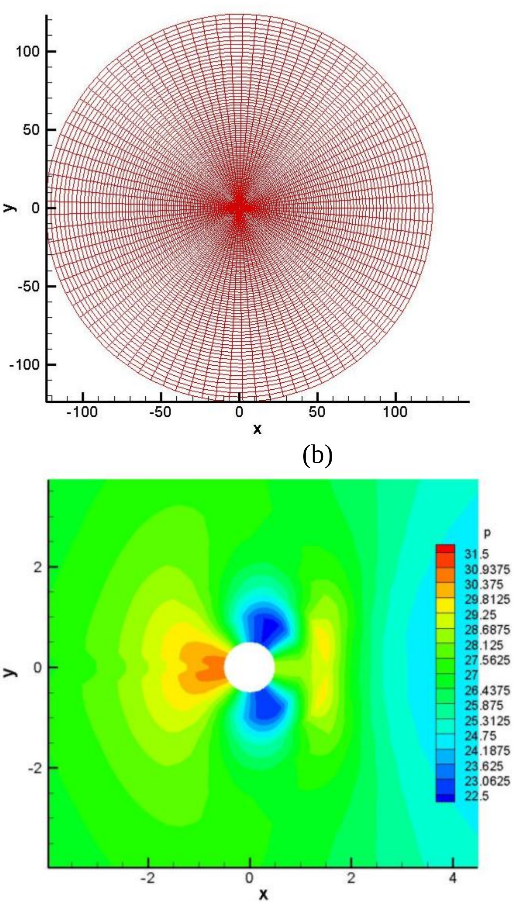
(a)

(b)

Fig. 2 (a): Computational grid in the physical domain. (b): Pressure contours around a circular cylinder for Re=100;

The present model, failed to improve the computation time. The time required for computation of eigenvalues of Jacobin matrices in the Steger–Warming formulation, may be the main reason for the high computational time.

Figure 3 shows the variation of lift force as a function of time at *Re=100*. As can be seen, numerical modeling of the phenomenon is able to present the real picture of the flow physics, since the oscillation in lift force is caused by the variation of pressure in effect of alternating vortex shedding in the wake of the riser. Fig. 4 shows the alternating nature of the vortices in four distinct time steps at *Re=100*. The well-known vortex street of Karman is quite obvious at this figure.

Table 2. Comparison between results obtained by the present work and other numerical and experimental data

Reference	Trriton [15] (dt=0.005)	Herfjord [14]	J.B. Wanderley [7]	Present study (dt=0.004)
Model type	experimental	Finite element	Finite difference (Beam-Warming)	Finite difference (Steger - Warming)
Reynolds no	100	100	100	100
Lift coefficient	0.34	0.34	0.313	0.37

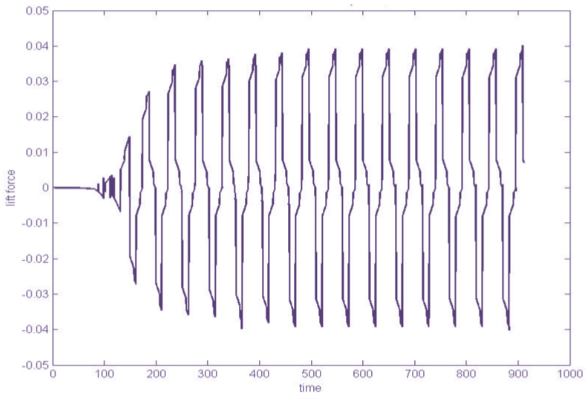

Fig. 3 Time variation of lift force at Re=100

After the accuracy of the model is verified at *Re=100*, the modeling was generalized to other Reynolds numbers. The Reynolds numbers used in the present study are in the range of 500 to 10000 which are proportional to the reduced velocity in the range of 0.5 to 10. The mass and damper coefficients used here, were $C\mu=1.88$ and $\zeta=5.42\times10\text{-}3$, which are the same coefficients used in [7] and [8]. Fig. 5 shows results obtained for the transversal displacement of the vibrating circular cylinder as a function of time. The time is traced in two states, one in the build-up of the upper branch and another at the top of the upper branch Khalak and Williamson [8]. Two values of reduced velocities of *Ur=4.5* in Fig. 5a and *Ur=6.5* in Fig. 5b correspond to the build-up and top part of the upper branch, respectively. The main reason that the lower branch in fig. 1 was not captured at present model may be related to the 2-D modeling using RANS equations, while the lower branch has been obtained in experimental model of Khalak and Williamson [8] which is 3-D.

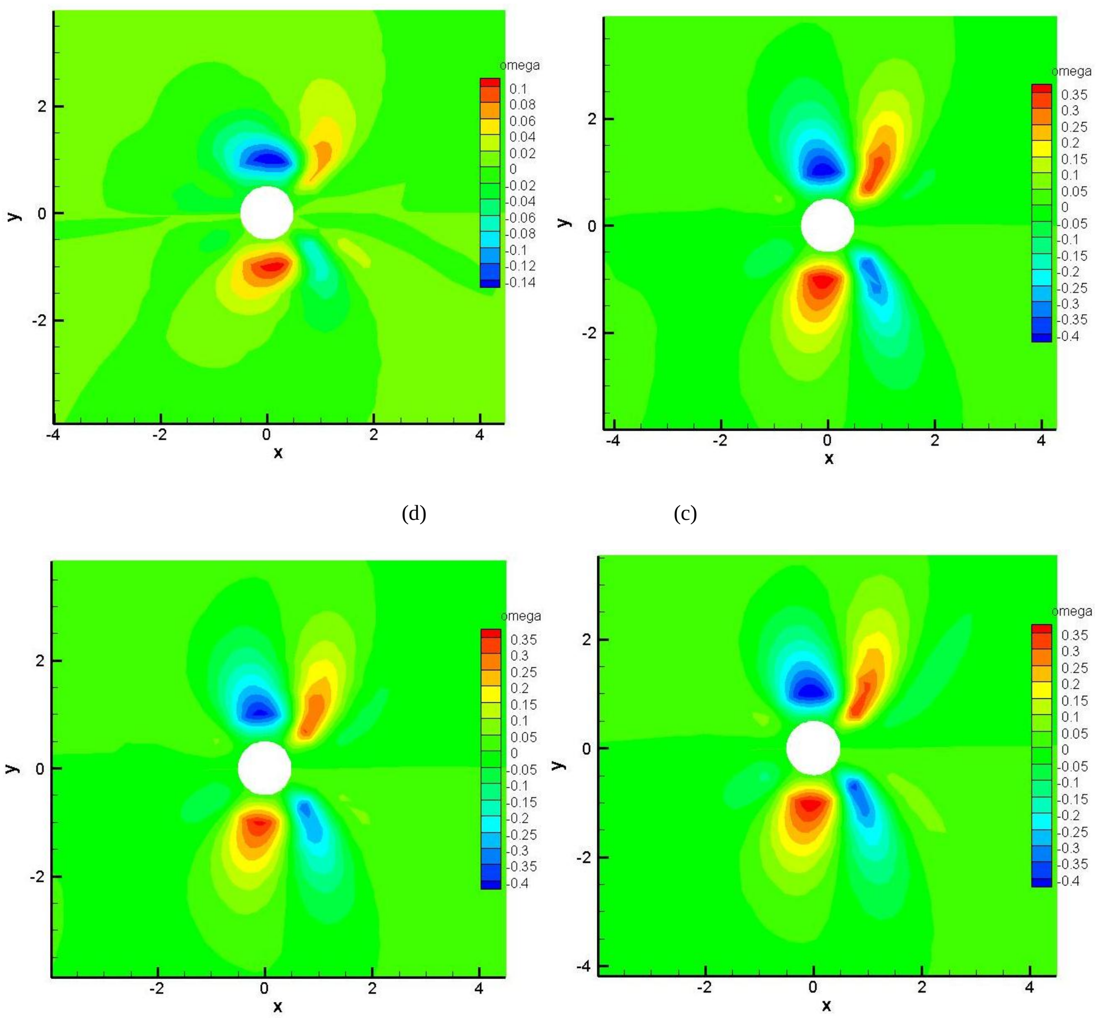
(a) (b)

(d) (c)

Fig. 4 Vortex strength contours at Re=100 in four time steps: (a) 100, (b) 500, (c) 1000, (d) 5000

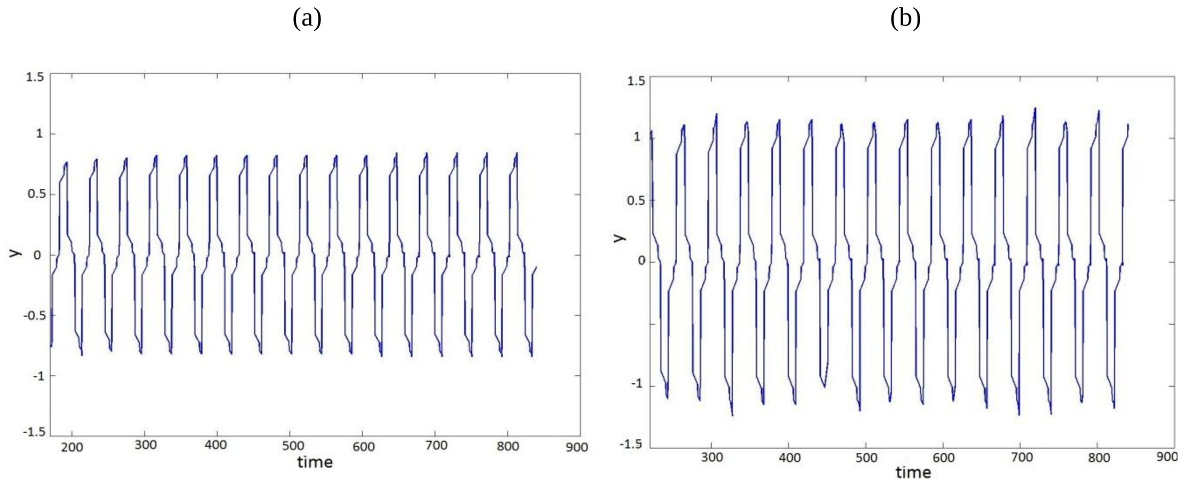
(a) (b)

Fig. 5 Transversal displacement of the riser for (a) Ur=4.5; (b) Ur=6.5.

The main reason the displacement is greater for U_r=6.5 than U_r=4.5 is that U_r=6.5 is in the lock–in region, i.e. the region of top part of upper branch in Figure 1, where the synchronization of frequencies occurs. Figure 6 shows the spectral analysis of displacements for U_r=6.5. As seen, the main component of period of displacements is lied on T=39.81s which justify entering riser to lock–in area at that reduced velocity, since this time period is very close to the natural period of riser displacement (T_n=40s). The features presented here are in close agreement with those presented in Khalak, and Williamson [8].

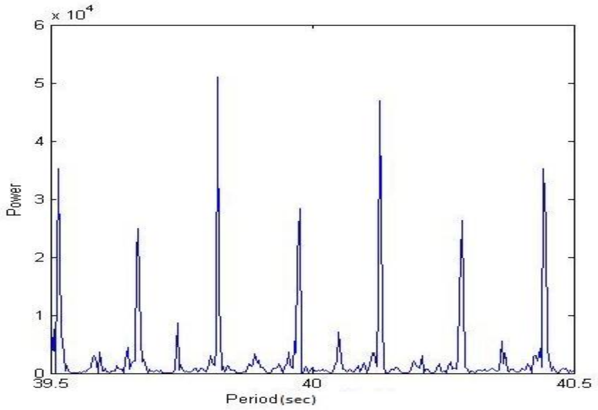

Fig. 6 Spectral analysis of riser displacement, U_r=6.5 (Re=6500)

5. Conclusions

Vortex-Induced vibration is a major concern in offshore oil and gas industry. This phenomenon can cause considerable damage to production lines. Here, a numerical code was developed to capture the vibration ranges of the risers and the comparison of the results show that the finite difference method can be considered as an efficient model tool to simulation of riser dynamics. Is is also indicated that the regime of so called the riser wake can also be captured using the present finite difference method.

First, the results were obtained at *Re=100,* and compared by data available in the literature. Then the solution was generalized to other *Re* (or *Ur*) values. The present mathematical model and respective numerical formulation were able to capture the upper branch of the amplitudes of oscillation reported in Khalak, and Williamson [8]. The lower branch obtained in the present investigation did not agree with the experimental data. To modeling this part of riser oscillation, it is needed to more robust models such 3-D ones to obtain an accurate results for lower branch regime.

The main features of present numerical investigation are:

- Using the *k-ε* turbulent model which is more suitable for separated flows.
- Formulating the conservative form of governing equations
- Applying the approximate factorization to increase the efficiency of solution.

Further investigations can include studying the problem with other turbulence models in CFD. Using the three-dimensional simulation and considering the more complicated geometries of the riser using overlapping Chimera Multi-block grids Houzeaux and Codina [13].

6. References

1- Griffin, O.M., and Ramberg, S.E., (1982), *Some recent studies of vortex shedding with application to marine tubular sand risers*. ASME Journal of Energy Resource Technology Vol.104, p.2–13.

2- Bearman, P.W., (1984), *Vortex shedding from oscillating bluff bodies*. Annual Review of Fluid Mechanics Vol.16, p.195–222.

3- Parkinson, G., (1989), *Phenomena and modeling of flow-induced vibrations of bluff bodies*. Progression Aerospace Sciences Vol.26, p.169–224.

4- Sarpkaya, T., (2004), *A critical review of the intrinsic nature of vortex-induced vibrations*, Journal of Fluids and Structures 1Vol.9, p.389–447.

5- Williamson, C.H.K., and Govardhan, R., (2004), *Vortex-induced vibrations*, Annual Review of Fluid Mechanics, Vol.36, p.413–455.

6- Bearman, P.W., (2000), *Developments in Vortex Shedding Research, Workshop on Vortex-Induced Vibrations of Offshore Structures*. Sao Paulo, Brazil.

7- Wanderley J.B., and Levi, C., (2005), *Vortex induced loads on marine risers*, Ocean Engineering Vol.32, p.1281–1295.

8- Khalak, A., and Williamson, C.H.K., (1996) *Dynamics of a hydroelastic cylinder with very low mass and damping*. Journal of Fluids and Structures, Vol.10, p.455–472.

9- Steger, J.L., and Warming, R.F, (1979), *Flux vector splitting of invicid gas dynamic equations with application to finite difference method*. NASA. TM-78605.

10- Favre, A., (1965) *Equations des gaz turbulents compressibles*: 1 Formes Ge´ne´rales. Journal of Mechanics, Vol.4, p.361–390.

11- Jones W.P., and Launder, B.E., (1997), *The prediction of relaminarization with a two-equation model of turbulence*, International Journal of Heat and Mass Transfer, Vol.15, p.301-314.

12- Goldberg, U.C., (1986), S*eparated flow treatment with a new turbulence model*, AIAA Journal, Vol.24(10), p. 1711-1713.

13- Houzeaux, G., and Codina, R., (2003), *A chimera method on a Dirichlet/Neumann (Robin) coupling for the Navier—Stokes equations*. Computational Methods Application and Mechanical Engineering, Vol.192, p.3343–3377.

14- Herfjord, K., (1995), *A study of two-dimensional separated flow by a combination of the finite element method and Navier–Stokes Equations*, Dr. Eng. Theses, The Norwegian Institute of Technology, Trondheim, Norway.

15- Tritton, D.J., (1959), *Experiments on the flow past a circular cylinder at low Reynolds number*, Journal of Fluid Mechanics, Vol.6, p.

INTERNATIONAL JOURNAL OF
COASTAL & OFFSHORE ENGINEERING

IJCOE Vol.2/No. 1/Spring 2017 (9-16)

Available online at: http://ijcoe.org/browse.php?a_code=A-10-49-1&sid=1&slc_lang=en

The Effect of Shifting Natural Frequency on the Reduction of Vortex-Induced Vibrations of Marine Risers

Younes Komachi[1], Said Mazaheri[2]*, Mohammad Reza Tabeshpour[3]

[1] *Ph.D. Student, National Institute for Oceanography; y_komachi@yahoo.com*
[2*] *Corresponding author: Assistant Professor, National Institute for Oceanography; said.mazaheri@inio.ac.ir*
[3]*Assistant Professor, Mechanical Engineering Department, Center of Excellence in Hydrodynamics and Dynamics of Marine Vehicles, Sharif University of Technology, Tehran, Iran; tabeshpour@sharif.edu*

ARTICLE INFO

Article History:
Received: 30 Apr. 2016
Accepted: 9 Mar. 2017

Keywords:
VIV
Wake Oscillator Model
Finite Element Method
Shifting Frequency

ABSTRACT

Many procedures suggest for reduction of responses of riser to Vortex Induced Vibrations (VIV). Natural frequencies of marine risers is an important parameter that can affect the responses of riser to VIV. Change of riser properties such as top tension and bending stiffness can alter natural frequencies. In this study effects of riser specifications on the responses and fatigue damage of marine risers were investigated analytically and numerically. For numerically analysis 2D wake-structure coupled model is used for modeling of VIV of riser in two directions of Cross Flow (CF) and In Line (IL). The wake dynamics, including IL and CF vibrations, is represented using a pair of non-linear Van der Pol equations that solved using modified Euler method. The Palmgren–Miner Rule is used for evaluation of fatigue damage. Riser of Amir-Kabir semisubmersible placed in Caspian sea is used for case study. Because VIV is self-limiting, it is showed that lower modes have lower curvature, that in some cases this is lead to lesser stress and also fatigue damage. The results show that for tension dominant modes of vibration, natural frequencies was increased with top tension and for a certain Strouhal frequency, dominant modes of vibration was reduced which leads to reduction of stress and fatigue damage. The results show that stress and fatigue damage increased with module of elasticity of riser and reduction of this leads to reducing of stress and fatigue damage. Therefore suitable procedure for reduction of VIV responses of riser should be selected based on the current velocity.

1. Introduction

The Vortex Induced Vibration (VIV) of risers subjected to currents has been a serious concern for ocean researchers and engineers and if effects of this condition not properly mitigated it imposes high additional costs and risks on projects. When fluids flow around slender marine structures, change in the downstream pressure, caused vibration that is named Vortex Induced Vibration. When vortex shedding frequency coincide with one of the structures natural frequencies, the lock-in situation take place and riser vibrate with this natural frequency.

Reduction of VIV amplitude is a method that reduces stresses and fatigue damage which can be achieved using different ways such as increasing structural damping, avoiding resonance and manipulate the wake. Damping can be increased by various means, such as permit scraping between structural elements, use of composite materials, and materials with high internal damping, use of external dampers and etc. For avoiding resonance, the natural frequency does not coincide with the vortex shedding frequency. Many methods have been proposed in order to manipulate the wake flows behind circular cylinders and suppress VIV responses, which are classified as passive, active open-loop and active closed loop controls (Gad-el-Hak and Bushnell [1]; Choi et al. [2]; Gad-el-Hak [3]). During the past 20 years, passive control methods have been further developed, such as helical strake (Zhou et al. [4]), surface protrusions (Shih et al. [5]), shrouds (Zdravkovich [6]), splitter plate (Hwang et al. [7]), rear-wake stabilizer (Eisenlohr and Eckelmann [8]), and small rods (Zhao et al. [9]; Zhao et al. [10]). Geometric modifications of cylinder wall are the main methods for these passive controls, which inevitably increase the mass ratio and sometimes increase the drag coefficient (e.g., helical strake). Therefore, few of them are applied on a large scale in practice.

Recently some studies was performed on the effects of riser structural properties on the VIV responses. The applied top tension and also bending stiffness may significantly affect the order of CF and IL dominant harmonics, collision avoidance (among adjacent risers) and vibration suppression and can be considered as an efficient method for the control of riser statics and dynamics. Sanaati and Kato [11] present the experimental results of a study on the effects of pre-tension and axial stiffness on VIV of a horizontally mounted flexible cylinder. They showed that high pre-tension, which reduces vibration amplitude, can significantly raise the lift coefficient. They also observed that the lock-in bandwidth of amplitude response narrowed with increase in pre-tension, whereas, it broadened with axial stiffness. In addition, high applied pre-tensions delay the excitation of higher modal frequencies compared to lower pre-tensions within the same range of flow velocities. Chen et al. [12] examined effects of axially varying structural parameters, i.e. the effective tension and bending stiffness, on the dynamic characteristics and VIV of slender riser. They show that axially varying structural parameters can efficiently change the modal wave length as well as the modal displacement. The vibration amplitude of riser VIV response is influenced by the complex effect of factors involving the axial tension, bending stiffness and modal wave length. Generally speaking, for lower modes the response amplitude is larger at the axial position where the tension is smaller, whereas for higher modes the response amplitude is larger at the axial position where the bending stiffness is lower. A recent study by Lee and Gerretsen [13] showed the importance of the effect of axial stiffness on tension change and VIV motion amplitude. Lee and Allen [14] concluded that top tension and structural stiffness can have a significant impact on vibration frequencies and lock-in bandwidth. They concluded that bending-dominated cylinders have a slight increase in vibration frequency after an abrupt rise to their first lock-in frequency because the motion of the structure takes control of the shedding process. Moreover, for a tension-dominated cylinder, they concluded that there is a significant rise to the vibration frequency in each lock-in. Srinil [15] performed numerical simulations to analyze and predict the VIV of variable-tension on vertical flexible risers in linearly sheared currents. In his simulations, he emphasized the effects of tension and sheared flow on the amplitude response and multimodal VIV.

Shifting the frequencies of riser can be used to reduction of responses of riser to VIV. The present paper studied the effects of riser properties such as top tension and module of elasticity on the VIV responses of deepwater marine risers. Relation of stress and fatigue damage with these parameters is obtained analytically which can be used to better understanding of effect of shifting frequency on the VIV response of riser and selection of suitable procedure for reduction of stress and fatigue damage.

2. Formulation

Relation of stress and fatigue damage with riser structural properties (top tension and bending stiffness) obtained as follow. For a linear S-N curve in log-log scale, the expected fatigue damage per unit time can be expressed as:

$$D = \frac{n_i}{\bar{a}} \int_0^{\infty} \sigma^m f_S(\sigma)\,\mathrm{d}\sigma = \frac{n_i}{\bar{a}} E\left[\sigma^m\right] \qquad (1)$$

where $\bar{a}$ and m are the scale parameter and the slope parameter of S-N curve, respectively, σ is stress, n_i is number of stress cycles at stress range, and $f_S(\sigma)$ is the Probability Density Function (PDF) for the stress cycles. The expected fatigue damage is hence directly related to the mth order moment, $E\left[\sigma^m\right]$ of the stress cycle PDF.

At lock-in condition response frequency will be close to vortex shedding frequency and the fatigue damage can be related directly to current velocity [16]. The damage proportionality relationship is obtained as follow:

$$D \propto f_n \sigma^m \qquad (2)$$

where f_n is eigenfrequency of vibration. To obtaining the relation of stress and damage with Top Tension (*TT*) and module of elasticity (*E*) of the riser, first the mode numbers ($n_{CF,IL}$) for a tensioned string and an untensioned beam relative to *TT* and *E* are given as:

$$f_n = \begin{cases} \dfrac{n_{CF,IL}}{2}\sqrt{\dfrac{TT}{mL^2}} = \dfrac{StU}{\mathrm{Re}} \;\Rightarrow\; n_{CF,IL} = \dfrac{2StU}{\mathrm{Re}}\sqrt{\dfrac{mL^2}{TT}} \\[2ex] n_{CF,IL}^2 \dfrac{\pi}{2}\sqrt{\dfrac{EI}{mL^4}} = \dfrac{StU}{\pi\,\mathrm{Re}} \;\Rightarrow\; n_{CF,IL}^2 = \dfrac{2StU}{\pi\,\mathrm{Re}}\sqrt{\dfrac{mL^4}{EI}} \end{cases}$$

$$\Rightarrow\; n_{CF,IL} \propto 1\big/\sqrt{TT} \qquad \text{:Tensioned string}$$

$$\Rightarrow\; n_{CF,IL}^2 \propto 1\big/\sqrt{E} \qquad \text{:Untensioned beam}$$

(3)

where *m* and *L* are mass of unit length and length of the riser , respectively, *U* is current velocity and *St* and *Re* are Strouhal and Reynoldes number, respectively. Since VIV amplitudes are self-limiting, one can assume that the response amplitudes x_0 and y_0 are independent of the current velocity and one can write:

$$\begin{cases} y(z) = y_0 \sin\left(\dfrac{n_{CF}\pi}{L} z\right) \\ x(z) = x_0 \sin\left(\dfrac{n_{IL}\pi}{L} z\right) \end{cases} \tag{4}$$

Uniaxial stresses caused by moment of each direction are obtained as:

$$\begin{cases} \sigma_{CF} = \dfrac{M_{CF} D_o}{2I} = E \dfrac{\partial^2}{\partial z^2} y \dfrac{D_o}{2} \\ \sigma_{IL} = \dfrac{M_{IL} D_o}{2I} = E \dfrac{\partial^2}{\partial z^2} x \dfrac{D_o}{2} \end{cases} \tag{5}$$

Finally, with respect to above equations, relation of stress with top tension and bending stiffness computed as follow:

$$\begin{matrix}\text{Uniaxial} \\ \text{Stress}\end{matrix} \begin{cases} \text{Tensioned String: } \sigma \propto n^2 \propto \dfrac{1}{TT} \\ \text{Untensioned Beam: } \sigma \propto E n^2 \propto \sqrt{E} \end{cases} \tag{6}$$

It can be seen that increasing of top tension lead to reduction of stress due to VIV. It is obvious that reduction of module of elasticity decrease the stress amplitude, especially in higher modes of vibration.
Using equations 2, 3, and 5 relation of fatigue damage with top tension and module of elasticity obtained as follow:

$$\begin{matrix}\text{Fatigue} \\ \text{Damage}\end{matrix} \begin{cases} \begin{matrix}\text{Tensioned} \\ \text{String}\end{matrix} : \quad D \propto f_n \sigma^m \propto \sqrt{TT}\left(n^2\right)^m \\ \begin{matrix}\text{Untensioned} \\ \text{Beam}\end{matrix} : D \propto f_n \sigma^m \propto \sqrt{E}\left(E n^2\right)^m \end{cases}$$

$$\propto \sqrt{TT}\left(\frac{1}{TT}\right)^m \propto \frac{1}{TT^{m-0.5}} \tag{7}$$

$$\propto \sqrt{E}\left(\frac{E}{\sqrt{E}}\right)^m \propto E^{0.5(m+1)}$$

Fatigue damage of riser decreased with increasing of top tension and reducing of module of elasticity. For a linear SN curve, the slope parameter m is often seen to be 3.0 [17] and so   for tension dominant modes and   for bending dominant modes. So for mitigation of stress and fatigue damage of VIV it is suitable that module of elasticity is reduced for higher modes (higher current velocity) and top tension increased for lower modes (lower current velocity).

3. Case study

Numerically investigation of effect of changing riser properties on the VIV responses was done using existing top tension riser of Amir-Kabir semisubmersible placed in Caspian Sea as a case study. Uniform current with various velocities was used and some results are mentioned. Based on the present position of semisubmersible, length of the riser is 713m. Other specifications of this riser are shown in the Table-1.

Table. 1 Specifications of riser of Amir-Kabir semisubmersible.

Specification	Value
Length	713 (m)
Bending stiffness (EI)	922540 (kN.m^2)
Axial stiffness (EA)	10320240 (kN)
Mass per unit length (m/L)	1080 (kg/m)
Top Tension	1000 (kN)

3.1. Modeling

There are several different available methods for prediction of VIV response of risers such as CFD, empirical models and experimental approaches. Wake oscillator model which was first introduced by Birkhoff & Zarantonello [18] used for modeling of VIV of riser. This model couples the equation of structural motion with a nonlinear oscillator equation that describes the fluid force for two directions of CF and IL. The dynamic response of a riser is described using the external force from the wake. The wake itself is described by a forced Van der Pol oscillator equation. The force term of the Van der Pol oscillator equation is related to the cylinder oscillation by a coupling term proportional to the cylinder's acceleration.
The marine riser is idealized as a tensioned Euler–Bernoulli beam. A Cartesian reference with its origin at the bottom of the riser has been used, in which the *x* axis is parallel to the flow velocity, *z* coincides with the vertical axis of the riser in its undeflected configuration and *y* is perpendicular to both as shown in the Fig. 1. A 3-D finite element model was considered for riser structure. A MATLAB code was used in this study. The Newmark-Beta method is used to solve the dynamic equation from previous section by a step-by-step time integration scheme. At each node of riser, equation of motion and Van der Pol equation of wake is coupled at each time step. Van der Pol equation is solved using modified Euler method.
The fatigue damage of a riser is evaluated based on the Palmgren–Miner Rule which Applying the Miner summation the fatigue damage is given by:

$$D = \sum_{i=1}^{N_{bin}} \frac{n_i}{N_i} \tag{8}$$

where N_i is the number of cycles to failure and n_i is the number of stress cycles at stress range $\Delta\sigma_i$ and N_{bin} is the number of stress range bins used in the Rainflow procedure.

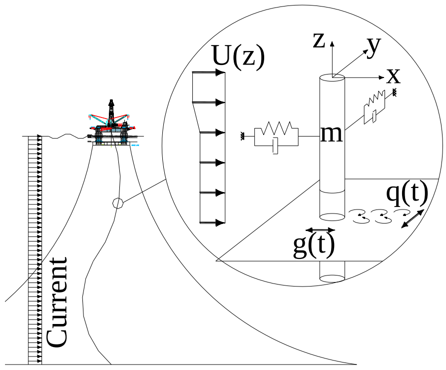

Fig. 1. 3D model of riser and 2-D wake oscillator model.

3.2 Validation of model

Chaplin et al. [19] carried out the laboratory VIV measurements of tensioned risers in a stepped current. Properties of the riser model are listed in Table 1. Lower 6m length of model was in a uniform current, while the upper part was in still water. The layout of the experiments is shown in Fig. 8. Four cases with various top tension and current velocity are chosen for VIV predictions and comparisons, as shown in Table 2.

The envelopes of CF VIV amplitude are given in Fig. 3. The present model predicts the same main dominated mode and the amplitudes are the same as experimental results. The response is mainly dominated by single mode and with increasing current velocity, the higher mode is excited. The envelopes of IL VIV amplitude are given in Fig. 4. The results of model in this direction also is the same as experiments.

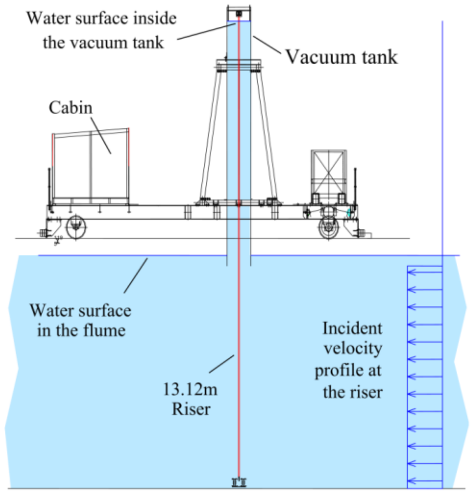

Fig. 2. Layout of Chaplin Experiments [19].

Table 1: Properties of Chaplin's tests.

Properties	Values
Total length (m)	13.12
Diameter (m)	0.028
Mass (including internal water) (kg/m)	1.85
Apparent weight (N/m)	12.1
Flexural rigidity (N/m^2)	29.9
Structural Damping	0.33%

Table 2: Test conditions for VIV comparison [19].

Cases	Top tension (N)	Current speed (m/s)
1	405	0.16
2	407	0.21
3	457	0.31
4	598	0.54
5	743	0.70

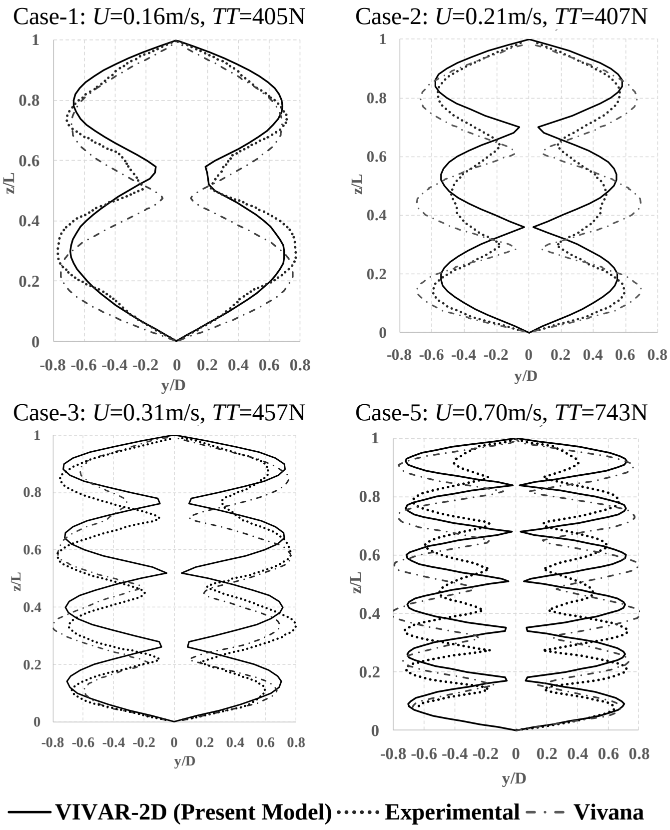

Fig. 3. Comparison of the results of the present model with others for CF VIV in stepped currents.

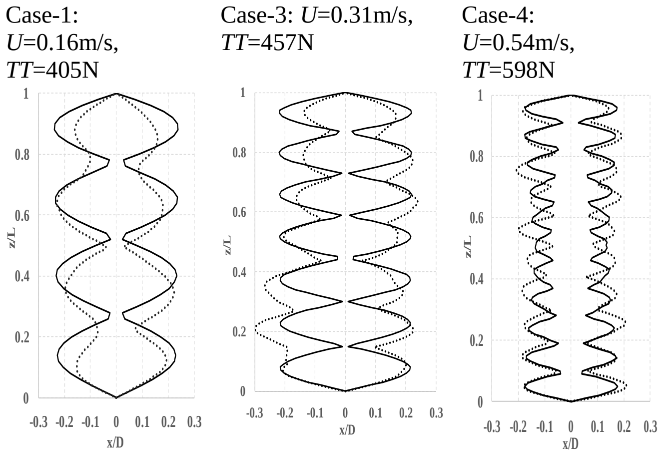

Fig. 4. Comparison of the results of present model with others for IL VIV in stepped currents.

4. Results

In this paper five cases according to Table. 2 is considered for investigation of effect of riser properties on the dynamic behavior to VIV.

Fig. 5 show natural frequencies of modes of riser and corresponding current velocity of lock-in condition for two directions of CF and IL.

Table. 2 Cases considered for VIV investigation.

Case	TT (kN)	E (kN/m^2)	Name
Case-1	1000	2.1e7	TT,E
Case-2	2000	2.1e7	2TT,E
Case-3	1000	4.2e7	TT,2E
Case-4	500	2.1e7	0.5TT,E
Case-5	1000	1.05e7	TT,0.5E

It can be seen that increasing of top tension is more effective for increasing of frequency of lower modes and increasing of bending stiffness is more effective for increasing of frequency of higher modes. It can be seen that altering top tension does not affect frequency of higher mode. This figure provides that for a certain current velocity, increasing of stiffness reduce the number of dominant modes. If the number of dominant mode reduce, the stress and fatigue damage reduce also.

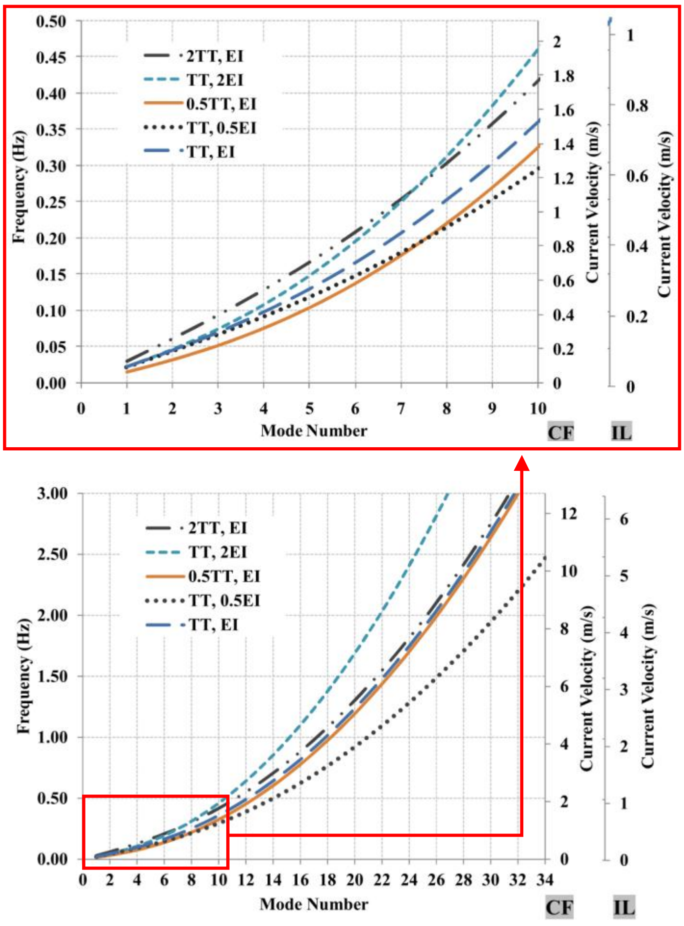

Fig. 5. Natural frequencies of riser and current velocity of lock-in conditions for two directions of CF and IL. (first 34 modes)

Fig. 6 and Fig. 7 shows Fast Fourier Transformation (FFT) of displacement of one node of riser in direction of CF for current velocities 0.2 and 1.8 m/s for five cases, respectively. This figure shows that approximately frequency of all cases is the same in IL direction but for CF direction is not. Table.3 shows frequencies of vibration of first 20 mode of riser. Also Strouhal frequency (CF direction) and twice of it (IL direction) shows in this table. In this table, frequencies that are closed to Strouhal frequency is highlighted with the same color. It can be seen that for U=0.2 m/s (tension dominant modes) in CF direction, the mode number of vibration and also frequency of vibration reduces for case with higher top tension ($2TT,E$) and mode number induce for lower top tension ($0.5TT,E$). For U=0.2 in IL direction all cases have the same frequencies at various mode numbers but mode number variation is the same as CF direction. Table 3 shows that for current velocity equals to 1.8 m/s (bending dominant mode) the mode number is reduced for cases with higher module of elasticity ($TT,2E$) and is induced for lower module ($TT,0.5E$). the same trend can be seen in IL direction in this velocity. According to table generally it is obvious that for lower velocities top tension is effective to reduce mode number of vibration and for higher velocities the bending stiffness is effective.

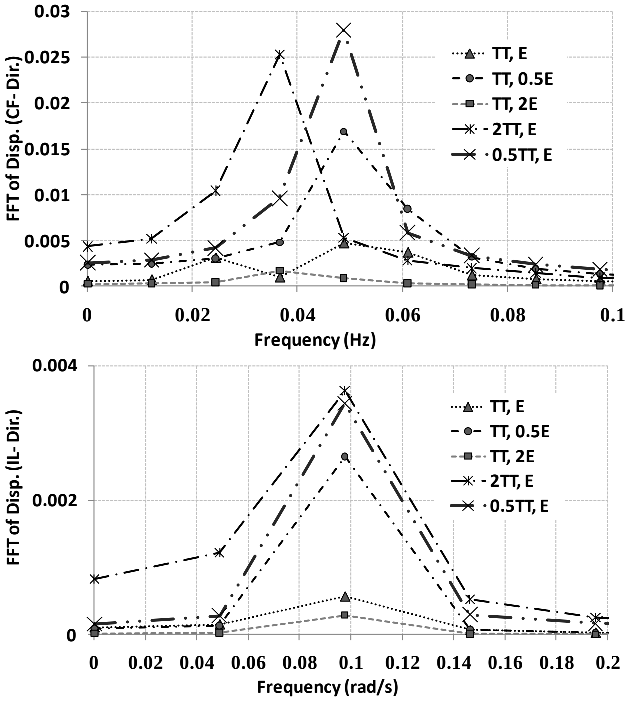

Fig. 6. Fast Fourier Transformation (FFT) of displacement of middle node of riser in CF direction-U=0.2 m/s.

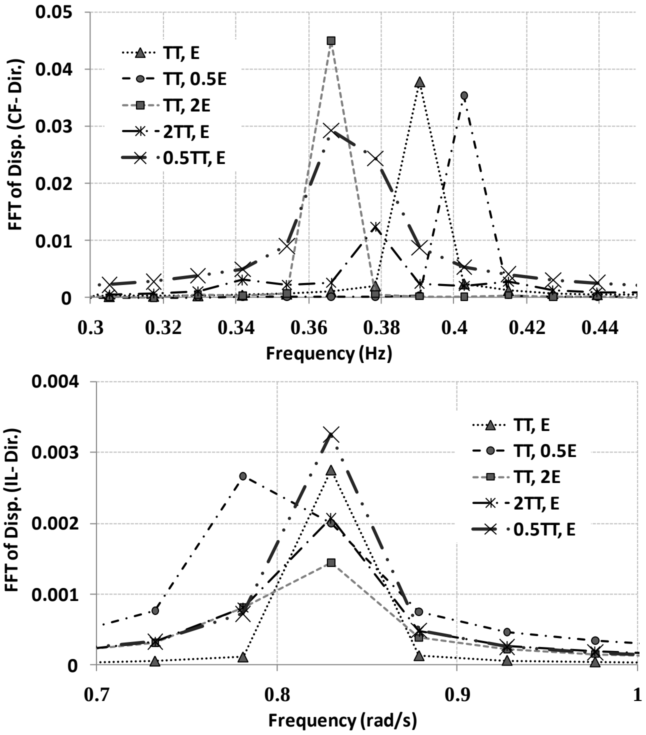

Fig. 7. Fast Fourier Transformation (FFT) of displacement of middle node of riser in CF direction-U=1.8 m/s.

Table. 3 Natural frequencies of riser and its relation with Strouhal frequency.

U (m/s)	OmegaF (Hz)	2OmegaF (Hz)
0.2	**0.047**	**0.094**
1.8	**0.424**	**0.847**

Mode Number	Frequency (Hz)				
	TT,E	TT,0.5E	TT,2E	2TT,E	0.5TT,E
1	0.018	0.018	0.019	0.026	0.013
2	0.038	0.037	0.040	0.053	0.028
3	0.060	0.058	0.066	0.082	0.046
4	0.086	0.080	0.097	0.113	0.069
5	0.115	0.104	0.135	0.147	0.096
6	0.149	0.131	0.181	0.185	0.128
7	0.188	0.161	0.234	0.228	0.165
8	0.232	0.194	0.294	0.274	0.208
9	0.281	0.231	0.363	0.326	0.256
10	0.336	0.270	0.439	0.382	0.310
11	0.396	0.314	0.523	0.444	0.370
12	0.462	0.361	0.615	0.511	0.435
13	0.533	0.412	0.715	0.583	0.505
14	0.609	0.467	0.823	0.597	0.582
15	0.691	0.526	0.844	0.661	0.663
16	0.779	0.588	1.062	0.744	0.751
17	0.872	0.725	1.194	0.832	0.844
18	0.971	0.771	1.333	0.926	0.943
19	1.076	0.799	1.481	1.025	1.047
20	1.186	0.877	1.637	1.130	1.157

Fig. 8 and Fig. 9 provide fatigue damage of riser nodes for current velocity of 0.6 m/s, for moment caused by vibration in CF and IL direction, respectively. It is evident from this figures that fatigue damage decreased with increasing of *TT* or reducing of *E*. The same trend can be seen for IL direction.

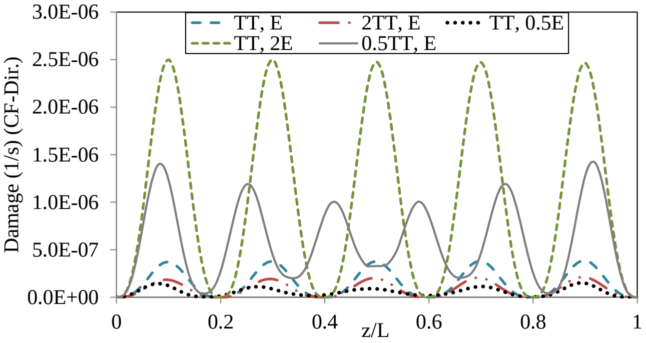

Fig. 8. Fatigue damage of riser nodes for moment caused by CF vibration for current velocity equals 0.6 m/s.

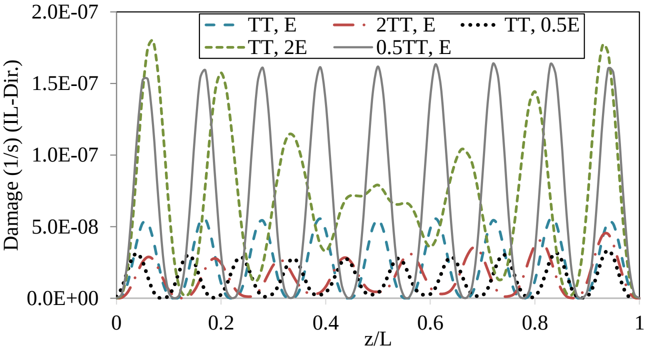

Fig. 9. Fatigue damage of riser nodes for moment caused by IL vibration for current velocity equals 0.6 m/s.

Fig. 10 and Fig. 11 show the ratio of stress due to moment of CF and IL direction for four cases (2TT, 2E, 0.5TT, 0.5E) to main structure versus current velocity, respectively. It can be seen that decreasing of *E* and increasing of *TT* cause decreasing of stress at two directions of CF and IL. According to these figures when current velocity increased, effect of TT is reduced and stress ratio of both cases of TT ratio=2 and 0.5 approach to one. Effect of variation of E approximately is constant for current velocities bigger than 0.4 m/s.

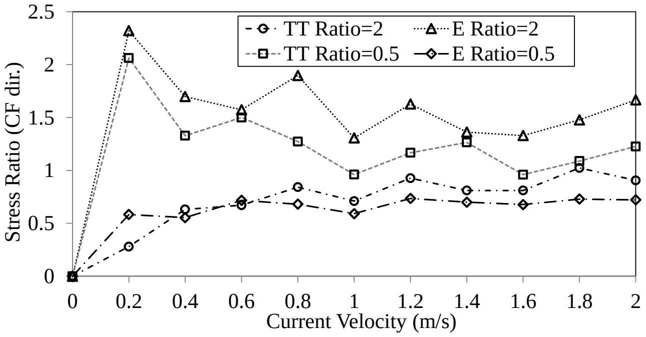

Fig. 10. Ratio of stress of moment caused by CF vibration for various cases.

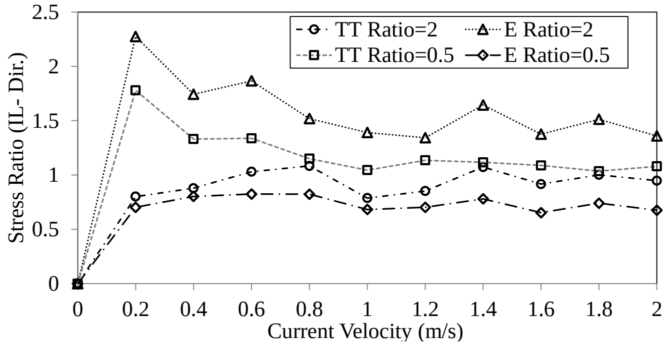

Fig. 11. Ratio of stress of moment caused by IL vibration for various cases.

Fig. 12 and Fig. 13 provide the ratio of fatigue damage due to CF and IL moment for four cases to main structure versus current velocity, respectively. It can be seen that increasing of TT is effective in lower velocities and for higher velocities variation of TT is not affect fatigue damage predominantly and fatigue damage ratio is very close to one for cases (TT ratio equals to 2 and 0.5). These figures shows that in low velocities, fatigue damage is very sensitive to variation of riser properties and variations of fatigue ratio is very high for various cases.

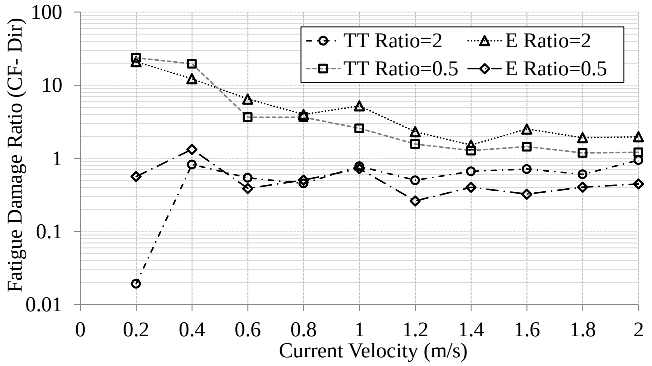

Fig. 12. Ratio of fatigue damage of moment caused by CF vibration for various cases.

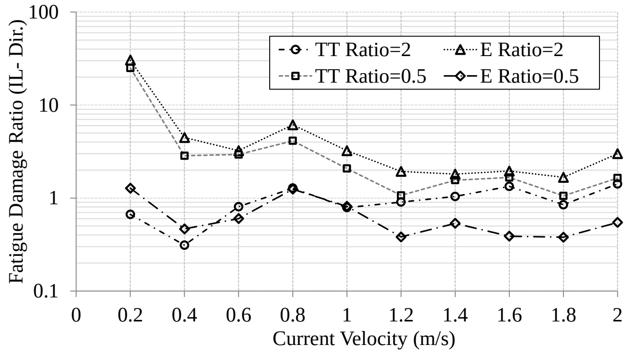

Fig. 13. Ratio of fatigue damage of moment caused by IL vibration for various cases.

5. Conclusion

The effects of shifting frequency on the VIV responses of marine risers were studied in this paper. Relation of stress and fatigue damage variation with riser properties such as top tension and module of elasticity is obtained. For numerical study a coupled 2D wake-structure interaction model was used for modeling of VIV that considered both direction of CF and IL. Stress of two directions was computed based on the moments that are obtained from amplitude of displacement of CF and IL. The fatigue damage of a riser is evaluated based on the Palmgren–Miner Rule and Rainflow procedure is used for counting the number of stress ranges. The following results are obtained:

- VIV has self-limiting property and for certain amplitude of vibration, higher mode of vibration has higher curvature and also stress. Also because of bigger frequency of vibration, fatigue damage increased with mode number.
- This shows that for a certain current velocity, stress for tension dominant modes is proportional to T^{-1} and for bending dominant modes is proportional to $\sqrt{E}$.
- For a certain current velocity, fatigue damage for tension dominant modes is proportional to $1/T^{(m-0.5)}$ and for bending dominant modes is proportional to $E^{0.5(m+1)}$. If the slope parameter m is assumed to be 3.0 [17], fatigue damage is proportional to $1/T^{2.5}$ and E^2, for tension and bending dominant modes, respectively.
- For tension-dominant modes, increasing of top tension can reduce stress and fatigue damage. This effect decreased with increasing of mode number. So this method can be used for VIV reduction for lower current velocities.
- Decreasing of module of elasticity can be used to reduce stress and fatigue damage in a wide range of current velocities.
- Increasing of bending stiffness, amplified stress and fatigue damage of riser. This is because the term of EI is used for moment computing. This effect is higher for lower modes of vibration.
- Stiffness and frequencies increased with module of elasticity, but because the *E* is used in stress relation, finally the stress and fatigue, amplified with increasing of *E*.

References

1- Gad-el-Hak, M. and Bushnell, D.M., (1991), *Separation control: review*, J Fluids Eng. Vol. 113, p.5–30.

2- Choi, H., Jeon, W.P. and Kim, J.S., (2008), *Control of flow over a bluff body*, Annu Rev Fluid Mech; Vol. 40 p. 113–39.

3- Gad-el-Hak, M., (2000), *Flow Control: Passive, active and reactive flow management*, Cambridge University Press

4- Zhou, T., Razali, S.F.M., Hao, Z. and Cheng, L., (2011), *On the study of vortex-induced vibration of a* *cylinder with helical strakes*, J. Fluids Struct., Vol. 7, p. 903–917.

5- Shih, W.C.L., Wang, C., Coles, D. and Roshko, A., (1993), *Experiments on flow past rough circular cylinders at large Reynolds numbers*, J. Wind Eng Ind Aerodyn, Vol. 49, p. 351–368.

6- Zdravkovich, M.M., (1997), *Flow around Circular Cylinders*, Vol. I Fundamentals. J. Fluid Mech. Vol. 350, p. 377–378.

7- Hwang, J.Y., Yang, K.S. and Sun, S.H., (2003), *Reduction of flow-induced forces on a circular cylinder using a detached splitter plate*, Phys Fluids., Vol. 15, p. 2433–2436.

8- Eisenlohr, H. and Eckelmann, H., (1989), *Vortex splitting and its consequences in the vortex street wake of cylinders at low Reynolds number*, Phys Fluids A Fluid Dyn., Vol. 1, p. 189–192.

9- Zhao, M., Cheng, L., Teng, B. and Liang, D., (2005), *Numerical simulation of viscous flow past two circular cylinders of different diameters*, Appl. Ocean Res, Vol. 27, p. 39–55.

10- Zhao, M., Cheng, L., Teng, B. and Dong, G., (2007), *Hydrodynamic forces on dual cylinders of different diameters in steady currents*, J. Fluids Struct., Vol. 23, p. 59–83.

11- Sanaati, B. and Kato, N., (2012), *A study on the effects of axial stiffness and pre-tension on VIV dynamics of a flexible cylinder in uniform cross-flow*, Appl. Ocean Res., Vol. 37, p. 198–210.

12- Chen, W., Li, M., Zheng, Z. and Tan, T., (2012), *Dynamic characteristics and VIV of deepwater riser with axially varying structural properties*, Ocean Eng., Vol. 42, p. 7–12.

13- Lee, L. and Gerretsen, H., (2011), VIV *inference from tension measurements*, In: Proceedings of the 30th International Conference on Offshore and Arctic Mechanics (OMAE2010), Paper no. 49552.

14- Lee, L. and Allen, D., (2010), *Vibration frequency and lock-in bandwidth of tensioned, flexible cylinders experiencing vortex shedding*, J. Fluids Struct., Vol. 26, p. 602–610.

15- Srinil, N., (2011), *Analysis and prediction of vortex-induced vibrations of variable-tension vertical risers in linearly sheared currents*, Appl. Ocean Res., Vol. 33, p. 41–53.

16- Baarholm, G.S., Larsen, C.M. and Lie, H., (2006), *On fatigue damage accumulation from in-line and cross-flow vortex-induced vibrations on risers*, Journal of Fluids and Structures, Vol. 22, p. 109–27.

17- NORSOK Standard 1998. *Design of Steel Structures—Annex C—Fatigue Strength Analysis*.

18- Birkhoff, G. and Zarantonello, E.H., (1957), *Jets, wakes, and cavities.*

19- Chaplin, J.R., Bearman, P.W., Cheng, Y., Fontaine, E., Graham, J.M.R., Herfjord, K., et al. (2005), *Blind predictions of laboratory measurements of vortex-induced vibrations of a tension riser*, Journal of Fluids and Structures, Vol. 21, p. 25–40.

INTERNATIONAL JOURNAL OF
COASTAL & OFFSHORE ENGINEERING
IJCOE Vol.2/No. 1/Spring 2017 (17-26)

Available online at: http://ijcoe.org/browse.php?a_code=A-10-1-1&sid=1&slc_lang=en

Drilling Risk Identification, Filtering, Ranking and Management

Sirous Yasseri

Brunel University, London, UK, sirous.yasseri@Brunel.ac.uk

ARTICLE INFO

Article History:
Received: 10 Sep. 2016
Accepted: 9 Mar. 2017

Keywords:
Drilling Risk Aassessment;
Risk Influencing Factors
Risk Filtering & Ranking
Analytic Hierarchical Process

ABSTRACT

Drilling Operations are exposed to a variety of hazards, some of which may be location and activity dependent and each could pose different risk from different paths. Drilling operation may be vulnerable to hurricanes in one region and be exposed to Geohazards in another. However, there are other hazards, (e.g. corrosion, age degradation, poor maintenance), which equally affects every rig. Identifying what can go wrong and their likelihood and possible consequences provides insight into vulnerability of the operation and helps to generate mitigation options. Filtering and Ranking risk contributors enable to decide priorities and to focus on the most important risk contributors. This paper offers a framework to identify, assess, prioritize, and manage drilling risks, which includes: (1) a holistic approach to risk identification; (2) prioritization of a large number of risk influencing factors or risk scenarios; (3) structured elicitation of experts' opinion and effective integration of experts judgment into qualitative and quantitative analyses to supplement limited data availability; (4) extreme and catastrophic event analysis; and (5) use of multi-objective framework to evaluate risk management priorities.

1. Introduction

Drilling operation is a complex activity and it is subject to a variety of hazards, some of which are location and activity dependent. Thus, the drilling risk management should be commensurate with the site, water depth, available information and complexity of the situation. As the drilling commences, new information becomes available and some predicted hazards may still pose risk, while others may not. New hazardous situations may be encountered or identified, and the characteristics of those already identified could change. Thus, the risk management should be carried out periodically at all stages of the project; i.e. before, during and after drilling.

There are usually more than six hazard categories that influence the risk; also there may be several paths through them a hazard could threaten the operation. The main hazards are grouped under the distinctive headings, such as: Geohazards; Equipment & Material; Human Elements; Local environment; Human-Machine Interface; Design issues; Technology and Operation; Organizational elements; Maintenance & Integrity; Externalities and so on. In some situations the age of the equipment and procedures may also require special attention. The above categories are not exhaustive.

This paper proposes a framework, which starts with organizing hazards into a tree-like structure, consisting of three or more layers. The first level is the goal and the second level is all primary hazard categories. The identification of primary hazard groups is mainly based on engineering judgment, brain storming, QRA, reports and available data (accident databases). In the third level, each category is then broken down into several sub-categories. Each sub-category can be in turn broken into sub-sub-categories and so on (see Figure 2).

Hazards are placed in this hierarchical structure as they are identified, and it is organized by source (category), consequently, the total risk exposure can be better visualized, and the risk mitigation plans are more easily implemented. This process produces a catalogue of all possible hazards, termed Risk Influencing Factors (RIFs), which must be filtered, since there is no need to take forward hazards of lesser importance for more detail study.

2. Hazard Structuring

Hazard identification, or scenario building, is the first step in determining hazards affecting an activity. Identification also enable to documenting characteristics of hazards. Each hazard is a risk influencing factor, which are grouped under headings and subheadings. In risk analysis we envision what could go wrong, how often and what are the consequences if something goes wrong. For this we need to list all possible events or "scenarios". This approach produces triplets [1], i.e.

$$\langle S_i, L, C_i\rangle; \quad i = 1,2,\cdots,N \tag{1}$$

Where, $S_i$is the scenario i and $L_i$is the likelihood of scenario$i$. Risk is defined as a function of these triplets, i.e.

$$R = \{\langle S_i, L_i, C_i\rangle\} \tag{2}$$

This equation is generally simplified as

$$R = \sum_{i}^{N} L_i \times C_i \tag{3}$$

Where, $C_i$is the consequence of scenario i

Table 1: The Risk Influencing Factors: showing major risks and their attributes

Category	Sub-categories
C1-Geohazards	C11- Formation pressure
	C12 Soil & Rock types and strength
	C13- Shallow faults
	C14- Gas hydrate
	C15- Multiple Geohazards
	C16-Top-hole Geology (sand, salt, carbonate, discontinuities, clay, loose formation)
	C17- Shallow soil (for jack-ups), sediment type and strength, Boulder bed,
	C18 -Salt or mud diapirs and diatremes, Calcareous soils, Coral, hard ground
C2-Equipment & material	C21- Material suitability & defects; Fabrication defects
	C22- Equipment used (robustness & dependability, maintenance)
	C23: Effect of Ageing; wear & tear , worn or fatigued part;
	C24- Operational and resource limits
	C25- Operational limit, failure to meet qualification & code compliance
	C26- Late changes to well design and procedures;
	C27- Equipment quality (special equipment; delay; damaged)
	C28 - Spare & material availability,
	C29- Unsuitability and unforeseen site condition, injuries, toxic emission
C3- Human Elements	C31- Skill & knowledge based mix, Training, Experience
	C32- Workload & Work coordination; Shift and stint duration
	C33- Quality of working environment.
	C34- Communication, Language barrier, Openness,
	C35- Performance evaluated & Suitability and Training; fit for the job
	C36 - Personnel exposure (qualification, experience, required presence, shift)
	C37 - Tiredness, boredom,
	C38 - Situational awareness
C4- Design; Technology and Operation	C41- Technology Readiness maturity,
	C42- New technology (e.g. packers and liner hangers);
	C43-Down-hole monitoring;
	C44- Kick tolerance;
	C45- Deviation versus hole size, Hole size contingencies,
	C46 - Cementing of long casing strings;
	C47- Well access and work over requirements, Well design and Job complexity
	C48- Blow out contingency;
C5-Automation & human Machine Interface	C51- Software error
	C52- Temporary disabling safety devises to get round annoying alarms,
	C53- Information overload
	C54- Design of Human-machine interface
	C55 - Failure of data processing function; failure of information support function;
	C56 - Failure of surveillance function; Failure of communication function;
	C57 - Expert system which by passes the operator involvement,
C6- Local condition	C61- Water depth
	C62- Local Weather
	C63 - Current , wave , tsunami, hurricane, ice, rain, storm surge, tropical cyclones
	C64- Wind and water borne debris
	C65 - Requires special equipment
	C66 - Existing infrastructure , surface and sub-surface,
	C67 - Shallow water flow,
	C68 - Preservation areas and sanctuaries
C7- Organizational elements	C71- Mix of cultures & compatibility (e.g. working to different procedures)
	C72- Organizational leaning
	C73- Personnel selection; Coordination
	C74- Training program, process and formalization
	C75- Safety commitment, perception & enforcement
	C76 Time and cost constraints
	C77- Bonus system and benefits upon performance
	C78 experience with operators or contractors,
	C79 Operational aspects (language barriers,, local marine traffic, shore proximity);

The set of triplets should be complete, namely it should include every possible scenarios, or at least those which are important. In fact, it is not obvious how even near completeness can be achieved [2]. Moreover, the set of scenarios must not overlap. This method generates a comprehensive list of all sources of hazards, i.e., categories of risks, in the order of dozens of entries. Consequently, there is a need to discriminate among these sources.

Tables 1 and 2 show a catalogue of hazards which might influence a drilling activity. The heading indicates that all hazards that might impact the drilling are identified during the hazard identification process. The sub-headings are attributes of each heading which facilitates the judgment process. Of course each sub-category can be in turn broken into sub-sub-categories and so on.

Tables 1 and 2 contain major risk influencing factors reported in the literature. These tables show a two-level risk break down structure. More remote or obscure hazards may not be identified and hence making the set of scenario incomplete.

It can be seen that there are numerous Risk Influencing Factors (RIFs) which could influence a drilling operation, and there is a certain probability that only a number of RIFs to affect a given operation. How strongly a RIF influences the risk is described by its weight relative to other RIFs.

Table 2: The Risk Influencing Factors: showing major risks and their attributes

Category	Sub-categories
C8- Complexity	C81- Multiple paths to failure; -Uncontrollability; Un-detectability; Cascading effect; Irreversibility C82- Latency (duration effect); C83- Demanding job; C84- High pressure & high temperature C85- Combination of Several adverse conditions C86 - First time experience; the number of components, novel assemblies, New skill set C87 Complexity mix (Combination of Several adverse conditions
C9-Uncertainty	C91- Phasing and planning; C92 Scope change C93- Complex procedures C94- Management of change(design , operating conditions, equipment substitution, plans, personnel) C95- Unforeseen events C96- Safety critical equipment
C10-Seabed Condition	C101- Seabed topography and relief, Seabed channels and scours, Seafloor sediments C102- Fault escarpments, Unstable slopes Sand banks, waves, and mega-ripples, Collapse features C103- Cold water C104- Rock outcrops, Pinnacles, Boulders, Rock outcrop, Hard grounds, Seafloor sediments, Reefs C105- Mud flows gullies, Volcanoes, Lumps, Lobes, Slumps, Fluid expulsion features C106- Sand banks, Sand waves, Mega-ripples C107- Gas hydrate mounds, Gas vents, Pockmarks, shallow gas, as cut mud sections, C108 - Seabed channels and scours C109- Diapiric structures, escarpment, Collapse features, shallow faults
C11- Regulation	C111- lack of Independent oversight C112- Inadequate regulation C113- mandatory regular inspection C114-periodial re-certification C115- regulator involvement and visibility
C12 -Wellbore Integrity	C121- Mechanical Wellbore Instability (Rock type & strength, C122- Wellbore geometry (hole inclination and azimuth) C123- manmade related stress, poor hole cleaning , excessive drilling vibration C124: Drilling into pre-stressed rock, excessive wellbore pressure, vibration C125 - Shale type & instability , time dependent swelling, reaction between fluid and shale C126 - Shale hydration mechanism, forces holding plates together, pore presses. stresses C127 - Inadequate well planning (wrong drilling fluid, wrong inclination &azimuth)
C13- Manmade	C131 - Hazardous waste C132 - Pipelines, Umbilicals, Power cables , Communication cables, Wellheads C133 - Dumped Munitions or chemicals C134- Sanken ships C135 – Debris; disposed wastes
C14- Miscellaneous	C141 - Shipping route C142 - Military training area C143 - Spill prevention C144- External Interferences, wilful acts, Third party present C145 - Anchor System limitation, Boat support needs C146- Weight restriction, riser length, draught limitation C147 - Cost sensitivities,

Table 3: Questionnaire for sifting hazards (After [1])

Question	Meaning
Is this hazard detectable	The system has redundant means of detecting and arresting a hazard before a harm could occur.
Is this hazard controllable	There are controls by which it is possible to take action or make an adjustment to prevent harm.
Is there multiple paths to failure	There are multiple and possibly unknown ways for events to cause harm, e.g. by circumventing safety controls.
Is the effect irreversibility	The system cannot be returned to the normal condition once the adverse event occurred.
Is the event duration of long enough to cause harm	Prolonged events with adverse consequence
Would the event trigger a cascading events	The event can trigger a cascading events which easily and rapidly propagate which cannot be contained
Does the event originate from external sources?	Risk due to external interferences with little or no control over them.
Can the system take more wear and tear	Would further degradation lead to degraded performance or accident
Does the machine-human interface aggravate the problem	Interfaces among diverse subsystems (e.g., human, software and hardware) causing adverse events
Do we understand the complexity?	Too many complexity create a potential for system level behaviours that are not anticipated from a knowledge of components and the laws governing their interactions
Is technology qualified for the task?	Immature or inappropriate technology or other lack of concept qualification

This risk influencing structure can be viewed as a means leading to a set of actions or behaviour that are required of the system in order to succeed in functioning safely; conversely, each risk factor defines a scenarios in which the system fails to deliver in one or more ways. The union of all risk scenarios should then be complete. This completeness is a very desirable feature. However, the intersection of two of our risk scenario sets, corresponding to two different heading, may not be empty. The method allows the set of subsets to be overlapping. Thus, by a filtering process overlapping hazards must be rationalised.

Risk Filtering

Filtering is performed at the sub-category level, to eliminate overlapping and less relevant RIFs. RIFs are filtered according to their perceived levels of likelihood and consequences. Filtering is achieved on the bases of expert experience and knowledge, as well as function, and operation of the drilling system being assessed. This activity often substantially reduces the number of RIFs. In this, the joint contributions of two different types of information-the likelihood of what can go wrong and the associated consequences-are estimated on the basis of the available evidence and engineering judgment. The evidence for taking forward a hazard for detailed studies, can be determined by answering questions noted in Table 3.

Risk matrix is a useful tool for visualising risk. This type of tool is commonly used with the assistance of experts. Since risk is defined as triplet then its likelihood and consequence must be judged. Commonly, 5x5 Matrix is used, but the 8x8 matrix (Figure 1) provided a better resolution. Figure 1 defines eight scales and their linguistic description. Each risk scenario is characterized using qualitative assessment of both consequence and likelihood. In risk matrix, the likelihoods and consequences are combined into a joint concept called "severity" [2]. The group of cells in the upper right indicates the highest level of severity. The mapping is achieved by first estimating the likelihood of a hazard then judging its consequence, and finally determining which cell it belongs to. The cells position determines the relative levels of severity.

In quantitative risk assessment, risk is defined as the product of likelihood of a hazards and its impact should it happen [2]. The multiplication method could yield the same numerical value for a high consequence but low likelihood event to be the same as high likelihood but low consequence event. This is a misleading picture, though both events are damaging, the high consequence event can wipe out an organisation. The problem is more pronounced for event in the middle of the risk matrix. Thus, cells in Figure 1are numbered to indicate their position importance. This importance numbering gives more emphasis to the middle range, compared with the multiplication approach.

Each RIF from the catalogue is placed into a cell, according to its perceived likelihood and impact, to represents a failure scenarios. Each scenario has its own combination of likelihood and consequence. These hazards can also be filtered based on scope, spatial & temporal domain considerations. Since we are considering the safety at the planning stage, we start by presenting an initial set of relevant hazards which could be validated by all stakeholders. RIFs falling in the low-severity boxes are filtered out and set aside for later consideration. The completed matrix shows which events are the major risk drivers.

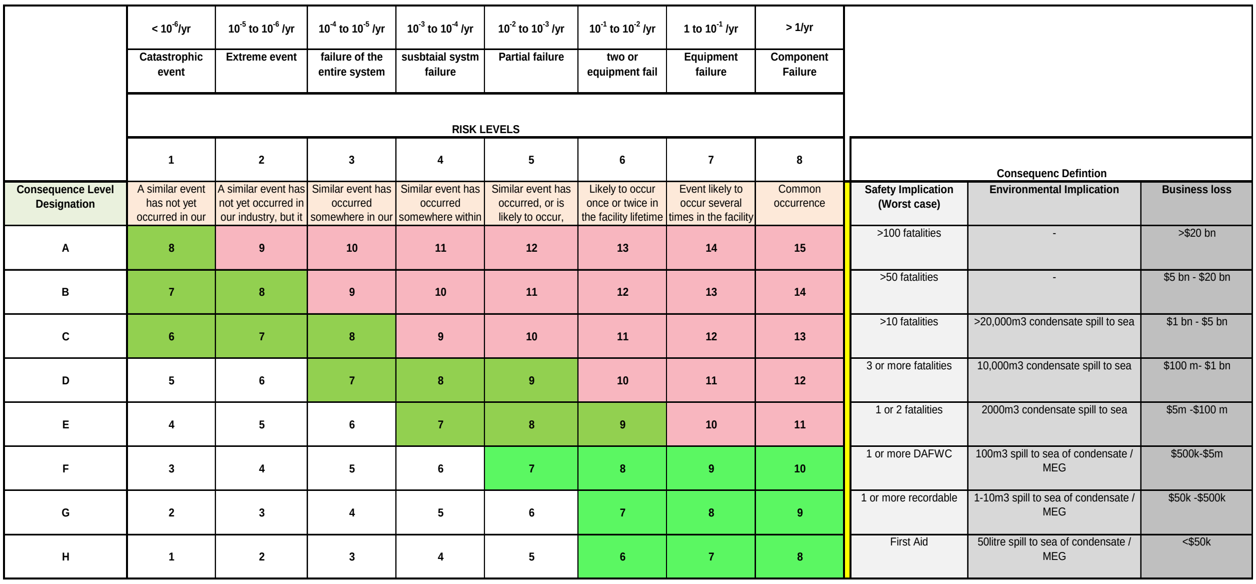

	$< 10^{-6}$/yr	10^{-5} to 10^{-6} /yr	10^{-4} to 10^{-5} /yr	10^{-3} to 10^{-4} /yr	10^{-2} to 10^{-3} /yr	10^{-1} to 10^{-2} /yr	1 to 10^{-1} /yr	> 1/yr			
	Catastrophic event	Extreme event	failure of the entire system	susbtaial systm failure	Partial failure	two or equipment fail	Equipment failure	Component Failure			
	RISK LEVELS										
	1	2	3	4	5	6	7	8	Consequenc Defintion		
Consequence Level Designation	A similar event has not yet occurred in our	A similar event has not yet occurred in our industry, but it	Similar event has occurred somewhere in our	Similar event has occurred somewhere within	Similar event has occurred, or is likely to occur,	Likely to occur once or twice in the facility lifetime	Event likely to occur several times in the facility	Common occurrence	**Safety Implication (Worst case)**	**Environmental Implication**	**Business loss**
A	8	9	10	11	12	13	14	15	>100 fatalities	-	>$20 bn
B	7	8	9	10	11	12	13	14	>50 fatalities	-	$5 bn - $20 bn
C	6	7	8	9	10	11	12	13	>10 fatalities	>20,000m3 condensate spill to sea	$1 bn - $5 bn
D	5	6	7	8	9	10	11	12	3 or more fatalities	10,000m3 condensate spill to sea	$100 m- $1 bn
E	4	5	6	7	8	9	10	11	1 or 2 fatalities	2000m3 condensate spill to sea	$5m -$100 m
F	3	4	5	6	7	8	9	10	1 or more DAFWC	100m3 spill to sea of condensate / MEG	$500k-$5m
G	2	3	4	5	6	7	8	9	1 or more recordable	1-10m3 spill to sea of condensate / MEG	$50k -$500k
H	1	2	3	4	5	6	7	8	First Aid	50litre spill to sea of condensate / MEG	<$50k

Figure 1: A typical industry risk matrix for filtering (and ranking) risks.

Risk Ranking

The boundaries of the different levels of risks are not symmetrical, because a catastrophic event, irrespective of its probability, could cause very large loss. The risk matrix doesn't provide a numerical relative importance of each rating, so the tool divides the risks into groups, but does not say anything about the ranking within each grouping. Thus, after filtering of minor hazards, the remaining hazards must be ranked to determine their relative strength. This enables to prioritise expenditure for avoiding, controlling and mitigating impact of hazard if they were to occur.

There are two types of comparisons: absolute and relative. In absolute comparisons, two hazards are compared with a standard or a baseline which exists in one's mind and has been formed through experience. In relative comparisons, hazards are compared in pairs according to a common attribute. Saaty, [8] and [9], proposed a pairwise comparison for determining the relative importance of two criteria known as analytic hierarchy process (AHP). The input to AHP models is the experts' answers to a series of questions of the general form, e.g. 'How important is Category 'C1' relative to Category 'C2'?' These are termed 'pairwise comparisons' [8]. Within AHP, questions of this type may be used to establish, both weights for categories and importance scores for different categories, using a suitable scale (see [8] or [10]). Very often qualitative data cannot be known in terms of absolute values. AHP allows the integration of both, quantitative and qualitative criteria [9].

It is difficult to be completely consistent because of the complexity and diversity of subjective judgment. The AHP does not require that judgments to be totally consistent. But, priorities make sense only if derived from consistent or near consistent matrices, and hence consistency check must be applied. Saaty [8] Proposed a consistency index (CI) to measure the degree of consistency (or inconsistency) of the judgments for each stage of the AHP process. If the comparisons are not reasonably consistent, then this check provides a mechanism for improving consistency by going back to the pairwise comparison. The mathematical background can be found in [10]

Case Study

The ranking process is illustrated using an example case, which is a drilling operation in a seismically active area. In a hazard filtering process, it was determined that the categories C1 to C7 (Table 1) have the largest direct effect on the risk, which are as listed in the first column of Table 3. The rest of hazards listed in (Tables 2) are considered either not to apply or to be of no importance and hence were filtered out. Figure 2 shows the content of Table 3 in its hierarchal format.

In consultation with the industry experts seven pairwise comparison matrices were developed to determine the categories and sub-categories weights. The weights for all the pairwise comparison matrices were computed using a spreadsheet. By aggregating the hierarchy, the preferential weight of each criterion is found. A consistency check is then performed. If the comparisons are not reasonably consistent, then this check provides a mechanism for improving consistency by going back to the pairwise comparison. Aggregating opinion of more than one expert, in principle, would enhance the decision making process [6] and [7].

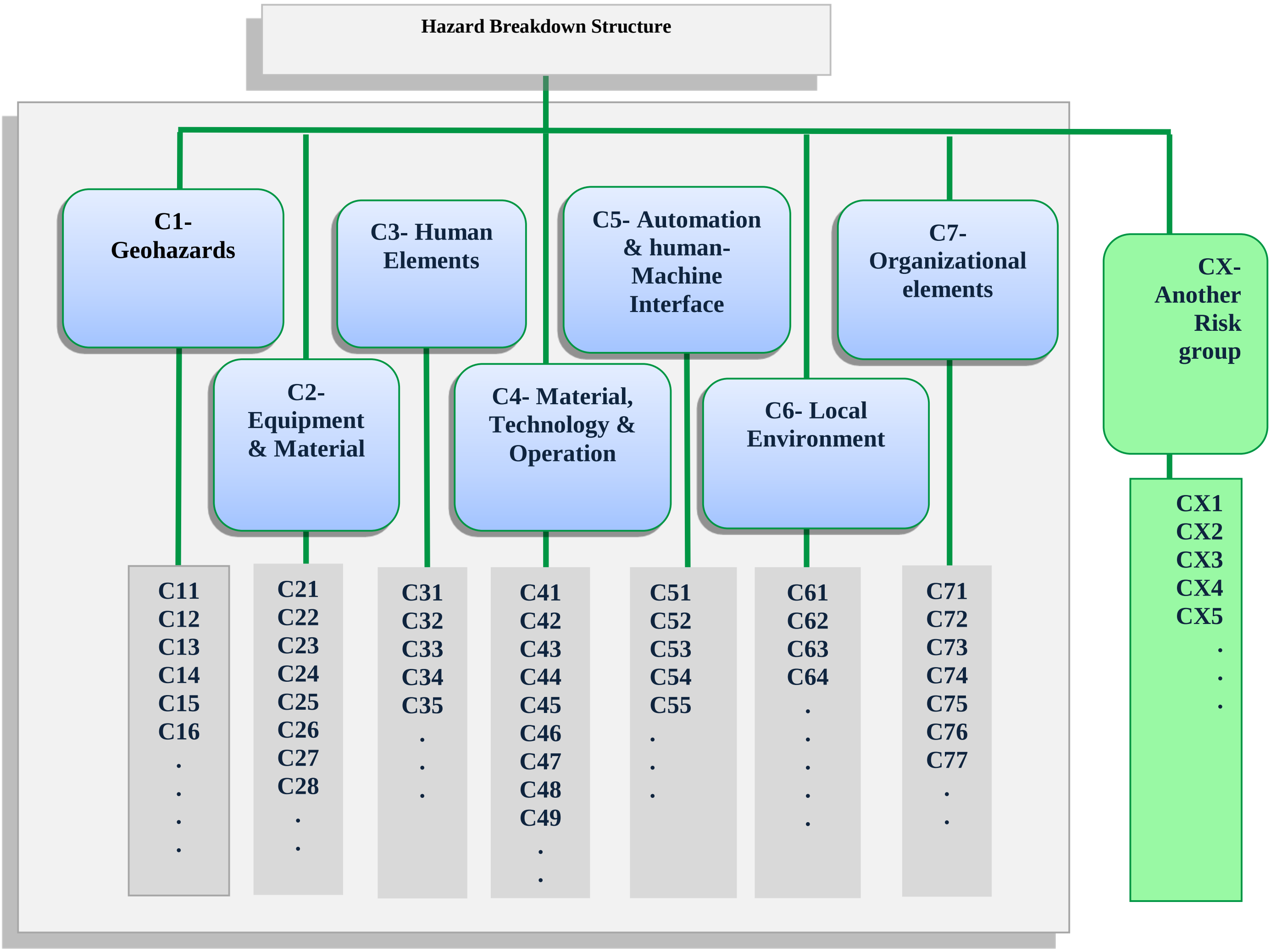

Figure 2: Hazard Breakdown Structure for the case study

	C1	C2	C3	C4	C5	C6	C7	Weight
C1	1	2	1	1	1	2	6	0.20
C2	1/2	1	1/2	2	2	1	6	0.17
C3	1	1	1	1	2	3	2	0.19
C4	1	1/2	1	1	2	2	2	0.16
C5	1	1/2	1/2	1/2	1	1	4	0.12
C6	1/2	1	1/3	1/3	1	1	5	0.11
C7	1/6	1/6	1/2	1/2	1/4	1/5	1	0.05
Sum	6 1/6	4 5/6	6 1/3	9 1/4	10 1/5	26	6 1/6	**1.00**
CR= 0.0589								

Figure 3: First level pairwise comparison matrix

Figure 3 shows the pairwise comparison of the primary categories (the second layer). Each column is summed up first, and then each element is divided by the sum of its column. The weight is then averaged of each row. The pairwise comparison matrices for subcategories are not shown here, but the results are given in the column 4 of Table 4. Table 4 summarizes these results. The second column gives the ranking of the top level categories as calculated in Figure 4. The fourth column give the ranking of all hazards within each category. The last column is the multiplication of the second and the fourth columns. These results are plotted in Figures 4 and 5.

Table 4: Summary of pairwise comparison matrices

Primary Criteria	Weight/Primary	Sub-criteria	Sub-criteria weight	Combined weight
C1-Geohazards	0.20	C11	0.213	0.043
		C12	0.343	0.069
		C13	0.153	0.031
		C14	0.146	0.030
		C15	0.073	0.015
		C16	0.073	0.015
C-2 Equipment & material	0.17	C21	0.228	0.040
		C22	0.125	0.022
		C23	0.039	0.007
		C24	0.218	0.038
		C25	0.098	0.017
		C26	0.098	0.017
		C27	0.098	0.017
		C28	0.098	0.017
C3- Human Elements	0.19	C31	0.183	0.034
		C32	0.212	0.040
		C33	0.195	0.037
		C34	0.196	0.037
		C35	0.213	0.040
C4- Design; Technology and Operation	0.16	C41	0.028	0.005
		C42	0.026	0.004
		C43	0.058	0.009
		C44	0.053	0.009
		C45	0.115	0.019
		C46	0.180	0.029
		C47	0.180	0.029
		C48	0.180	0.029
		C49	0.180	0.029
C5-Automation & human-Machine Interface	0.12	C51	0.147	0.017
		C52	0.107	0.013
		C53	0.285	0.033
		C54	0.261	0.030
		C55	0.199	0.023
C6- Local environment	0.11	C61	0.151	0.017
		C62	0.201	0.022
		C63	0.367	0.041
		C64	0.281	0.031
C7- Organizational elements	0.05	C71	0.215	0.010
		C72	0.247	0.012
		C73	0.148	0.007
		C74	0.077	0.004
		C75	0.115	0.005
		C76	0.090	0.004
		C77	0.106	0.005

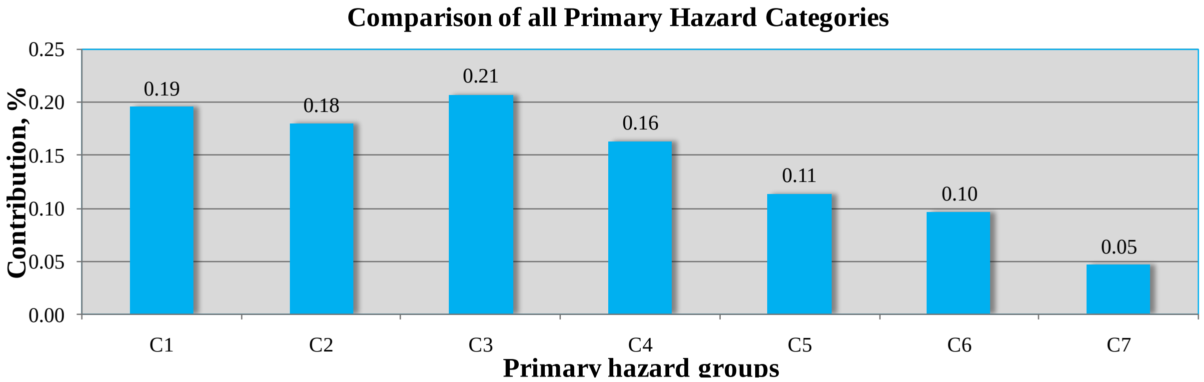

Figure 4: Ranking of all hazard sub-categories

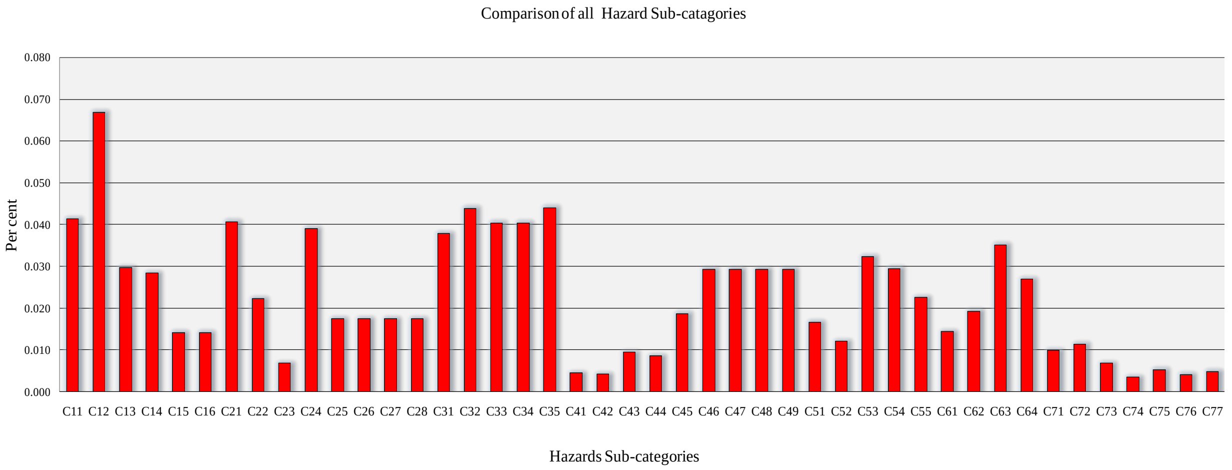

Figure 5: Ranking of all hazards sub-categories to risk.

Risk Management

The hazard control is based on the concept of safety barriers. The safety barrier approach in turn is based on two models, the Swiss cheese accident model and the bow tie method. For this, imagine a row of Swiss cheese slices, (Figure 6), in which each slice is a barrier and the hole represents a weakness in the barriers that may fail to prevent an accident. If the holes line up, which may occur when multiple robust barriers are not in place or they are properly functioning, accidents can occur. This simple model is surprisingly a useful tool – the more barriers, i.e. more Swiss cheese slices, the safer the facility, and the smaller the holes, the smaller is the weaknesses of the barrier. Barrier management is an effective tool to connect facility operations with HSE cases, design features and regulatory requirements in an integrated fashion.

The tool that captures the Swiss cheese concept and carries it further is the Bow Tie Diagram (Figure 7). For each “Top Event”, such as a major leak, blowout, or explosion, , and all of other threats, e.g. equipment malfunctions or failure to follow operating procedures are shown on the left, while the effects, such as injuries, asset or environmental damage are shown on the right. The prevention barriers are then between the threats and the top event, while the mitigation barriers are between the top event and the outcome.

The bow tie risk model can address hardware, administrative and procedural controls, either on the main pathways as shown in the simplified diagram of Figure 6, or on separate branches [5]. The bow tie is a simplified representation of a fault tree diagram where each barrier is an AND gate with two inputs – a demand AND barrier fails. An escalation branch is just building out the barrier fails arm from an undeveloped event to one that is developed – showing the means in place to maintain that barrier. A requirement of fault trees and thus of bow ties is an assumption of barrier independence.

Human intervention can cause degradation of many barriers if their intention is to reduce time or resources from what was originally planned. A system with multiple barriers can in fact has fewer if resources are not devoted to maintaining them. The bow tie, like the fault tree, is poor at capturing these overarching influences, but they important to overall system safety and a systems process is important [3].

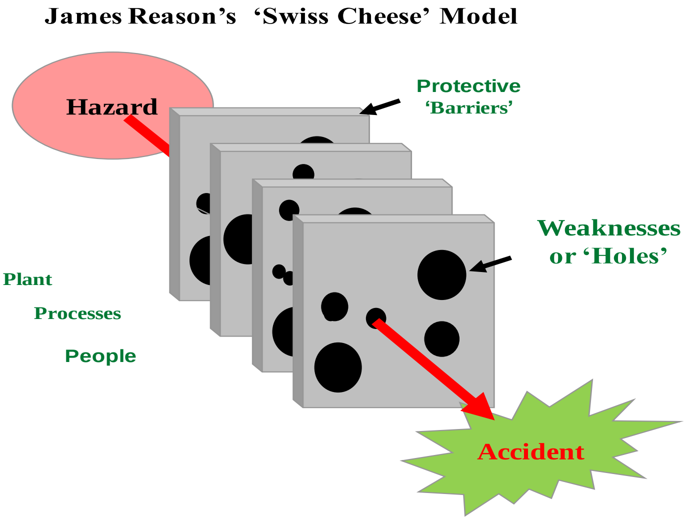

Figure 6: Reason’s Accident model

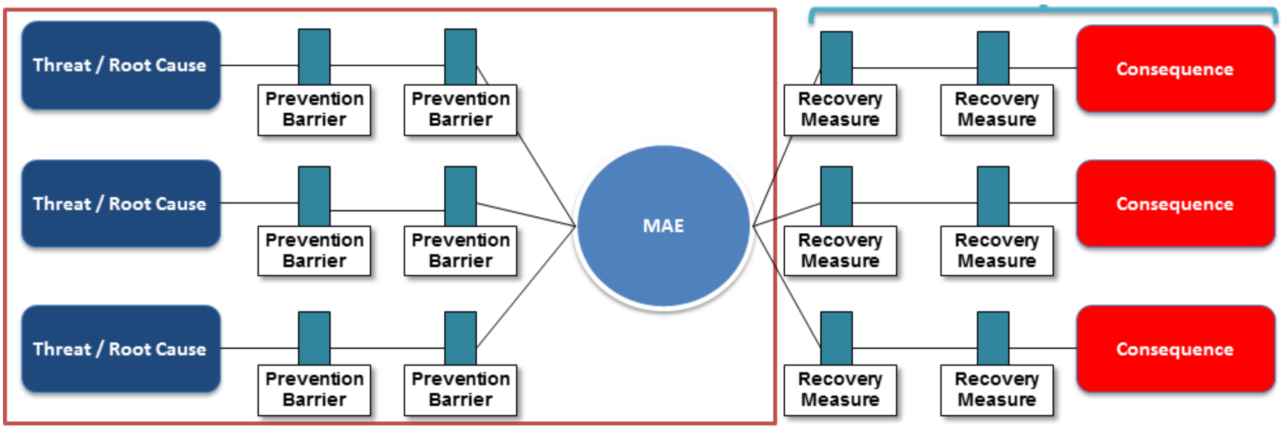

Figure 7: A typical bow-tie model

There are three levels of well control: primary, secondary and tertiary. Primary refers to control during the drilling phase with mud weight. Secondary refers to well control with a blowout preventer, and tertiary refers to a worst-case scenario – a blowout. Conventional well-control strategies include casing, fluid programs, and other barriers to well control incidents in the well design and BOP, and other mitigation procedures that help minimize the impact of an incident should one occur. The primary barrier is the hydrostatic pressure of mud which is larger than of the pore pressure. In underbalance drilling, this barrier must be adjusted. In this case it is composed of the drilling fluid column and a separate back pressure choke. The secondary barrier is the envelope consisting of the blowout preventer, the casing, the exposed wellbore below the casing shoe and the drill string. If the primary barrier is failed, this barrier is closed.

Conclusions

The purpose of risk analysis is to obtain robust design. Risk analysis identifies all factors which influences a design. Measuring risks is essential to reduce exposure, and it can be used for other purposes such as upgrading an existing drilling rig for life extension, change of use, reducing corporate risk exposure or measuring cost effectiveness of expenditures. The proposed approach is an effective tool for such purposes.

We used the risk matrix to filter out less important hazards and AHP to rank the remaining hazards by eliciting opinion of several experts [4]. Opinions of several experts can be aggregated after going through the process described above and then averaging the calculated ranks. Such averaging may be done before processing the data. Using fuzzy mathematics was also proposed for aggregation in the literature, but their value is uncertain as AHP itself is dealing with fuzzy situation and it is doubtful if further complication would add value. There are other methods for aggregation [6] which involve more calculations.

The AHP is a versatile decision aid which can handle problems involving both multiple objectives and uncertainty. It is popular with many decision makers who find the questions it poses easy to answer. It should, however, not be forgotten that the purpose of any decision aid is to provide insights and understanding, rather than to prescribe a "correct" solution. Often the process of attempting to structure the problem is more useful in achieving these aims than the numeric output of the model.

References

1- Kaplan, S. and B.J. Garrick, B.J., *On the Quantitative Definition of risk*, 1981, Risk Analysis Vol. l (1), pp11-27, 1981.
2- Kaplan, S., Haimes, Y.Y. and Garrick, B.J., *Fitting hierarchical holographic modelling (HHM) into the theory of scenario structuring and a refinement to the quantitative definition of risk*, Risk Analysis, Vol.21 (5): pp 807-819, 2001.
3- Leveson N., *Applying systems thinking to analyse and learn from events, Safety Science*, Vol.49, pp 55–64, 2011.
4- Ouchi, F., *A Literature Review on the Use of Expert Opinion in Probabilistic Risk Analysis*, World Bank Policy Research Working Paper 3201, February 2004, last accessed 23/03/2015. http://wwwwds.worldbank.org/external/default/WDSContentServer/WDSP/IB/2004/04/15/000009486_20040415130301/additional/115515322_20041117173031.pdf
5- Pitblado, R. and Nelson, W. R., *Advanced Safety Barrier Management with Inclusion of Human and Organizational Aspects*, Chemical engineering transactions Vol. 31, 2013. http://www.aidic.it/cet/13/31/056.pdf
6- Ramanathan, R. and Ganesh, L. S., *Group preference aggregation methods employed in the AHP: an evaluation and an intrinsic process for deriving members*, European Journal of Operational Research 79, 249–265, 1994.
7- Ramanathan, R., *A note on the use of the analytic hierarchy process for environmental impact*

assessment R. Journal of Environmental Management Vol.63, pp 27–35, 2001.

8- Saaty, T.L., *The analytic hierarchy process*, New York- McGraw Hill 1980.

9- Saaty, T., *How to make a decision: the analytic hierarchy process*, European journal of operational Research, Vol. 48(1): 9-26, 1990.

10- Yasseri, S., *Subsea technologies selection using analytic hierarchy process*, International journal of underwater technology, Society for Underwater Technology, Volume 30, Number 3, pp. 151-164, 2012.

INTERNATIONAL JOURNAL OF
COASTAL & OFFSHORE ENGINEERING

IJCOE Vol.2/No. 1/Spring 2017 (27-32)

Available online at: http://ijcoe.org/browse.php?a_code=A-10-86-1&sid=1&slc_lang=en

Subsea Corrosion Management: Challenges and Limitations

Reza Javaherdashti

Director, Parscorrosion Consultants, Perth, Australia; javaherdashti@yahoo.com

ARTICLE INFO

Article History:
Received: 15 Nov. 2016
Accepted: 9 Mar. 2017

Keywords:
Subsea structures
Integrity
Corrosion prediction models
CRA
Cathodic protection

ABSTRACT

Subsea structures such as manifolds, line pipes and flow lines are important investments. Also because of the sensitivity of environmental issues, corrosion of these structures is of vital importance. Subsea corrosion management is different from on-shore and shallow water off-shore corrosion management in mainly three factors: materials, corrosion management practice and cathodic protection. There are important limitations in many aspects of these three factors that make them different from their “counterparts” in other industries. In this paper, some of these differences especially with regards to corrosion prediction softwares and associated design strategies are addressed and discussed.

1. Introduction

Deep sea oil and gas industry is becoming more and more an attractive option for energy-thirsty industry. In addition to its various economical benefits, it also has its dangerous downsides, mainly ecological. With no doubt corrosion is a significant issue in these structures that can lead into ecological disasters. Any failure in the deep sea structures (manifold, line pipe, flow lines …) could be disastrous. Unlike on-shore structures or even shallow water structures, the access for regular monitoring and repair is not an easy option, in terms of both the cost and the accessibility. Therefore corrosion management for the subsea structures mostly rely on the estimation of corrosion rates. These corrosion rates themselves are calculated based on semi-experimental research results and therefore, are always limited in terms of their assumptions and applications. In this paper we will review some important features of deep sea corrosion issues and the main counter-measures to address such issues.

2-Some of the highlights for the corrosion management of deep sea structures:

There are mainly three aspects of deep sea structures corrosion management (DSCM) that make them different from on-shore and shallow water structures corrosion management (OF/SW CM) techniques:

- Materials
- Corrosion Management Practice
- Cathodic Protection

These three issues are important in the sense that when they are taken together, they can define the job description of a typical subsea corrosion engineer and differentiate it from that of a, say, corrosion engineer who works in mining industry.

Materials

The variety of materials that are used in OF/SW CM applications is not seen with DSCM. This is in fact dictated by the corrosion models and their underlying design philosophy. The materials of frequent use in pipes for subsea applications are [1]: (carbon) steel, stainless, duplex and superduplex stainless steels, clad and titanium pipes. A more general classification of t he materials can be either:

-Carbon steel (clad or lined)
-Corrosion resistant alloys (CRA) such as but not limited to duplex stainless steels (DSS)

Clad steel plate is a composite steel plate made by (metallurgical) bonding the cladding material (such as all types of stainless steels, nickel and nickel-copper alloys and Titanium) to either or both sides of a carbon steel or low alloy steel plate (base metal). While different methods may be used to apply the cladding, both the economy and the available sizes of the final product are important factors, in addition to mechanical properties, that will affect the use of these materials. However, it must be noted that as application of these methods can change the overall microstructure, it can have some unwanted effects as well: a study on stainless-cladded carbon steels by hot-rolling shows that the following changes in the bimetallic microstructure has happened [2]:
-formation of a decarburized region near the carbon steel side,

- a hardened region with high carbon content at the stainless steel side where a partial Cr depletion had occurred.

These micro structural changes along with the formation of residual stresses –which mostly have tensile natures- can be leading into premature failures.

An example of CRA is duplex stainless steel. These steels are mainly charcterised by their “dual” crystal structure, Figure 1:

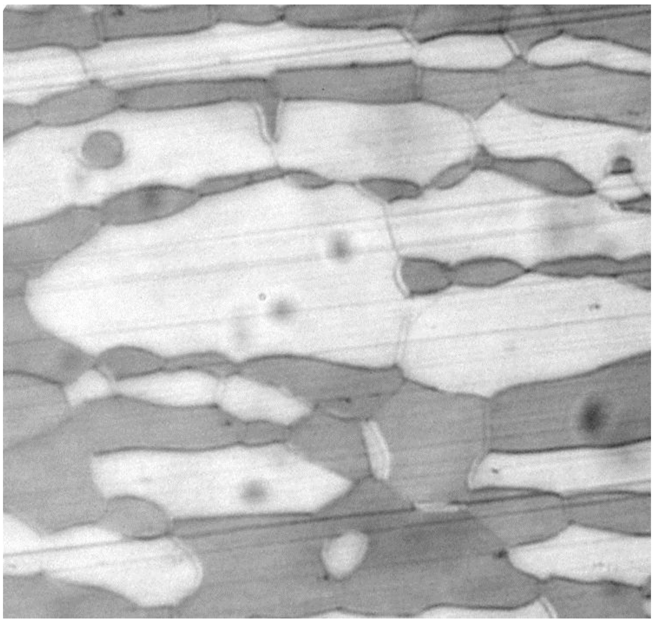

Figure 1. An example of the microstructure of a duplex stainless steel (SAF2205): (bright: austenite, dark: ferrite). The structure shows 52 ± 2 wt% retained austenite.

Duplex stainless steels are taken more corrosion resistant than austenitic stainless steels owing to their relatively higher chromium content. A very important issue with duplex stainless steels is the spacing between austenite islands as short austenite spacing is normally preferred due to both shorter hydrogen diffusion paths, more “hydrogen” tapping and crack stop properties [3].To avoid hydrogen induced stress cracking (HISC), based on deformation mode and induced strains, an austenite spacing from less than or equal to 30μ to 60 μ [4].

Corrosion Management:

Corrosion management includes items such as corrosion allowance, corrosion models and inhibitor availability and the like.

In contrast to many on-shore corrosion management techniques, subsea corrosion management still applies “corrosion allowance”. This is in essence the extra thickness of the pipe wall to compensate for corrosion. While it may appear as a simple issue of just adding “a few” millimeter to the net thickness of the pipe (to get the nominal thickness), this corrosion management technique has huge economical and application impacts, a rather “classical” example in this regard is for a pipe line of 8-in. diameter and 225 miles (~362 km) long and a wall thickness of 0.322 inches, by increasing the thickness by only 0.250 inches, an extra 3700 tons of steel will be needed as well as well as decreasing the internal capacity by 5% [5].

Corrosion modeling and inhibitor availability are the main two features that define the main differences between corrosion prediction models [6]. In these models the type of inhibitor (cathodic, anionic or mixed) is of no importance and the assumption is that whatever the mechanism of action, it is the availability of the inhibitor that matters. Corrosion models can be classified into two groups, “conservative” BP (Cassandra) and NORSOK (and their various in-house alternatives) and rather “liberal” Shell model [6]. Figure 2 schematically shows some of the features of these modeling approaches:

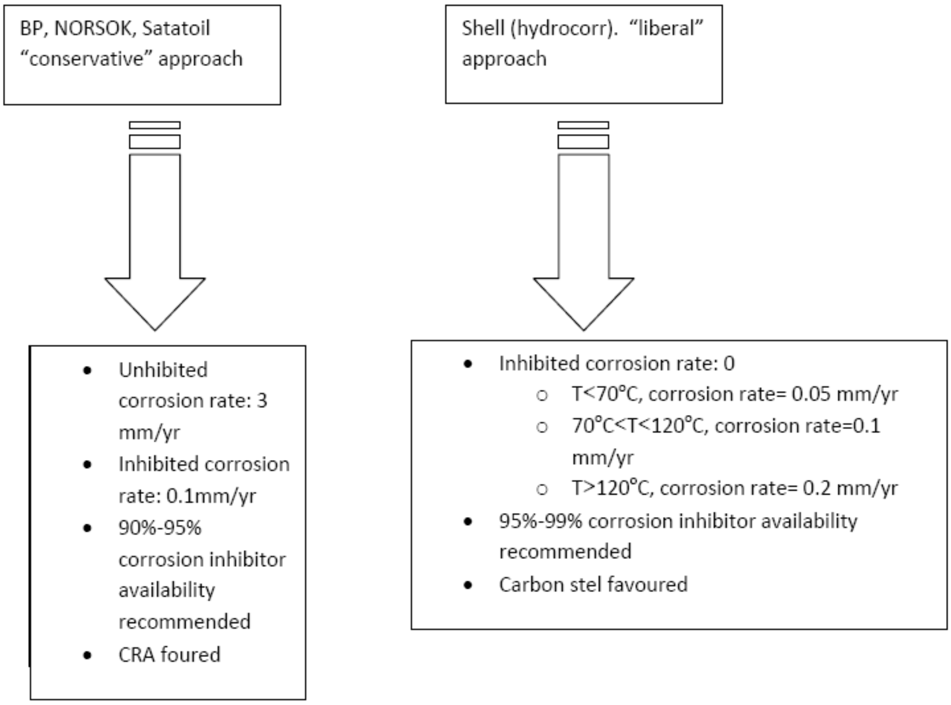

BP, NORSOK, Satatoil “conservative” approach

- Unhibited corrosion rate: 3 mm/yr
- Inhibited corrosion rate: 0.1mm/yr
- 90%-95% corrosion inhibitor availability recommended
- CRA foured

Shell (hydrocorr). “liberal” approach

- Inhibited corrosion rate: 0
    - T<70°C, corrosion rate= 0.05 mm/yr
    - 70°C<T<120°C, corrosion rate=0.1 mm/yr
    - T>120°C, corrosion rate= 0.2 mm/yr
- 95%-99% corrosion inhibitor availability recommended
- Carbon stel favoured

Figure 2. Schematic comparison between two most frequently used corrosion prediction models for subsea structures

Although so-called BP model is based on papers published by de Waard [7]-[8] , and they essentially show similar results, there are slight differences between the model and the work by de Waard, in issues such as use of a correction factor for carbon dioxide fugacity and its lack in the BP model [9]. Figure 3 shows a typical input for a BP 93 (flow insensitive) model:

Assumptions:	- Hold up conservatively assumed to be all water. - DW pH model has been used - We assume a total shear stress of 1 Pa. -The values given for TOL BP93 have been calculated based on the assumption that it is top of line condensing corrosion only and that wetting occurs only 10% of time (F=0.1).
CO_2	Value in mol.%
H_2S	Value in mol.%
pH Model	DW
Glycol	Value %
Internal Diameter	Value in m
Water SG (specific gravity)	(Normally accepted as 1.00)_
Acetates as acid?	False/True
Water Chemistry (mg/l)	Na, K, Ca, Mg, Sr, Ba, Fe, Cl, SO_4, HCO3

Figure 3. Typical Input data for a BP 93 Cassandra corrosion prediction model

The Norwegian NORSOK model, de Waard model and the BP model predict the same corrosion rates at temperatures below or equal to scaling temperature, after the scaling temperature these models will predict corrosion rates that can be different from each other (Figure 4) , and thus will dictate different strategies.

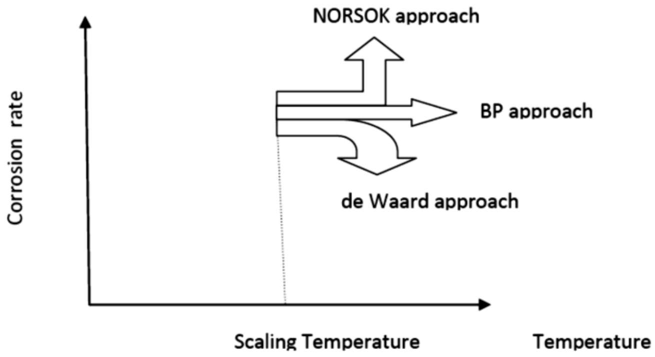

Figure 4. Corrosion rates as predicted by three models for temperatures above scaling temperature (NORSOK, by default, calculates ferrous ions unsaturated rates).

To illustrate how the same data can result in different corrosion management strategies according to these models, Marsh and Teh consider the example of 100,000ppm sodium chloride brine with 500ppm of bicarbonate ions, 100bara, 5% CO2 (gas phase), 100oC, No significant flow effects considered, 20 year design life. In addition, we can take In this example, Cassandra model by assuming 95% availability upper limit, inhibited corrosion rate 0.1mm/yr will recommend the use of CRA (such as 13% Cr supermartensitic stainless steel or SAF 2205) whereas for the same set of data, NORSOK M-506 by assuming 99% availability upper limit, inhibited corrosion rate 0.05/0.1 mm/yr (65oC/100oC) recommends carbon steel with 3mm corrosion allowance. Considering that the average costs of 13% Cr supermartensitic stainless steel and SAF 2205 are, respectively, 4 and 10 times of carbon stel, the readers can easily calculate that the economic impact of differences in corrosion rate calculations and design philosophies. In addition to de Waard, Cassandra and NORSOK, there are other corrosion prediction models such as [10] Cormed (Elf), Lipucorr (Total), Predict (InterCorr), CorPos (CorrOcean/FORCE Technology), as it can be expected while all these models have the same basics, the input and results will differ.

One important shortcoming of corrosion prediction models is that in models such as BP, deWaard and NORSOK, microbial corrosion is not considered. Cassandra [9] for example, is not valid for liquid velocities less than 1.5 $ms^{-1.}$ It is interesting to know that this is also the velocity limit where microbial corrosion can be expected [11]. Even the standards frequently used in subsea corrosion management (such as DNV) [12] do not address microbial corrosion properly. This matter becomes important when we consider that microbial corrosion has been shown as a cause of failure in subsea structures [13].

Table 1. Methods and techniques for corrosion monitoring

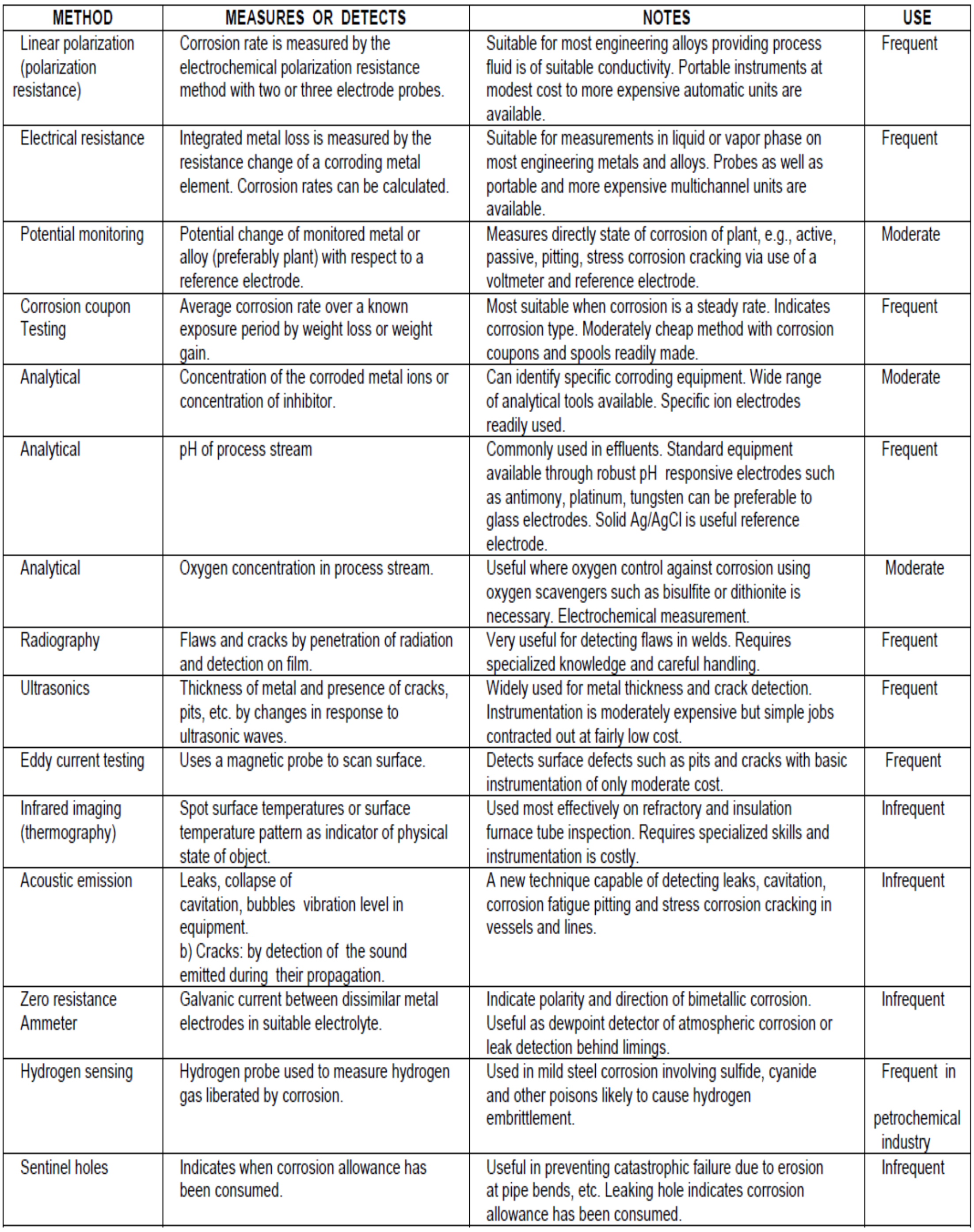

METHOD	MEASURES OR DETECTS	NOTES	USE
Linear polarization (polarization resistance)	Corrosion rate is measured by the electrochemical polarization resistance method with two or three electrode probes.	Suitable for most engineering alloys providing process fluid is of suitable conductivity. Portable instruments at modest cost to more expensive automatic units are available.	Frequent
Electrical resistance	Integrated metal loss is measured by the resistance change of a corroding metal element. Corrosion rates can be calculated.	Suitable for measurements in liquid or vapor phase on most engineering metals and alloys. Probes as well as portable and more expensive multichannel units are available.	Frequent
Potential monitoring	Potential change of monitored metal or alloy (preferably plant) with respect to a reference electrode.	Measures directly state of corrosion of plant, e.g., active, passive, pitting, stress corrosion cracking via use of a voltmeter and reference electrode.	Moderate
Corrosion coupon Testing	Average corrosion rate over a known exposure period by weight loss or weight gain.	Most suitable when corrosion is a steady rate. Indicates corrosion type. Moderately cheap method with corrosion coupons and spools readily made.	Frequent
Analytical	Concentration of the corroded metal ions or concentration of inhibitor.	Can identify specific corroding equipment. Wide range of analytical tools available. Specific ion electrodes readily used.	Moderate
Analytical	pH of process stream	Commonly used in effluents. Standard equipment available through robust pH responsive electrodes such as antimony, platinum, tungsten can be preferable to glass electrodes. Solid Ag/AgCl is useful reference electrode.	Frequent
Analytical	Oxygen concentration in process stream.	Useful where oxygen control against corrosion using oxygen scavengers such as bisulfite or dithionite is necessary. Electrochemical measurement.	Moderate
Radiography	Flaws and cracks by penetration of radiation and detection on film.	Very useful for detecting flaws in welds. Requires specialized knowledge and careful handling.	Frequent
Ultrasonics	Thickness of metal and presence of cracks, pits, etc. by changes in response to ultrasonic waves.	Widely used for metal thickness and crack detection. Instrumentation is moderately expensive but simple jobs contracted out at fairly low cost.	Frequent
Eddy current testing	Uses a magnetic probe to scan surface.	Detects surface defects such as pits and cracks with basic instrumentation of only moderate cost.	Frequent
Infrared imaging (thermography)	Spot surface temperatures or surface temperature pattern as indicator of physical state of object.	Used most effectively on refractory and insulation furnace tube inspection. Requires specialized skills and instrumentation is costly.	Infrequent
Acoustic emission	Leaks, collapse of cavitation, bubbles vibration level in equipment. b) Cracks: by detection of the sound emitted during their propagation.	A new technique capable of detecting leaks, cavitation, corrosion fatigue pitting and stress corrosion cracking in vessels and lines.	Infrequent
Zero resistance Ammeter	Galvanic current between dissimilar metal electrodes in suitable electrolyte.	Indicate polarity and direction of bimetallic corrosion. Useful as dewpoint detector of atmospheric corrosion or leak detection behind limings.	Infrequent
Hydrogen sensing	Hydrogen probe used to measure hydrogen gas liberated by corrosion.	Used in mild steel corrosion involving sulfide, cyanide and other poisons likely to cause hydrogen embrittlement.	Frequent in petrochemical industry
Sentinel holes	Indicates when corrosion allowance has been consumed.	Useful in preventing catastrophic failure due to erosion at pipe bends, etc. Leaking hole indicates corrosion allowance has been consumed.	Infrequent

3- The Concept of Corrosion Monitoring for subsea structures

The concept of corrosion monitoring has developed from two distinct areas, plant inspection techniques and laboratory corrosion testing techniques, with the original aim of assessing or predicting corrosion.

Use of Corrosion Monitoring Data:

- **To provide operational or management information**

Corrosion can often be controlled by maintaining a single operational variable (e.g., temperature, pH, humidity) within limits determined by prior monitoring or other investigations. If the significant variable is measured for other reasons, this measurement can be used directly for corrosion control. If the variable is not otherwise measured, or in more complex cases where several variables interact, corrosion monitoring information can be used by plant operators to control plant operation so as to control corrosion. Any process change may have significant effects on corrosion, and corrosion monitoring techniques allow full scale trials to proceed with a minimum of risk to plant.

- **Corrosion Monitoring Techniques**

A wide range of corrosion monitoring techniques is now available allowing determination of total corrosion, corrosion rate, corrosion state, analytical determination of corrosion product or active species, detection of defects or changes in physical parameters. Associated costs can be small where simple instrumentation and a few measurements are appropriate but in some cases may be extremely costly and require expert skills.

Much of the progress which has been made in the past few years has been due to advances in electronics which have allowed multiprobe measurement and recording at a tolerable cost. Instantaneous feedback of corrosion information can be obtained from various parts of the plant, which can be fed to the plant control room and/or plant computer to permit control of the necessary process variable to provide corrosion control. Table 1 indicates corrosion monitoring techniques

- **Selecting a Technique for Corrosion Monitoring**

Many techniques have been used for corrosion monitoring (see Table 1), it is clearly possible to develop others. Consequently when a possible new application is being considered, a problem arises in choosing the most appropriate technique. Each has its strong points and its limitations, and none is the best for all situations.

Any monitoring technique can provide only a limited amount of information, and the techniques should be regarded as complementary rather than competitive. Where more than one technique will give the information required, the information is obtained in different ways; a cross-check can be valuable and differences in detail can add meaning.

A corrosion monitoring technique rarely gives wrong information, unless the equipment used is faulty. "Nonsense" results arise because the information is correct, but irrelevant in the corrosion sense.

The polarization resistance method, for example, measures the combined rate of any electrochemical reactions at the surface of the test sample. If the main reaction is the corrosion ones, the rate measured is the corrosion rate. If however, other reactions are possible at rates that are comparable or greater, the measured rate includes the other reactions. Useful deductions can still be made provided it is recognized that the corrosion rate has not been measured. The choice of a monitoring technique is a complex problem requiring expert knowledge. The first essential is to establish what type of information is needed. This necessarily involves an input from the management of the plant in question.

Cathodic Protection

For obvious reasons, impressed current CP cannot be an option for deep sea water applications. According to DNV- OS-F101 [14], “duplex and martensitic stainless steel linepipe, and C-Mn steel linepipe with SMYS > 450 MPa require special considerations of the susceptibility of environmentally assisted cracking (including SSC and hydrogen induced cracking related to cathodic protection)”.

NORSOK workshop agreement [4] seems more detailed about the joint use of CP and duplex stainless steels. According to this document duplex stainless steels are well protected for potentials more negative than -600 mV (Ag/AgCl) on the condition that a complete electrical insulation from the structural elements, that are protected at -1050 mV, is also applied. Although some modifications in CP system design may be promising in using both CP and supermartinsitic stainless steel together [15]. As it can be seen, two major limitations on applying CP to subsea structures are that only one method of CP can be applied and that we are limited to use of certain alloys whose yield stress is lower than a certain limit.

4- Conclusion

Subsea structures like on-shore and other off-shore (shallow water) structures need to be protected from corrosion. However the practice of corrosion management for these structures is different from on-shore and off-shore in not only the materials used but also in applications such as cathodic protection. Due to factors such as difficulty in having access to the subsea structures and the costs involved, different corrosion prediction models have been developed. These models-with their in-house variants- are frequently used in not only estimation of corrosion but also selecting the strategy that will be the most feasible one to apply. Although these models have similar basics, due to their assumptions and conservative approaches , the very same inputs may result in different corrosion ,management strategies and therefore different budgeting for the projects. When applying these models, their limitations must be considered and their approaches must be taken with required precautions.

5- References

1. Guide for building and classing subsea pipeline systems-Chapter 2, Section1, American Bureau of Shipping (ABS), Houston, TX, USA, May 2006 (updated March 2008).
2. S. Missori, F. Murdolo, A. Sili, *Microstructural Characterisation of a stainless steel-cladded carbon steel*, Metallurgical Science and Technology, Vol.19.No.2, December 2001, p.21-24.
3. V. Olden *FE modeling of hydrogen induced stress cracking in 25% Cr duplex stainless steel*, PhD Thesis, Norwegian University of Science and Technology, Trondheim, August 2008.
4. *Design guideline to avoid hydrogen induced stress cracking in subsea duplex stainless steel*, NORSOK Workshop Agreement-HISC Guideline for duplex stainless steel-M-WA-01, Rev.1, October 2005
5. H.H. Uhlig, *Corrosion and corrosion control*. 2nd edn. John Wiley & Sons, West Sussex, England, 1971.
6. J. Marsh and T. The, *Conflicting Views: CO2 Corrosion Models, Corrosion Inhibitor Availability Philosophies, and the Effect on Subsea Systems and Pipeline Design*, SPE 109209, Offshore Europe 2007, Aberdeen, Scotland, U.K., 4–7 September 2007.
7. C. de Waard, U. Lotz, D.E. Milliams, *Predictive model for CO_2 corrosion engineering in wet natural gas pipelines*, Corrosion, Vol.47, No.12, December 1991, pp.976-985.
8. C. de Waard, U. Lotz, *Prediction of CO_2 corrosion of car bon steel*, NACE CORROSION'93, Paper 69, March 1993, New Orleans, 1993, USA.
9. A. Petersen, R. Chapman, B. Hedges *Corrosion prediction with Cassnadra*, S/UTG/013/03, bp Upstream Technology Group Sunbury, 01/03/03.
10. R. Johnsen, *Corrosion of carbon steel in hydrocarbon environments*, Norwegian University of Science and Technology, 20/09/2005.
11. R. Javaherdashti, *Microbiologically influenced corrosion-An engineering insight*, Springer, 2008, UK.
12. R. Javaherdashti, *MIC myths: Avoiding common pitfalls in the practice of hydrotesting and likelihood of Microbial induced corrosion*, Corrosion Management, January-February 2009.
13. X. Wang, J. Duan, Y. Li, J. Zhang, S. Ma, B. Hou, *Corrosion of steel structures in sea-bed sediments*, Bulletin of Materials Science, Vol.28, No.2, pp.81-85, April 2005.
14. Offshore Standard DNV- OS-F101, Section 5, B 507, Det Norske Veritas, Norway, January 2000.
15. S. Eliassen, *New concept for cathodic protection of offshore pipelines to reduce hydrogen induced stress cracking (HISC) in high strength 13% Cr stainless steel*, Corrosion Engineering, Science, and Technology, Vol.39, No.1, pp.31-37, 2004.

INTERNATIONAL JOURNAL OF
COASTAL & OFFSHORE ENGINEERING

IJCOE Vol.2/No. 1/Spring 2017 (33-41)

Available online at: http://ijcoe.org/browse.php?a_code=A-10-90-1&sid=1&slc_lang=en

A 3D Numerical Study of Cyclone Gonu Waves Impact on Ramin Port

Fatemeh Hajivalie[1*], Ahmad Arabzadeh[2]

[1 *] *Corresponding author: Ocean Engineering and Technology Research Center, Iranian National Institute for Oceanography and Atmospheric Science (INIOAS), Tehran, IRAN, hajivalie@inio.ac.ir*
[2]*Persian Gulf Center- Boushehr, Iranian National Institute for Oceanography and Atmospheric Science (INIOAS), Boushehr, IRAN, ahmadarabzadeh@inio.ac.ir*

ARTICLE INFO

Article History:
Received: 28 Jan. 2017
Accepted: 9 Mar. 2017

Keywords:
TELEMAC-3D
Wave Overtopping
Wave Diffraction
Wave Penetration
Inundation

ABSTRACT

In this paper the TELEMAC-3D model has been hired to simulate and study the high waves' interaction with coastal structures. Therefore a special arrangement of TELEMAC-3D has been prepared in this study to simulate wave generation, coastal processes, wave set-up and overtopping over coastal structures. Experimental data has been used to verify this arrangement of the model. Thereafter, the model has been used to simulate the interaction of waves induced by Cyclone Gonu and Ramin Port breakwaters. Visually comparisons between images provided by Iran Fisheries Organization during the Gonu event and the TELEMAC3D results conclude that the numerical model could simulate the interaction of Gonu induced wave and Ramin breakwaters with a good accuracy. Different kind of results like inundation area, wave overtopping discharge over the breakwaters and wave penetration in port were obtained in this simulation.

1. Introduction

Cyclone Gonu (Fig. 1), June 2007, is the strongest cyclone among all tropical cyclones recorded in Arabian Sea since 1945, the year which recording began in this region. Most of tropical cyclones generated in Indian Ocean tend to travel to Oman in the West or Pakistan and India in the North and only their swell waves reach to Iranian Coasts, therefore Gonu was exceptional. It killed 49 people in Oman and 23 people in Iran [1] in spite of on time warning systems' public awareness and early evacuation; otherwise much more lives could be lost.

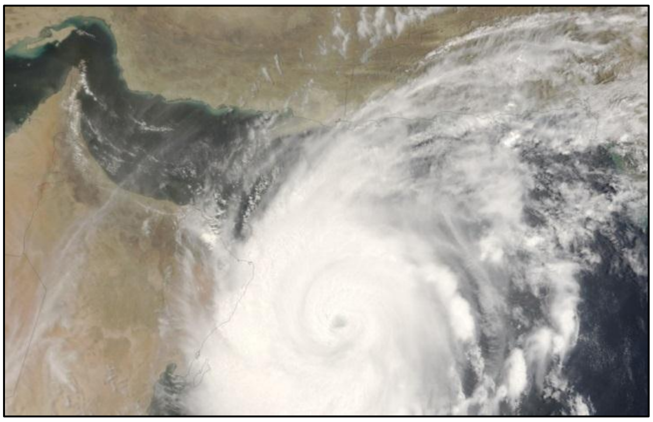

Figure 1. Cyclone Gonu (https://visibleearth.nasa.gov)

The maximum wind speed during Gonu on the Iranian Coast reached 58 km/h and about 4.5 m significant wave height was recorded outside of Chabahar bay in depth of 30 m, [1, 2].

After the Cyclone, The maximum watermark detected in the field observations was about 4 m above mean sea level in mud flats of Chabahar Bay [3]. On the other hand, on the Omani coast the inundation height reached up to 5 m [4].

Gonu is not the only powerful Cyclone reached to the Iranian Coasts; there are other evidences about strong cyclone crashing Iranian coasts before Gonu. The India Meteorological Department compiled an extensive summary of cyclonic storm tracks for the period from 1877 to 1970. Reviewing those tracks, four severe storms were identified to enter Oman Sea including storms happened in June 1889, June 1890, May 1898 and April 1901. However the "Best track" data of these events were weakened as they approached Iranian Coast. One might concluded that the Cyclone patterns has been changed due to climate change and made Gonu reach to Iranian Coast at a very strong situation [2].

Therefore strong Cyclone like Gonu may attack Iranian Coasts again in the future. That's why it is essential to estimate the effect of high waves induced by tropical cyclones on the Iranian coastal structures to check the design of existing structures and design the future structures.

This made many researchers to study the effect of cyclone Gonu on Iranian and Omani coastlines. Most of the studies were on the Gonu storm surge and inundation in both countries. Fritz et al. [4] observed the high water marks and inundation along Omani side in 2007 while Shah-hosseini et al [3] measured the water marks in Iranian side in 2008.

Khalilabadi and Mansouri [5] analyzed the hourly sea level recorded by tide gauges of the National Cartographic Center (NCC) at Jask and Bandar-Abbas to calculate the non-tidal sea level change during Gonu in Persian Gulf. Golshani and Taebi [1] numerically simulated Gonu and its resulting waves in the southern Iran using a time-dependent radius cyclone field and used the computed waves for extreme value analysis. Mashhadi et al. [6] also simulated the storm surges and wave characteristics during Gonu employing the SWAN and GETM models. However, to the authors' knowledge, there is no study on the effect of the Gonu induced wave on the coastal areas and structures.

Therefore in this this research, TELEMAC-3D has been hired to simulate wave generation, shoaling, refraction, diffraction, penetration as well as wave overtopping over coastal structures. The model has been verified based on Hsiao and Lin [7] experiments on solitary waves imping a seawall. After that, the interaction of high waves induced by the Cyclone Gonu with Ramin port breakwaters was simulated. The results then have been compared visually with the photos taken during the Cyclone in Ramin port. Ramin fishing port is located in the east of Chabahar, in the Southeast of Iran (Fig. 2). Its breakwaters were damaged by wave overtopping over them during Gonu event; however their stability was preserved (Fig. 3).

Figure 2. Aerial view of Ramin Port

Figure 3. Damaged in Ramin Port breakwaters resulted by wave overtopping during Gonu Cyclone

2. Numerical Model

2.1. Mathematical formulation

The TELEMAC-3D open source software is part of the TELEMAC modeling system developed and managed by a consortium of core organizations e.g. Artelia (France), Electricité de France R&D (EDF, France), and HR Wallingford (United Kingdom). TELEMAC-3D solves the RANS equations by the finite elements method through the vertical integration of the continuity equation and momentum equations [8].

$$\frac{\partial U_j}{\partial x_j} = 0 \qquad (1)$$

$$\frac{\partial U_j}{\partial t} + U_i \frac{\partial U_j}{\partial x_i} = -\frac{1}{\rho}\frac{\partial p}{\partial x_j} - g_j + \upsilon\Delta\left(U_j\right) + F_j \qquad (2)$$

U_i and U_j are velocity component in *i*th and *j*th coordinate directions (for three dimensional equations *i* and *j* =1, 2, 3), *p* is pressure, g_j= gravity acceleration in *j*th direction, ν_t kinetic eddy viscosity, ρ is water density. To simplify the solvation process, the pressure considered as the sum of hydrostatic pressure and a dynamic pressure term:

$$p = p_{atm} + \rho_0 g\left(\eta - z\right) + \rho_0 g \int_z^{Z_s} \frac{\Delta\rho}{\rho_0} dz + p_d \qquad (3)$$

Here, p_{atm} and p_d are the atmospheric and the dynamic pressure, η is the free surface elevation, ρ_0 is the reference water density. The turbulent viscosity can be estimated from a *k*-*ε* turbulence model. Thereafter the governing equations are:

$$\frac{\partial k}{\partial t} + U_j \frac{\partial}{\partial x_j} k = \frac{\partial}{\partial x_j}\left(\frac{\nu_t}{\sigma_k}\frac{\partial k}{\partial x_j}\right) + p - G - \varepsilon \qquad (4)$$

$$\frac{\partial \varepsilon}{\partial t} + U_j \frac{\partial}{\partial x_j} \varepsilon = \frac{\partial}{\partial x_j}\left[\frac{\nu_t}{\sigma_\varepsilon}\frac{\partial \varepsilon}{\partial x_j}\right] + C_{1\varepsilon}\frac{\varepsilon}{k}\left[P + \left(1 - C_{3\varepsilon}\right)G\right] - C_{2\varepsilon}\frac{\varepsilon^2}{k} \qquad (5)$$

$$P = \nu_t \frac{\partial \overline{U_i}}{\partial x_j}\left[\left(\frac{\partial \overline{U_i}}{\partial x_j} + \frac{\partial \overline{U_j}}{\partial x_i}\right)\right] \qquad (6)$$

$$G = -\frac{\nu_t}{\mathrm{Pr}_t}\frac{g}{\rho}\frac{\partial \rho}{\partial z} \qquad (7)$$

$$\nu_t = C_\mu \frac{k^2}{\varepsilon} \qquad (8)$$

where *k* is the turbulence kinetic energy, *ε* is the kinetic energy dissipation rate. *P* is a turbulence energy production term and *G* is a source term due to the gravitational forces. C_μ, Pr_t, $C_{1\varepsilon}$, $C_{2\varepsilon}$, $C_{3\varepsilon}$, σ_k and σ_ε are *k*-*ε* model contestants.

2.2. Model Verification

Since there was no nearshore wave measurement near the Ramin port during the Cyclone, the model has been verified against Hsiao and Lin [7] experiments on solitary waves imping a trapezoidal seawall on a sloped bed (Fig. 4). The physical characteristics of the selected experiment for the verification are summarized in Table (1). In this simulation, the bed and seawall act as rough wall. Slip boundary condition is used for the side walls and a variable free surface condition is placed as the wave generator in the inlet boundary.

After the simulation, the calculated water free surface configuration over the seawall has been compared with measurement data in four different stages of wave transmission over the seawall and illustrated in Fig. (5); as could be seen in the figure, TELEMAC-3D results have an acceptable accuracy. After testing the TELEMAC-3D accuracy in simulation of wave runup and overtopping over coastal structures, the model has been hired to simulate the runup and overtopping of Cyclone Gonu induced waves over Ramin port breakwaters.

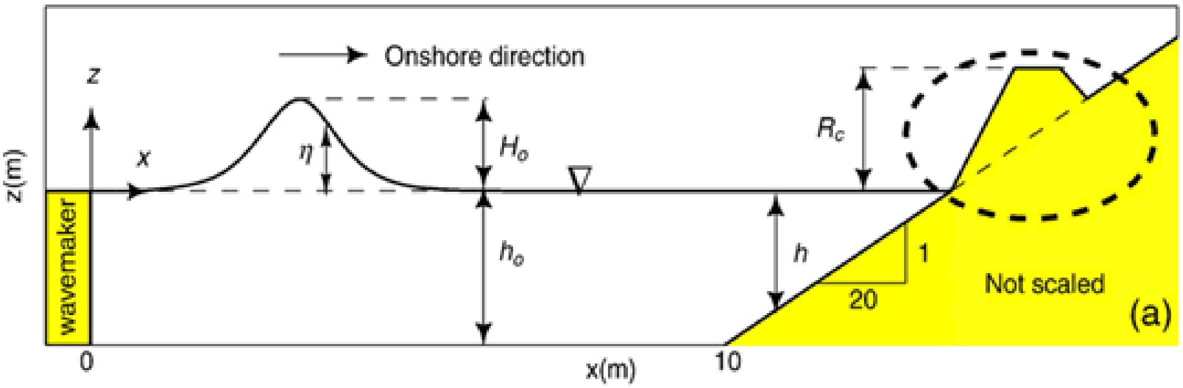

Figure 4. Sketch of wave flume layout [7]

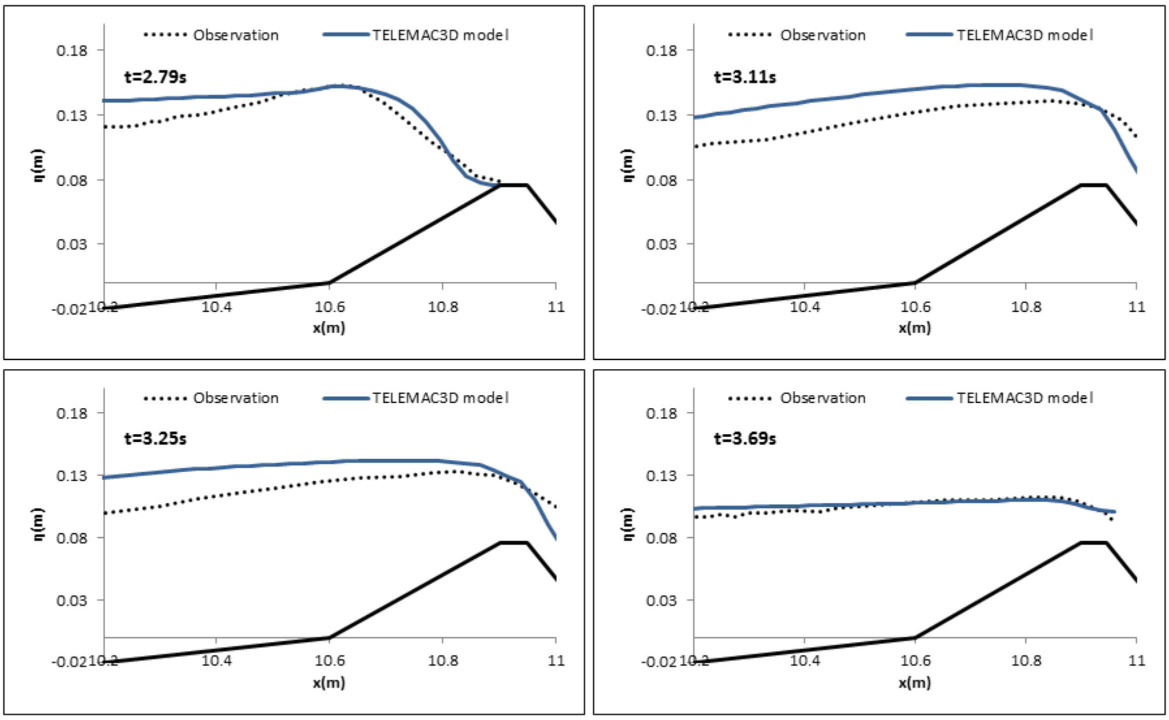

Figure 5. Comparison between numerical results and Hsiao and Lin (2010) experimental measurements

Table 1. The simulation characteristics based on Hsiao and Lin [7]

h_0 (m)	H_0 (m)	$\varepsilon = h_0 / H_0$	R_C (M)
0.2	0.07	0.35	0.056

2.2. Model Setup

To run the model, the local bathymetry and free surface elevation in addition to wave condition near the offshore boundary are necessary. For bathymetry data, Ramin port hydrography provided by Iran Fisheries Organization in 2005 has been used. The numerical domain was discretized to triangular mesh with mean side length about 10 m. To achieve higher accuracy, the mesh size decreased to about 1 m around the breakwaters (Fig. 6). As if it's a 3D domain, it is divided to 5 layers in vertical direction. This number of layer was chosen based on try and error. More layers increase computation time without meaningful changes in the results; while fewer layers couldn't calculate the wave propagation and transmission well.

The East and West boundary are introduced as slip boundary condition. In the South, the inlet boundary, a wave generator should be defined by introducing a time varying free surface elevation at the inlet boundary. At the time of Gonu event, an AWAC current and wave profiler had been installed in 25.261° N and 60.650° E in 30 m depth as a part of measurement tools installation during the project MONITOR SB&B by Ports and Maritime Organization of Iran. Fig.7 shows the time series of significant wave height, peak period and wave direction measured during Gonu event.

The AWAC was located about 9 km from the South boundary of the numerical domain used in this research and in the same depth, therefore its measurements was suitable enough to be used as the offshore boundary condition of this simulation. The simulations of Mashhadi et al. [6] also showed that the wave height in the location of the AWAC and the south boundary of our numerical domain was almost the same in different time steps of Gonu event. Therefore we have chosen these measurements as the input waves for the south boundary condition.

To start the simulation we also need the free surface elevation covering tide and storm surge effects. As long as there was a tide gage installed inside Ramin port at the time, there was no difficulty to obtain the free surface variations. Fig. 8 shows the water free surface variations during Gonu event. For the simulation, one of the most extreme situations has been considered which was observed in 2006/06/06; table 2 summarized the hydrodynamic parameters of this situation. In this table $\Delta\eta$ is the difference between mean sea - $\bar{\eta}$ - level and the free surface influenced by tide and storm surge. Considering the mean sea level equal 2.9 m based on the Ramin port design studies (Fig. 9) we have:

$$\eta=\bar{\eta}+\Delta\eta=2.9+1.5=4.4\text{ m} \tag{9}$$

Table 2. The hydrodynamics parameters for the simulation of Gonu induced wave crash on Ramin port breakwaters

$\Delta\eta$ (m)	*dir* (degree)	T_p (s)	H_s (m)
1.5	175	12.0	5.0

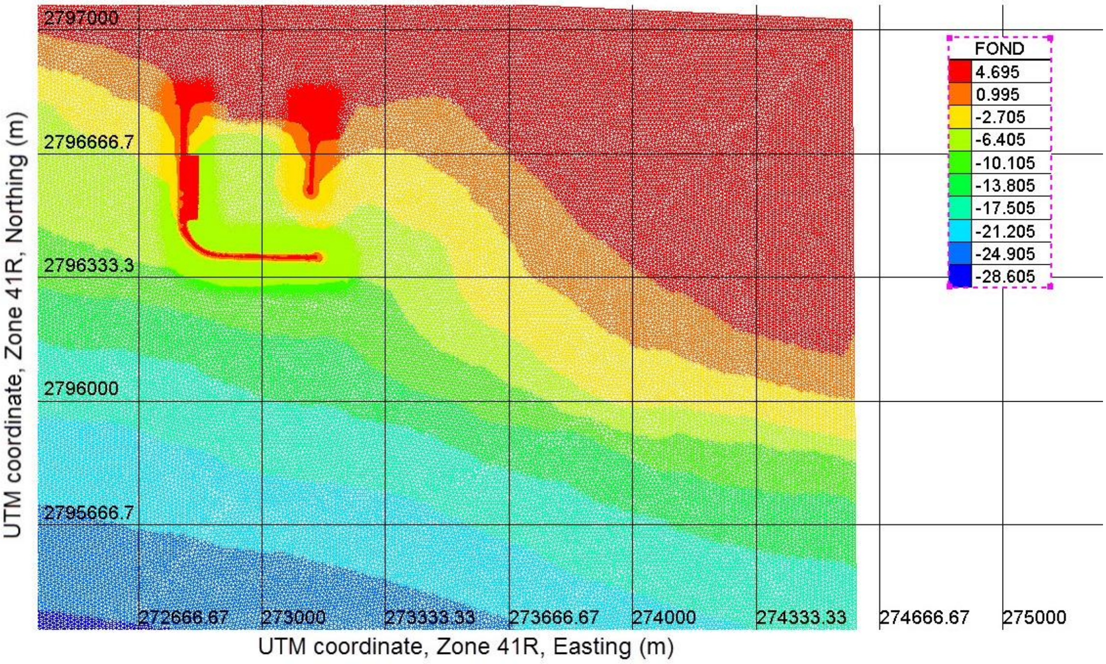

Figure 6. Computational grid for TELEMAC-3D based on Ramin port geomorphology

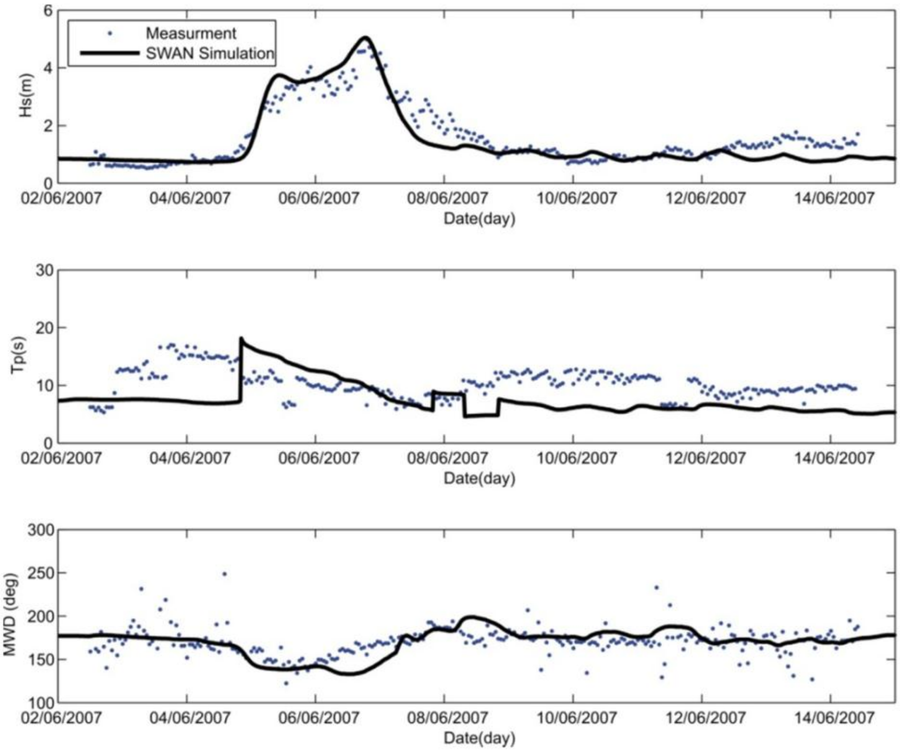

Figure 7. Significant wave height, peak wave period and mean wave direction measured by AWAC2 during Gonu event [6]

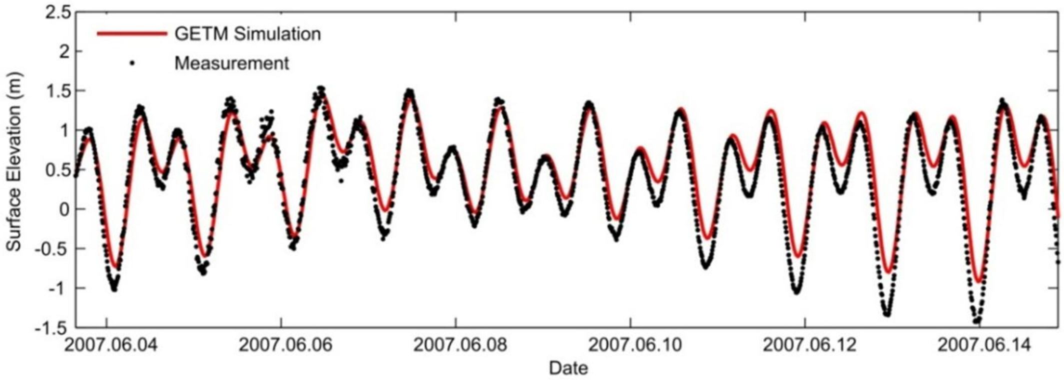

Figure 8. Free surface variation during Gonu event in Ramin port [6]

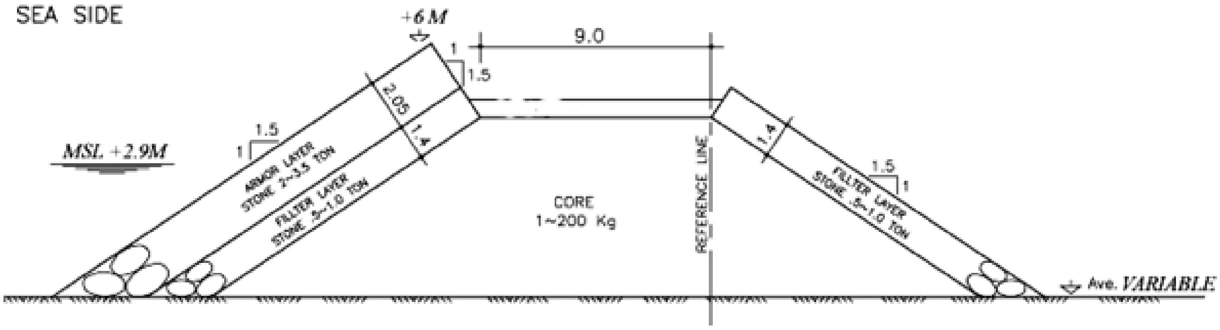

Figure 9. Ramin port breakwater sections versus sea levels

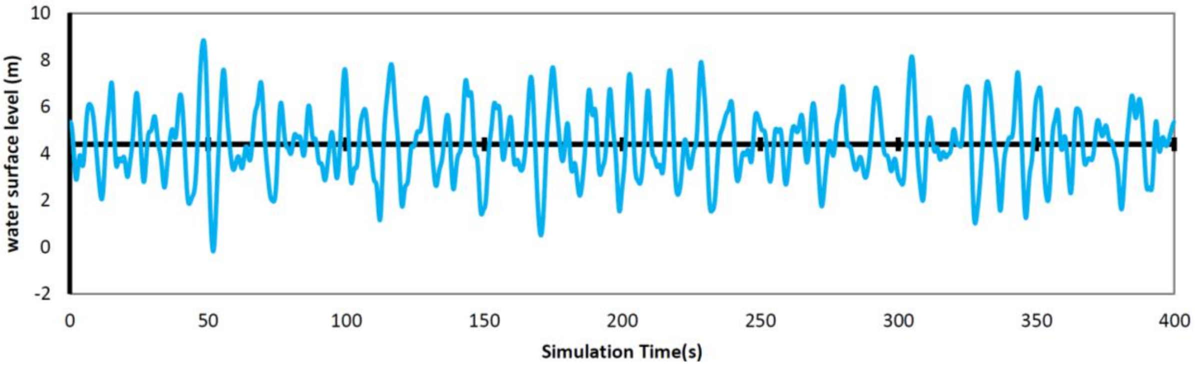

Figure 10. Free surface input time series

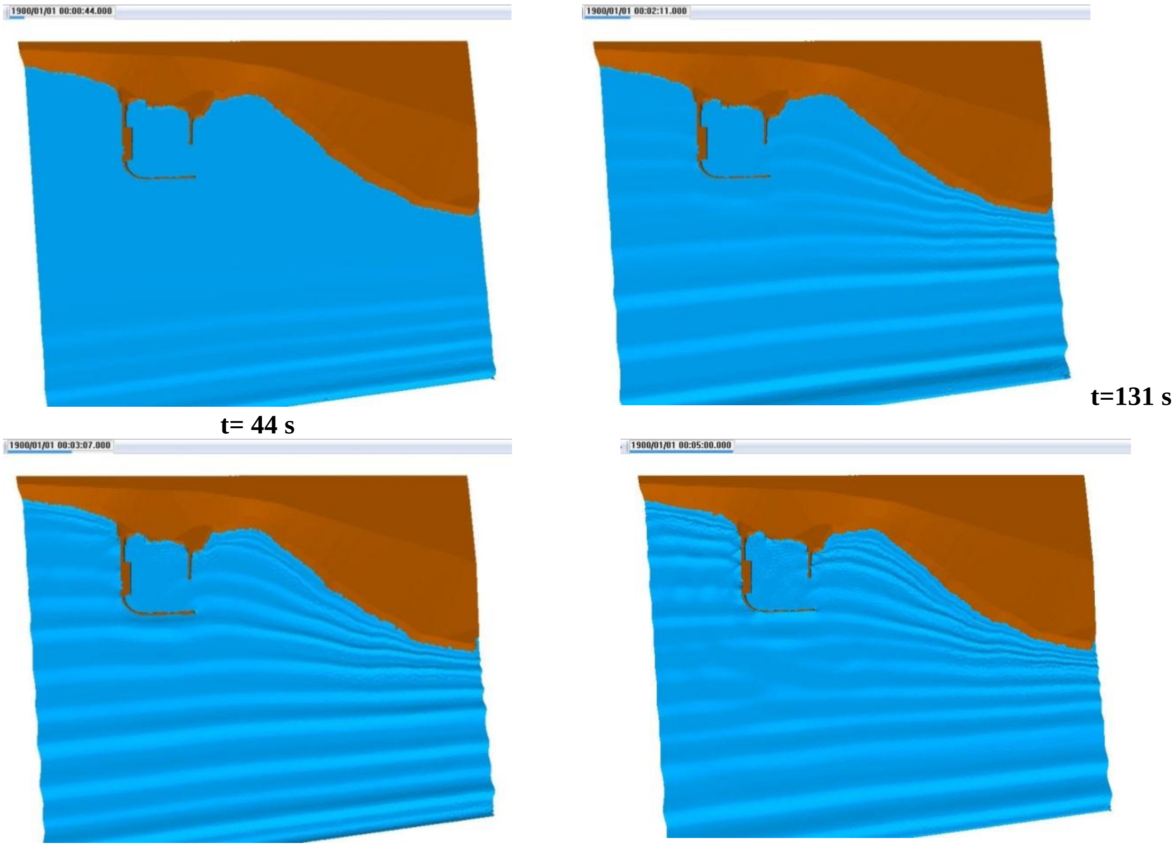

t= 44 s

t=131 s

t=187 s

t= 300 s

Figure 11. Wave propagation inside the numerical domain

Based on table 2 a wave time series based on JONSWAP wave spectrum was generate using WAFO module in MATLAB, this time series then has been used to introduce a time varying free surface boundary condition at the South boundary as illustrated in Fig. (10). At the bottom, a rough bed boundary condition has been considered.

The simulation start from still water condition which means the free surface elevation is set to mean water level. In addition zero velocities and hydrostatic pressure is considered in the entire domain as initial conditions.

4. Results and Discussion

The simulation was carried out for 5 minutes of the worst situation in Ramin port during the Gonu incident. Waves generated at the South boundary propagate inside the numerical domain. Fig. (11) shows us 3D views of free surface results in four different time steps of the simulation. As illustrated in the figure, waves start to response to the bed hydrography as they approaching the shoreline. At t= 187 s, wave diffraction is observed around the main breakwater tip. Also wave penetration inside the port basin is clear. At t=300, wave overtopping over the main breakwater is also recognizable.

To study the interaction of waves and breakwaters four different sections were selected in the simulation domain (Fig. 12). The maximum and minimum of the water line in the shore area is illustrated in this figure with two black continues lines. The maximum line can be considered as the inundation line. The variation of free surface can be extract in any location needed. For example Fig. 13 shows the free surface variation at Transect 2, Stations 1 to 6. As it could be seen in the figures, starting from Station 1 to Station 3, waves height reduces considerably during the reducing water depth, but as for Station 4, the water surface variations starts to get stronger as a result of interaction between waves and the main breakwater. In some points, water level exceeded 5.7 m which is the breakwater crest level. Station 5 is located inside the port basin, as one can see in the figure, the wave heights are less than 0.3 m there which show that the port remained almost calm during the simulation.

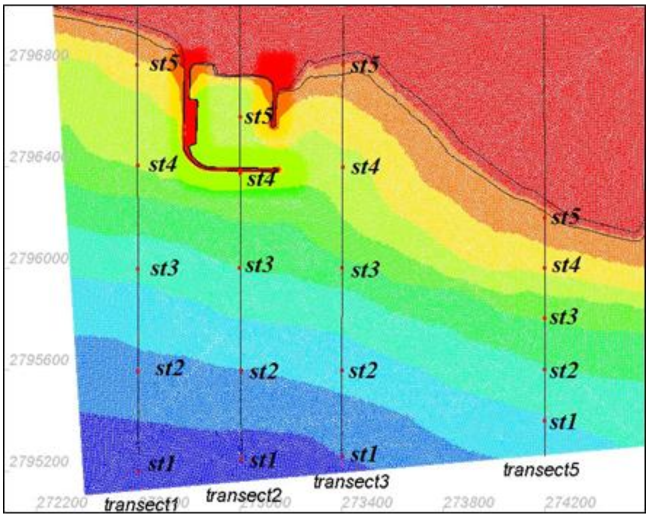

Figure 12. The selected sections for extracting outputs

Fig. (14) shows the maximum and minimum free water surface in front of the main breakwater at Transection 2. The wave overtopping over the breakwater can be observed clearly in this figure. The overtopping discharge can be estimated by multiplying average flow velocity and thickness of the water jet over the breakwater in each section. Fig. (15) shows this discharge for Transection 2. The maximum discharge reaches to 1.5 m^2/s in this section during the simulation.

Fig. 16 a and b show a comparison between 3D view of wave overtopping over the main breakwater and the photos taken by Iran Fisheries Organization; as it could be seen in this figure, the model results visually agree with the wave overtopping filmed in the port.

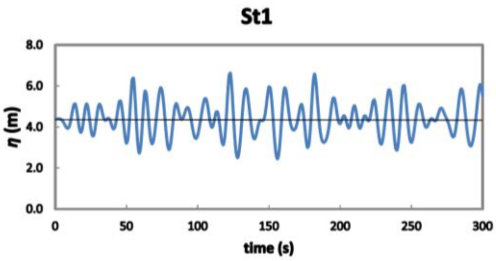

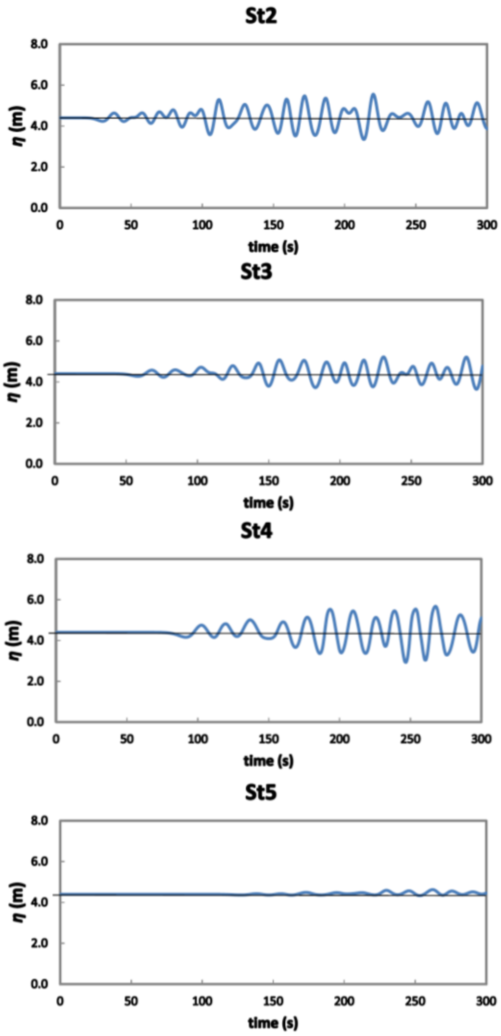

Figure 13. free surface variation in transection 2

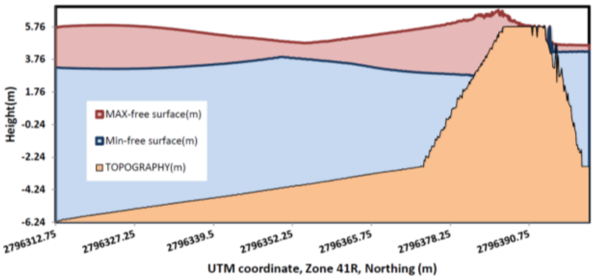

Figure 14. Maximum and Minimum free surface level in front of the breakwater, Transection 2

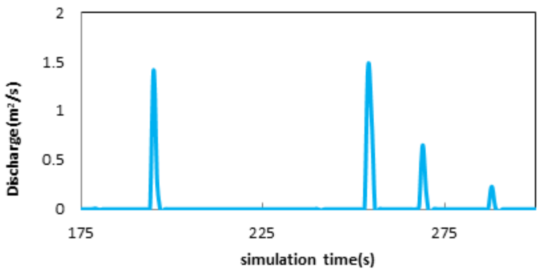

Figure 15. Overtopping discharge over the main breakwater, Transection 2

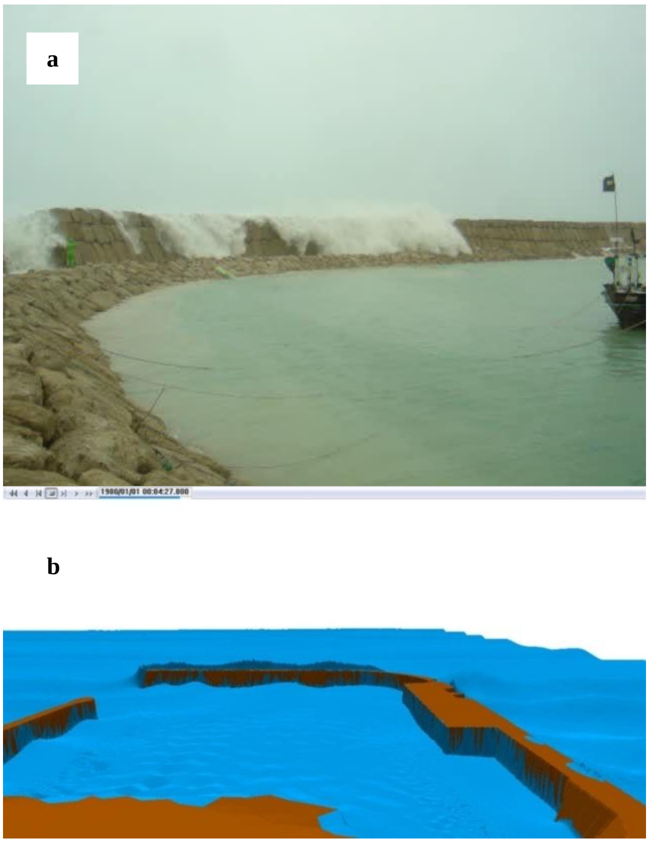

Figure 16. Comparison between a) real image of wave overtopping during the Gonu incident and b) the numerical results

5. Conclusions

TELEMAC-3D model has been hired for the first time to simulate high wave crash on coastal structures. For this simulation, Ramin port breakwaters were considered during Cyclone Gonu. The model was first verified versus Hsiao and Lin [7] experimental results because there wasn't any nearshore measurement during the cyclone. The simulation inputs were hydrography of Ramin port area, a variable free surface boundary condition as a wave generator in the South boundary and the free surface affected by storm surge. The 3D results show that the model was successful in simulating coastal process like wave shoaling, refraction and the diffraction at the tip of the breakwater.

Some wave overtopping was observed during the simulation which is in agreement with the videos taken by Iran Fisheries Organization videos during Gonu event. The overtopping discharge can be obtained from this simulation. It was also observed that in spite of wave diffraction and overtopping, the port basin was almost safe. According to this simulation, TELEMAC-3D could be hired in modeling of waves and coastal structure interactions as well as wave penetration inside ports and coastal process; however wave and current measurement are needed to verify and calibrate this model.

List of Symbols (Optional)

C_μ, Pr_t, $C_{1\varepsilon}$, $C_{2\varepsilon}$, $C_{3\varepsilon}$, σ_k and σ_ε	k-ε model contestants
g	Gravity acceleration
G	Source term due to the gravitational forces
k	Turbulence kinetic energy
p	Pressure
p_{atm}	Atmospheric pressure
p_d	Dynamic pressure
P	Turbulence energy production term
U_i	Fluid velocity in i^{th} direction
x, y, z	Coordinate directions
$\Delta\eta$	Difference between mean sea level and the free surface
ε	Kinetic energy dissipation rate
η	Free surface elevation
ν_t	Kinetic eddy viscosity
ρ	Water density
ρ_0	Reference water density

6. References

1- Golshani, A., Taebi, S., (2008), *Numerical modeling and warning procedures for Gonu Super Cyclone along Iranian Coastlines*. In: Wallendorf, L., et al. (Ed.), Proceedings of the Third COPRI Solutions to Coastal Disasters Conference. ASCE, Oahu, HI. 13–16 April 2008.

2- Dibajnia, M., Soltanpour, M., Nairn, R., Allahyar, M., (2010), In: Charabi, Y. (Ed.), *Indian Ocean Tropical Cyclones and Climate Change.* Springer. 373 pp.

3- Shah-hosseini, M., Morhange, C., Naderi Beni, A., Marriner, N., Lahijani, H., Hamzeh, M., Sabatier, F., (2011), *Coastal boulders as evidence for high-energy waves on the Iranian coast of Makran, Marine Geology*, Volume 290, Issues 1–4, Pages 17-28.

4- Fritz, H.M., Blount, C.D., Albusaidi, F.B., Al-Harthy, A.H.M., (2010), *Cyclone Gonu storm surge in Oman. Estuarine*, Coastal and Shelf Science 86, 102–106.

5- Khalilabadi, M. R. and Mansouri, D., (2013), *The effect of super cyclone "GONU" on sea level variation along Iranian coastlines*, Khalilabadi, M. R. and Mansouri, D., 2013, The effect of super cyclone "GONU" on sea level variation along Iranian coastlines, Indian Journal of Geo-Marine Science, Vol. 42(4), pp 470-475.

6- Mashhadi, L., Hajizadeh-Zaker, N., Soltanpour, M. Moghimi, S., 2013, *Numerical simulation of waves* *and storm surge induced by the Gonu Tropical Cyclone in the Chahbahar bay area.* Journal of Marine Engineering, 17, 37-50, (in Persian).

7- Hsiao, S.C., Lin, T.C., 2010, *Tsunami like solitary waves impinging and overtopping an impermeable seawall: Experimental and RANS modeling*. Coastal Engineering. 57.1-18.

8- Pham, C., Goeury, C., and Joly, A., 2016, *TELEMAC modeling syste*, TELEMAC-3D software operating manual (Rep. No. Release 7.0).

INTERNATIONAL JOURNAL OF
COASTAL & OFFSHORE ENGINEERING

IJCOE Vol.2/No. 1/Spring 2017 (43-52)

Available online at: http://ijcoe.org/browse.php?a_code=A-10-57-1&sid=1&slc_lang=en

SPH Simulation of Waves Associated with Underwater Explosion

Omid Reza Safiyari[1], Mahmood Reza Akbarpour Jannat[2*], Babak Banijamali[3]

[1] Phd student, Iranian National Institute for Oceanography and Atmospheric Science (INIOAS), Ocean Engineering and Technology Research Center, Tehran, Iran; o.r.safiyari@inio.ac.ir
[2] Corresponding author: Assistant Professor, Iranian National Institute for Oceanography and Atmospheric Science (INIOAS), Ocean Engineering and Technology Research Center, Tehran, Iran; akbarpour@inio.ac.ir*
[3] Deputy CEO of Darya Bandar Engineering Consultant Company (DBC), Tehran, Iran; banijamali.babak@gmail.com

ARTICLE INFO

Article History:
Received: 24 Aug. 2016
Accepted: 23 Apr. 2017

Keywords:
Underwater Explosion
Smoothed Particle Hydrodynamics
Graphical Processing Unit
Numerical Modeling
Explosion Generated Water Waves

ABSTRACT

The current manuscript presents the validation of Smoothed Particle Hydrodynamics (SPH) techniques for wave generation by underwater explosion, utilizing the so-called DualSPHysics numerical model. This numerical method is used to analyze generated waves which are initiated by man-made or natural explosions below free surface level of sea. In spite of the modeling limitations (e.g. absence of open boundary conditions), reasonable agreement is accomplished with predictions of the existing formula as well as experimental results. This proved that SPH techniques such as incorporated in DualSPHysics are becoming a suitable alternative to existing classical approaches to this particular water waves problem. It is also provided an inherently more accurate computational for the prediction of wave characteristics generated by underwater explosions.

1. Introduction

Underwater explosions are known to generate relatively slow, outward-moving surface waves, with certain recognizable characteristics. Such waves, originating in the volume oscillations and upward movement of the explosion-induced gas bubble breaking on the surface, eventually form a train spreading in widening circles of steadily diminishing height around the still water level. Predominantly, the first surface wave near the burst is too steep a waveform to be sustainable; consequently, it breaks into a turbulent kind of motion, dissipating a large part of the initial energy that would otherwise be available to create surface waves. Subsequently, the wave-train usually travels over deep waters almost without further loss of energy.

Past studies on waves generated by underwater explosion lead to valuable results regarding the behavior of waves and developing wave theories. Moreover, given the similarity of these waves to the waves caused by the impact of meteorites in large water bodies, exploding volcanoes and tsunamis caused by underwater landslides, therefore, by virtue of studying waves induced by controlled underwater explosions, the derived results may be similarly applicable to for the simulation of other types. Naturally, the waves produced by a downward surface elevation impulse, or via an underwater explosion, constitute a dispersive system whose properties are not constant as wave characteristics such as representative periods, celerities and wave-lengths often increase over duration of propagation and wave-heights decrease with increasing travelled distance. Various theoretical concepts have been established often rooted in analytical derivations in combination with empirical observations to characterize wave properties at a given place and time in order to achieve good conformity with measurements, however, a study of the literature points to the fact that in recent era numerical modeling tools are yet to be widely used in tackling this interesting topic. Therefore, it is strived in this article to address this issue by applying state-of-the-art numerical modeling tools for the sake of better understanding explosion created water waves as well as other waves of similar mode of generation.

A number of previous studies on underwater explosion phenomena have been performed in different related realms, such as, field experiments, laboratory investigations, analytical approaches, and numerical modeling. Generally, water waves due to underwater explosions are originated by a pulsating bubble. As a result, some researchers focused on the ensuing bubble behavior during its movements, while others worked on the stage of the bubble collapse and wave initiation, utilizing similar methodologies and assumptions which present study is more close to the last series of researches.

The first theoretical treatment of wave generated by an initial free surface disturbance of infinitely small radius, but finite energy, is due to Cauchy (1815) and Poisson (1816). An early study of considerable significance in the field of bubble research is investigation by Lord Rayleigh (1917) about collapse of a spherical cavity in an infinite fluid. The generalization of Lamb's method to a case of an initial disturbance of finite extent was developed by Terazawa (1915), for the cases of deep and intermediate water depth. Terazawa also investigated the effect of the depth of burst in the case of an impulsive explosion. Rayleigh’s idea was extended in the context of underwater explosion research by Lamb (1923) who assumed that the pressure within the explosion bubble is variable. For motion under the influence of buoyancy alone Herring (1941) first gave the system of equations describing the evolution of the explosion bubble. A numerical investigation of the generation and propagation of an underwater blast wave was undertaken by Penney (1941) and Penney and Dasgupta (1942) in which the equations of compressible flow were integrated along characteristics. Penney and Price (1942) were motivated to consider the stability of an initially spherical bubble rising under the action of buoyancy forces. The significant practical technique employed being high speed photography by Taylor and Davies (1943) and Bryant (1944), which allowed accurate records of the bubble shape as a function of time and the migration of the bubble to be obtained, with data also being recorded during collapse phase of the motion. Charlesworth (1945) performed a series of tests and studied underwater explosion effects on wave generation and propagation. Penney (1945) proposed an analytical relation for dome and crater formation during bubble collapse near free surface of water. Besides he worked on gravity waves in water caused by explosions. Bryant (1945) applied Penney’s analytical solution for test results. Herring (1949) presented a discussion of possible loss mechanisms including radiation of acoustic energy, turbulence and heat transfer and concluded that although the principal loss mechanism is via radiation [1].

Axi-symmetric solutions for explosion generated water waves was given by Kranzer and Keller (1959) in which the influence of water depth was taken into account [2]. The characteristics of explosion cavities at reduced pressure have been modeled in detail on a small scale by Kaplan and Goodale (1962). A generalization of the Cauchy-Poisson Theory to a finite disturbance of arbitrary form was developed by Le Mehaute (1963). By approximating the dispersion relationship to include only the long wave portion of the spectrum and limiting the source disturbance to a long narrow strip, Kajiura (1963) arrived at results same as Eckart’s works (1948). Applications of Kranzer and Keller analytical approach were presented by VanDorn (1964), Whalin (1965), Hwang and Divoky (1967). Theory was developed to predict the wave properties at a given travel time and distance for given source energy, displacement and travel path depth profile by Jordaan (1965). In their landmark paper Benjamin and Ellis (1966) introduce the concept of the Kelvin impulse to the study of bubble dynamics. Some researches were performed about propagation of water waves due to explosions and a sort of concepts were raised, such as VanDorn et. al (1968). They also found the behavior of explosion generated water waves on the continental shelf and its effect on costal area. Chapman (1971) employed a marker in cell technique and computed the collapse of an initially spherical vapor cavity adjacent to a rigid boundary. A theoretical mathematical model for the simulation of the hydrodynamics related to underwater explosion and subsequent bubble dynamics and free surface effects was formulated by Amsden (1973); Hirt and Rivard (1983); Fogel, et al. (1983) and Mader (1988) [1].

Bottin and outlaw (1987) prepared a class of field investigations about explosion generated waves in shallow water [3]. The vulnerability of coastal facilities and vessels to explosion generated water waves was studied experimentally by Bottin and outlaw (1988) in US army engineer waterways experiment station [4]. Wilkerson (1988) studied theoretical cavity shapes and potential flow by numerical methods. For a given experimental wave record at a defined distance from zero surface, the initial conditions are determined numerically by reverse transforms by Le Mehaute, et al. (1989), Wang, et al. (1989) and Khangaonkar and Le Mehaute (1991). Le Mehaute and Khangaonkar (1991) proposed a simple relationship for horizontal radius of the cavity when it is developed in depth of water. Wang (1992) worked on simulation of crater formation and surface movement [5].

The effects of an underwater explosion depend on several parameters, including distance from the explosion source, energy of the explosion, the depth of the explosion, and the water depth. Underwater explosions generate relatively slow, outward-moving surface waves, which have certain recognizable characteristics. These waves, originating in the oscillations of the gas bubble as it breaks the surface, eventually form a train spreading in widening circles of steadily diminishing intensity around the surface zero. Generally, the first surface wave near the burst is too steep to be sustained; consequently, it breaks into a turbulent kind of motion, consuming a large part of the initial energy that would otherwise have been available to create surface waves. Subsequently, the wave train travels over deep water often almost with no further loss of energy. Certain characteristics of surface waves become more pronounced when the detonation occurs in shallow water rather than in deep water. Field test observations showed that the first wave behaved differently from the succeeding ones; it was apparently a long, solitary wave, generated directly by the explosion, receiving its initial energy from were probably formed by the venting of the gas bubble and refilling of the cavity in the high-velocity outward motion of the water accompanying the expansion of the gas bubble. Some other tests indicated that the initial, solitary wave is characteristic of explosions in shallow water. Detonations in deep water generate a train of waves in which the number of crests and troughs increases as the train propagates outward from the center of the explosion. The properties of dispersive wave motion in the space-time field were derived for general conditions and certain practical applications. Maximum wave heights, periods, lengths, velocities, travel times, envelopes, group velocities, and the modification by a shoaling bottom can be uniquely expressed in terms of the initiating disturbance and stated by VanDorn (1964), LeMehaute (1964), Whalin (1965) and Jordaan (1964) [6].

In case of deep water or near surface explosions with low quantity of yield, after reaching bubble to the free surface region of water, sea surface started to deform into a dome shape body (see Figure 1). During this process water layer which is located on top of water become thinner and unstable until its strength be broken, so confined gas and vapor inside the bubble will be released outward. Finally the fragmented bubble will be reshaped into a crater which is surrounded by lip shape all around it (see Figure 2) [7, 8, 9, 10].

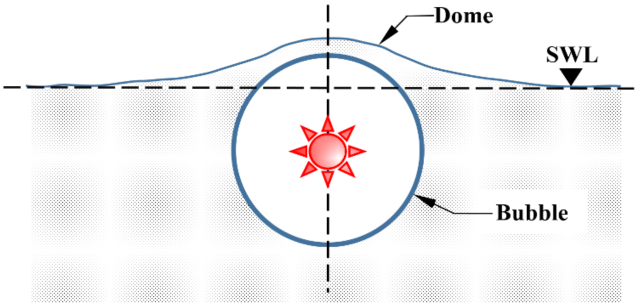

Figure 1. Rising dome due to expansion and upward migration of bubble

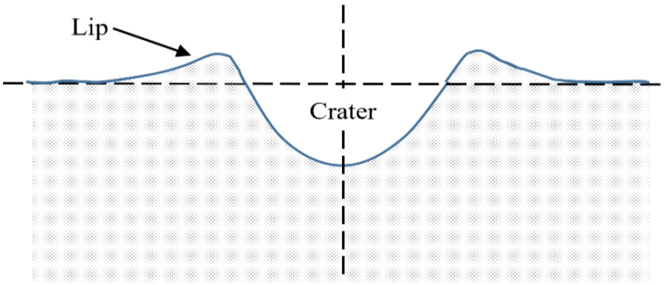

Figure 2. Generating crater and lips after bubble collapse

2. SPH numerical model

SPH is a Lagrangian method in which the continuous medium can be discretized into a set of disordered points [11]. SPH allows any function to be expressed in terms of its values at a set of the particles by interpolation without using grid to calculate spatial derivatives. In this way physical properties of each particle, such as: acceleration, density and etc. are quantified as an interpolation of the same values in neighbor nodes. The main feature of the SPH technique is to approximate a scalar function $A(\boldsymbol{r})$ at any point with r vector of position, as follows [12, 13, 14]:

$$A(\boldsymbol{r}) \cong \int A(\boldsymbol{r}').W(\boldsymbol{r}-\boldsymbol{r}',h)d\boldsymbol{r}' \qquad (1)$$

where in Eq.(1) h is called smoothing length to represent the influence of the nearest particles in a neighboring domain, so it is weighted in accordance with distance between particles. Kernel function $W(\boldsymbol{r}-\boldsymbol{r}',h)$ is used to estimate the amount of participation by means of smoothing length parameter. In discrete form Eq.(1) becomes [12, 14]:

$$\langle A(\boldsymbol{r}_a)\rangle \approx \sum_b \left(\frac{m_b}{\rho_b}\right).A(\boldsymbol{r}_b).W(\boldsymbol{r}_a-\boldsymbol{r}_b,h) \qquad (2)$$

where in Eq.(2) the summation is extended to all the particles within the neighboring distance of particle "a", and the volume associated with the particle "b" is $\frac{m_\mathrm{b}}{\rho_\mathrm{b}}$, so m_b and ρ_b are respectively the mass and the density of this neighbor particle. The kernel functions shall have several properties [12, 13], including: positivity inside the area of interaction, compact support, normalization, and monotonic decrease with distance. One kernel option is the quintic kernel described by Wendland (1995), for which the weighting function vanishes for inter-particle distances greater than $2h$. It is defined as (Altomare et. al., 2014, 2015):

$$W(q) = \alpha_D\left(1-\frac{q}{2}\right)^4(2q+1)\ ;\ 0 \le q \le 2 \qquad (3)$$

Where in Eq.(3), $q = \frac{|\boldsymbol{r}|}{h}$ is defined as ratio of particle distance to smoothing length and α_D is a normalization constant, which is equal to $\frac{7}{14\pi.h^2}$ in two dimensions and $\frac{21}{16\pi.h^3}$ in three dimensions.

The conservation laws of continuum fluid dynamics, in the form of differential equations, are transformed into their particle forms by the use of the kernel functions. The momentum equation proposed by Monaghan (1992) has been used to determine the acceleration of a particle "a" as the result of the particle interaction with its neighbors, such as particle "b" [12, 13]:

$$\frac{d\boldsymbol{v}_a}{dt} = -\sum_b m_b \left(\frac{P_b}{\rho_b^2} + \frac{P_a}{\rho_a^2} + \Pi_{ab}\right) \boldsymbol{\nabla}_a W_{ab} + \boldsymbol{g} \tag{4}$$

where $\boldsymbol{v}$ is particle velocity, P is particle pressure, $\boldsymbol{g}$ is gravitational acceleration vector equal to $(0,0,-9.81)$, and W_{ab} is the kernel function that depends on the distance between particles "a" and "b". Π_{ab} is the viscous term according to the artificial viscosity proposed by Monaghan (1992) [12, 13]:

$$\Pi_{ab} = \begin{cases} -\frac{\alpha_v \cdot \bar{c}_{ab} \cdot \mu_{ab}}{\bar{\rho}_{ab}} & ; \ \boldsymbol{v}_{ab} \cdot \boldsymbol{r}_{ab} < 0 \\ 0 & ; \ \boldsymbol{v}_{ab} \cdot \boldsymbol{r}_{ab} \geq 0 \end{cases} \tag{5}$$

where $\boldsymbol{r}_{\mathrm{ab}} = \boldsymbol{r}_{\mathrm{a}} - \boldsymbol{r}_{\mathrm{b}}$, $\boldsymbol{v}_{\mathrm{ab}} = \boldsymbol{v}_{\mathrm{a}} - \boldsymbol{v}_{\mathrm{b}}$; which are the particle position and velocity, respectively. α_v is a coefficient that needs to be tuned in order to introduce the proper dissipation. The value $\alpha_v = 0.01$ was used in this work because it is the minimum value that prevents instability and spurious oscillations in the numerical scheme. $\bar{c}_{\mathrm{ab}} = \frac{c_{\mathrm{a}} + c_{\mathrm{b}}}{2}$ is the mean speed of sound of particles, $\bar{\rho}_{\mathrm{ab}} = \frac{\rho_{\mathrm{a}} + \rho_{\mathrm{b}}}{2}$ is the mean density of particles and $\mu_{\mathrm{ab}} = \frac{h \cdot \boldsymbol{v}_{\mathrm{ab}} \cdot \boldsymbol{r}_{\mathrm{ab}}}{\boldsymbol{r}_{\mathrm{ab}} \cdot \boldsymbol{r}_{\mathrm{ab}} + \eta^2}$ with $\eta^2 = 0.01 \times h^2$.

Equation of states for ideal gases is as follow [12, 13, 14]:

$$P = B\left[\left(\frac{\rho}{\rho_0}\right)^{\gamma} - 1\right] \tag{6}$$

$$B = \frac{c_0^2 \cdot \rho_0}{\gamma} \tag{7}$$

$$c_0 = c(\rho_0) = \sqrt{\frac{\partial P}{\partial \rho}}\bigg|_{\rho_0} \tag{8}$$

the parameter B is a constant related to the fluid compressibility modulus, $\rho_0 = 1000\,\mathrm{kg/m^3}$ is the reference density, chosen as the density at the free surface, γ is a constant, normally between 1 and 7, and c_0 is the speed of sound at the reference density [14].

3. Present Approach

In this study, it is aimed to simulate the initiation and primary wave propagation via underwater explosion phenomena partaking of the SPH method. Results of the adopted SPH model were compared with some of well-known experimental, analytical and numerical studies, focusing on the primary wave formation after cavity collapse and wave propagation aspects.

It is intended to investigate of the flow after the cavity in the free surface reaches its maximum dimensions, assuming that the flow is single phase type, neglecting any two-phase flow effects, as well as that the surrounding fluid is deemed approximately at rest at the time of reaching the maximum bubble radius [15].

As stated in user manual of the DualSPHysics code [16], it has been developed starting from the SPH formulation implemented in SPHysics [17]. This FORTRAN code is robust and reliable but is not properly optimized for huge simulations [18, 19]. DualSPHysics is implemented in C++ and CUDA language to carry out simulations on the CPU and GPU respectively [20]. Furthermore, better approaches are implemented, for example particles are reordered to give faster access to memory, symmetry is considered in the force computation to reduce the number of particle interactions and the best approach to create the neighbor list is implemented [21]. The CUDA language manages the parallel execution of threads on the GPUs. The best approaches were considered to be implemented as an extension of the C++ code, so the most appropriate optimizations to parallelize particle interaction on GPU were implemented [22]. The DualSPHysics code has been developed to simulate real-life engineering problems using SPH models such as the computation of forces exerted by large waves on the urban furniture of a realistic promenade [14] or the study of the run-up in an existing armour block sea breakwater and wave forces on coastal structures [12, 13].

The main purpose of the present study is to investigate the precision of SPH-type methods for computing water waves generated by underwater explosion occurrences. Hence, some new modeling test cases were compared with analytical-rooted solutions proposed in the literature, and with experimental data as well as traditional numerical modeling results.

DualSPHysics version 3.1 (2013) is used in the current study, requiring hardware with run of a Central Processing Unit (CPU) or a Graphical Processing Unit (GPU) in addition. The computational efficiency offered by the GPU has made high performance computing more readily available for computational fluid dynamics applications, especially in the case of very large modeling domains.

Two types of GPU cards on different machines were used in current study. Applied machines and processors are as following: (1) GeForce GTX 680 with 1536 CUDA cores on a personal computer with a CPU type of AMD A8-3870 APU, (2) GeForce GTX 780M with 1536 CUDA cores on a MSI laptop which has CPU type of Intel® Core™ i7-4700MQ.

4. Comparison of simulation results with existing analytical and empirical solutions

Before application of the code for field tests, appropriate justification of the DualSPHysics was required to clarify that the numerical model could reliably simulate free surface shock propagation phenomena due to predefined initial condition [23]. Thus, several recognized analytical solved problems were simulated, so the generated wave shapes and behavior of propagated waves due to initial crater of underwater explosion were monitored. Finally the results were compared with those are described in reference works and literature. There are too many theories and formulae about underwater explosion waves, so in this study the Penney's (19450 theoretical relations [24], Charlesworth (1945) experimental results [25] and Mader (1976) numerical experiences [26], were considered as case studies.

4.1. Charlesworth's experimental setup

One of the experiences in a field-laboratory environment was performed by Charlesworth (1945) at the Road Research Laboratory, London [25]. A complete description of the experimental definition and set of outputs were provided by him. This field test was an underwater explosion experiment within a semi rectangular bay, which was limited by banks in west and south directions respectively 55 ft (16.76 meter) and 70 ft (21.34 meter) from surface zero. Water depth was approximately uniform, from 15 to 18 ft (4.57 to 5.49 meter), all around the charge location (see Figure 3). Charge depth locations and weights were considered variable. Wave amplitudes in specified locations were captured by a camera on south bank.

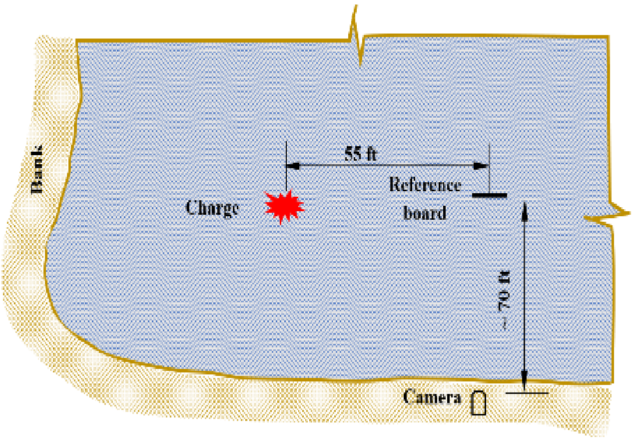

Figure 3. Site plan of underwater explosion tests (Charlesworth, 1945)

In this study, the recorded amplitudes of surface waves produced by a 32 lb (14.5 kg) charge detonated in water at a depth of 8 ft (2.44 meter) which was recorded for point at 56.5 ft (17.22 meter) from the charge, were considered for evaluation of SPH modeling.

4.2. Penney's analytical solution

Analytical solution proposed by Penney (1945) for initial condition of cavity formation due to underwater explosion [24], especially in deep water, was examined by Bryant (1945) for last mentioned experiment by Charlesworth (1945) [25]. The same three dimensional SPH model was applied for comparison of results (see Table1). In this case both initial conditions, Penney's theory and modified Penney's curve as described by Bryant (1945), were tested in simulations.

Table 1. SPH-3D model parameters of the simulation of Charlesworth's experiment and Penney's analytical solution by bryant

Characteristic	Value
Particle size	0.2 ~ 0.5 [*m*]
Smoothing length	0.015 [*m*]
Number of particles	1,000,000 ~ 3,700,000 [-]
Artificial viscosity	0.01~0.5 [-]
Speed of sound coefficient	10 ~ 20 [-]
CFL number	0.2 [-]
Kernel function type	Wendland [-]

4.3. Mader's numerical experiences

As mentioned before, some researchers tried to model underwater explosion and its effects such as surface water waves. One of this kind of researches, is numerical simulations of waves generated from surface cavities by Mader (1976) [26]. Mader applied two reference numerical model, SWAN and ZUNI, for simulation purposes in his works [26]. Here the results of Mader were used for re-assessing the primary wave generation from cavity formation of underwater explosion phenomenon. Mader studied the wave motion resulting from cavities in the ocean surface, using both the long wave, shallow water model and the incompressible Navier-Stokes equations. He found that the fluid flow resulting from the calculated collapse of the cavities is significantly different for the two models. Also he supposed that the experimentally observed flow resulting from explosively formed cavities is in better agreement with the flow calculated using the incompressible Navier-Stokes model.

4.4. Prins' experimental setup

In this section SPH modeling results are also compared with the experimental data provided by J.E. Prins (1956) at Wave Research Laboratory of the Institute of Engineering Research, University of California, Berkeley [27, 28]. The model investigations were carried out in a flume one foot wide by sixty foot long. In this experimental research water depression was created by an air-tight box of Plexiglas with a sliding front wall in which the water level could be elevated or depressed by means of a decreased/increased pressure in the air compartment. By pulling the slide upward in the shortest possible time it was possible to develop a free elevated or depressed area of uniform height with all the water particles effectively at rest. The back wall of the box was considered to cause a total reflection and hence is the axis of symmetry of the system. At the opposite end of the channel a wave absorber was installed. The vertical movement of the water surface, η, was recorded as a function of time simultaneously at five places along the channel with a six-channel recorder by using parallel wire resistance wave gages [27, 28]. The test results with water depth d=2.3 ft (0.7 meter), upward initial bore Q=0.4 ft (0.12 meter) by a length of L=2 ft (0.61 meter) were considered for modeling purposes. Recorded wave profile at X=15 ft (4.57 meter).

5. Results and discussions

This section shows the capability of the SPH method, the DualSPHysics code in particular, to simulate collapse of initial cavity and primary wave domain due to underwater explosion.

The process of numerical simulation of fluid particles, during initiation of primary wave shapes and their radial propagation from surface zero towards all directions, is related on the physical properties at each SPH particle and its interaction with other ones. The wave shapes can be numerically measured by wave gauges in specified locations or by free surface waterline calculations. These techniques were applied in following simulation test cases to assess the results with experimental, analytical or numerical experiences by others.

Prior to applying DualSphyics to model experimental and numerical cases, a simple wave propagation due to free water surface initial condition deformation was tested and wave shapes were monitored qualitatively. In this numerical test, wave forms were originated and propagated very smooth. The effects of variation of different parameters were checked and found that the most critical parameter in this type of hydrodynamic problem is particle sizes. For very large or very small sizes of particles, the waves were dissipated or damped very quickly due to low accuracy in very large sizes and numerical viscosity effects in very small sizes. Finally it has been proven that for a good behavior of numerical model, it is better that the optimum size of particles to be considered in the range of 1/10 to 1/1000 of largest dimension in 3D simulations and 1/1000 to 1/100000 of largest dimension in 2D models. Also it is found that in vertical direction at least 5 to 10 particle is required. The primary wave formation and propagation is shown in Figure 4.

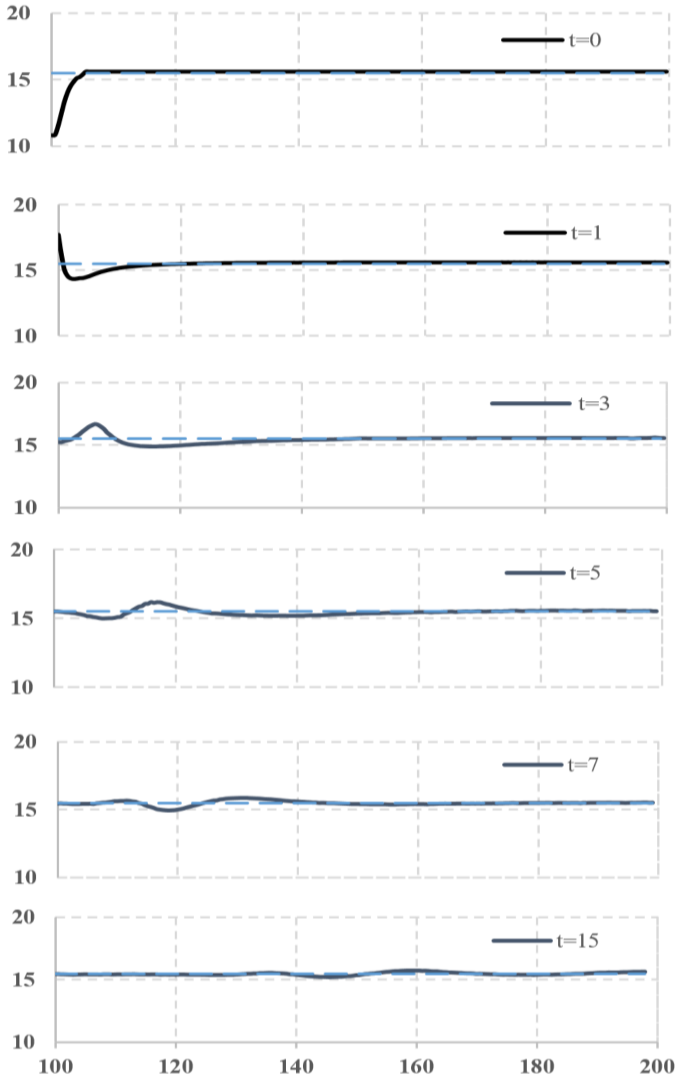

Figure 4. Primary wave generation and propagation due to underwater explosion (times in seconds, distances in meters)

3D presentation of dome evolution in time and primary wave propagation mechanism in Figure 5a, also velocity components in X, Y and Z directions are quoted respectively in Figures 5b to 5d. Two instant of the SPH simulation using DualSPHysics is depicted in Figure 6. Different numerical parameters related to the number of particles and 3D-SPH simulations are summarized in Table 1. A good agreement between experimental and SPH results are presented in Figure 6. Both trends are definitely compatible and besides three peaks are approximately simulated with a shift in time of occurrence which become greater from first crest in curve to the third one (see Figure 6).

Experimental measurements included the time series of the wave amplitudes. These experimental data were also used by Bryant (1945) to validate the Penney's theoretical formula for initiation of water waves and cavity formation. The initial surface condition was considered to be parabolic with the characteristics that are specified in Bryant's work (1945) for both SPH models of Charleston and Penney [28].

Various types of two dimensional SPH models were prepared for these samples, so their simulation parameters are similar to last SPH modeling case that is presented in Table 1.

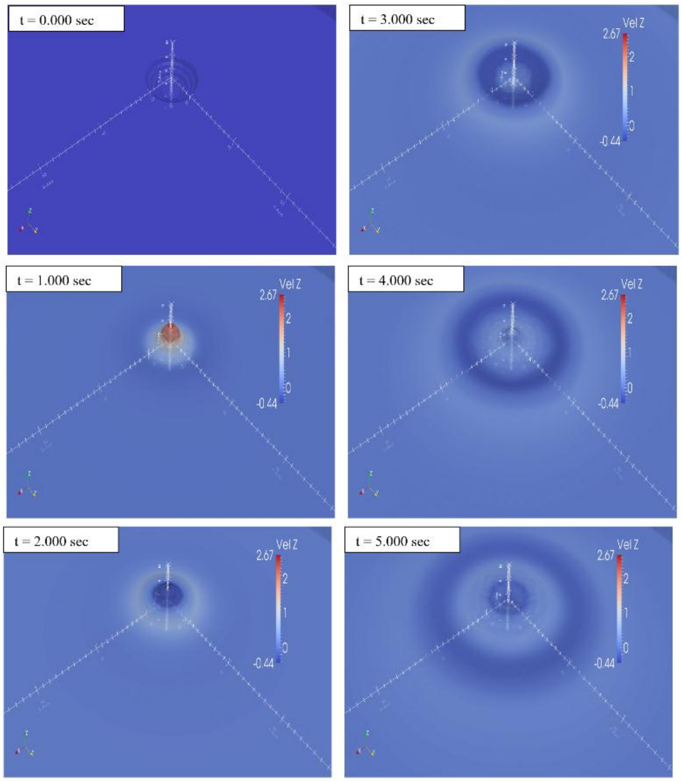

Figure 5a. Time evolution of dome shape and primary wave propagation with vertical velocity contours

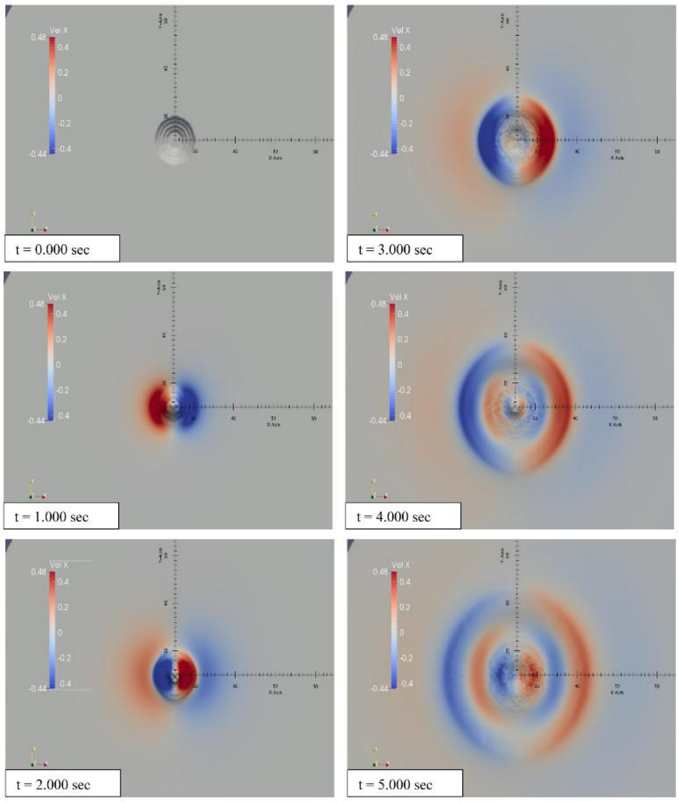

Figure 5b. Time evolution of velocity X-component contours

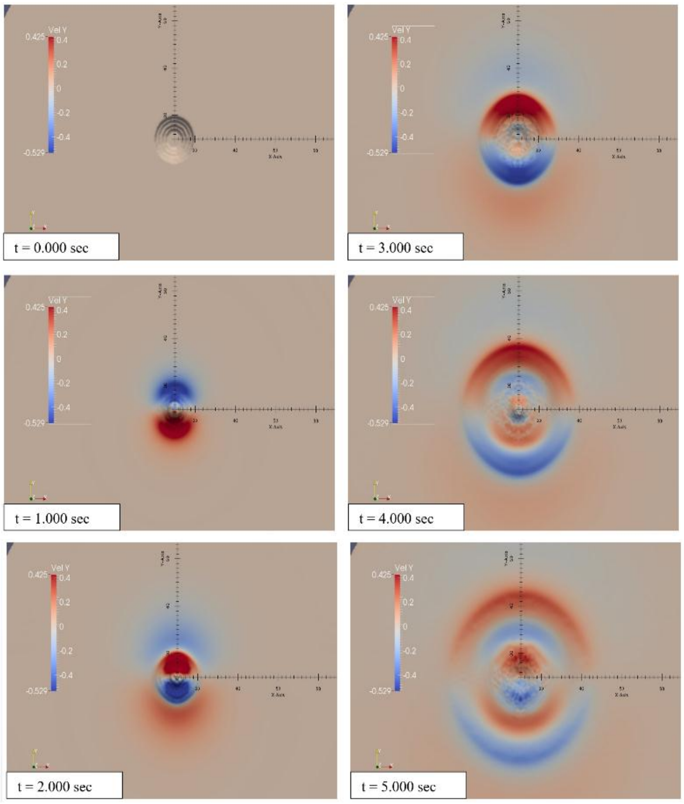

Figure 5c. Time evolution of velocity Y-component contours

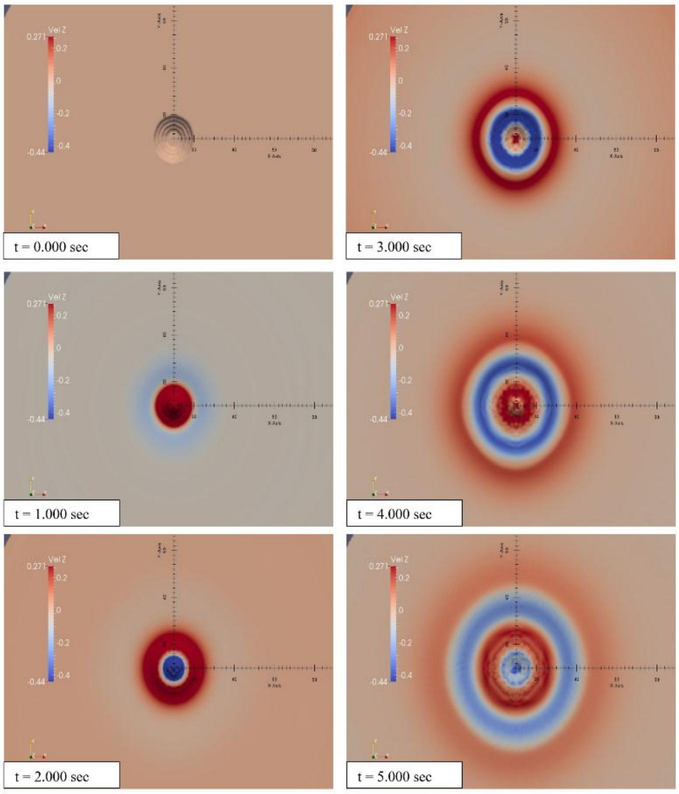

Figure 5d. Time evolution of velocity Z-component contours

Such as last numerical experience in present work, there is reasonable agreement between the two curves (see Figure 7).Results of SPH are shown in Figure 8 for SWAN modeling and also Figure 9 for simulations by ZUNI respectively. SPH model properties of these series are quoted in Table 2.

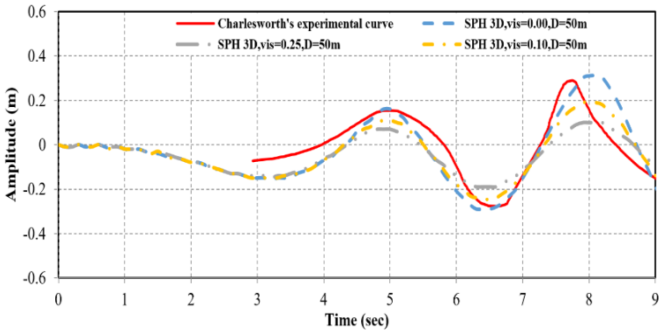

Figure 6. Comparison of Charlesworth's experimental data with SPH results

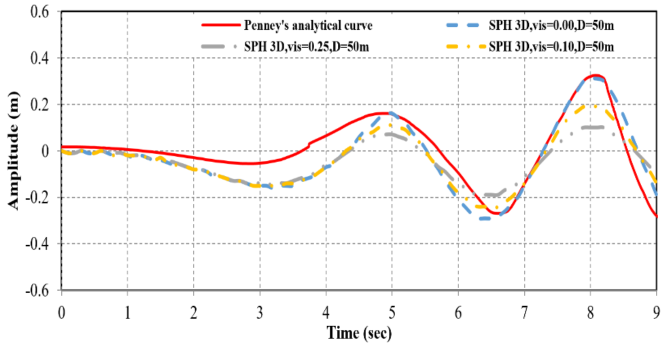

Figure 7. Comparison of Penney's analytical solution with SPH results

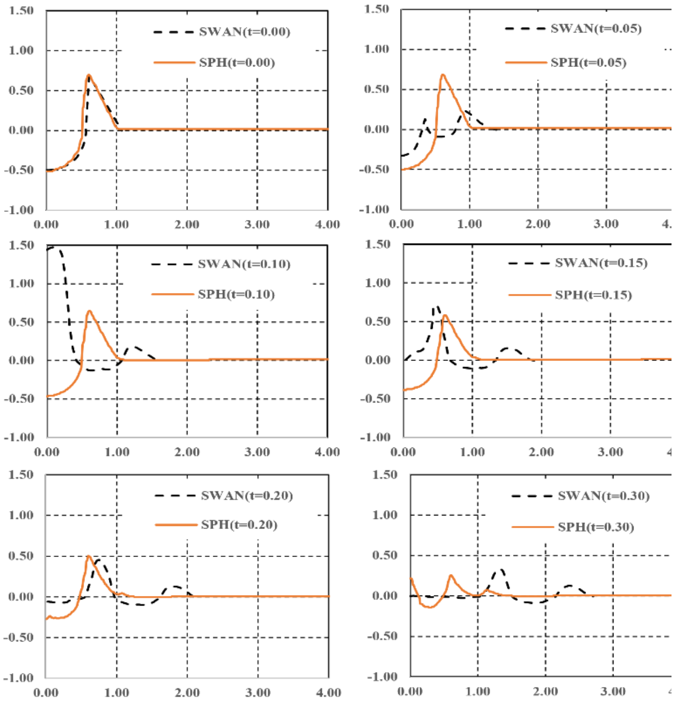

Figure 8. Comparison of SWAN modeling wave generation and propagation due to initial crater (Mader, 1976) with SPH results (Current study) in different time steps

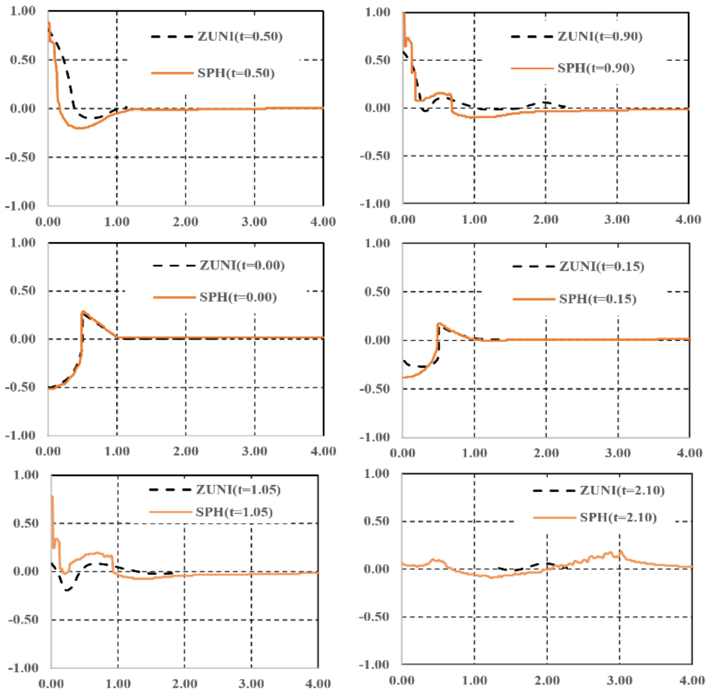

Figure 9. Comparison of ZUNI modeling wave generation and propagation due to initial crater (Mader, 1976) with SPH results (Current study) in different time steps

Table 2. SPH-2D model parameters of the simulation of Mader's numerical experiment

Characteristic	Value
Particle size	0.01 ~ 0.05 [m]
Smoothing length	0.015 [m]
Number of particles	20,000 ~ 100,000 [-]
Artificial viscosity	0.01~0.5 [-]
Speed of sound coefficient	10 ~ 20 [-]
CFL number	0.2 [-]
Kernel function type	Wendland [-]

It is important to note that wave shapes are very similar but a slight time shift in wave propagation is visible. Water levels and especially geometry of primary wave are approximately simulated by SPH technique. A series of two dimensional SPH models of Prins's tests were built, which their simulation properties are presented in Table 3.

Table 3. SPH-2D model parameters of the simulation of Prins's laboratory experiment

Characteristic	Value
Particle size	0.0006096 ~ 0.01016 [*m*]
Smoothing length	0.0015 [*m*]
Number of particles	130,000 ~ 365,000 [-]
Artificial viscosity	0.01~0.5 [-]
Speed of sound coefficient	10 ~ 20 [-]
CFL number	0.2 [-]
Kernel function type	Wendland [-]

Results of 2D-SPH modeling are shown in Figure 10 for these experiments. Obviously the location and peak values of wave time histories in SPH models are very close to experimental results.

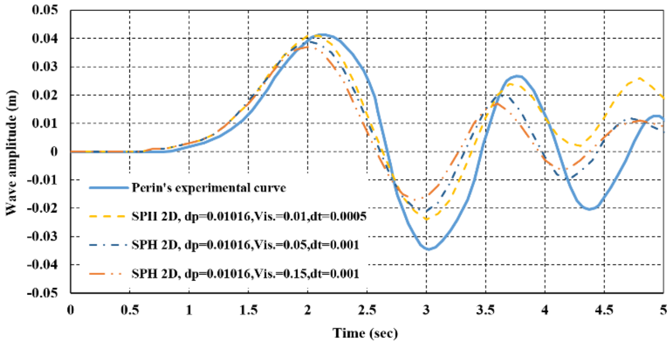

Figure 10. Comparison of SPH results with Prins' experimental record (1956) at X=15 ft

6. Conclusions

Generation of first leading wave of a cavity type initial condition on free surface of sea water line, is a typical shock wave that is very high and unstable due to its extra ordinary steepness. Most of the time this primary wave is the largest and strongest wave among other wave in a trail of underwater explosion surface waves. Prediction leading wave and calculation of its properties, is important for design of coastal and marine structures that are located in the effective domain of leading wave. Smoothed Particle Hydrodynamics, is a proper numerical method for prediction of turbulent and harsh condition of surface water waves. In this research it is found that:

SPH model can predict first two or three leading waves. It is seen than SPH model prediction has good agreement with experimental or field records (see Figures 6 & 10).

SPH results are more compatible with Eulerian models which are constructed on the basis of Navier-Stocks equations such as ZUNI model (see Figure 9). Obviously shallow water models such as SWAN has not capability of underwater explosion wave generation by free surface initial conditions and results are not compatible. Even in this case the general trend of wave initiation and propagation are the same but they are not match from scale and shape point of view (see Figure 8).

SPH model results has shorter wave crest prediction vs. analytical and other numerical models. This difference is raised from discrete nature of SPH and splash of particles especially in contact moments when some parts of fluid particles coincide with other particles or rigid walls. In these cases, some parts of fluids are separated from the whole body and will drop again in another place with impact. This may cause some extra wave generation or damping of main wave bodies, so the results shows shorter wave heights than other techniques.

The main difference between analytical and traditional numerical models with SPH models is discrete behavior of the last one. This property make it more suitable for modeling of shock phenomena. For instance when initial cavity form of water surface started to collapse, it is very hard for traditional models that simulate mixing multiple layers of fluids, but it is simulate inherently by SPH method.

The major weak point of SPH is its lower accuracy vs. traditional CFD tools, then it may enforce user to create a fine size of particle and cause to larger computational times. On the other hand, by use of coarse size of particles, it is possible to find the main trend of surface waves of underwater explosion phenomenon.

7. Acknowledgements

Funding for this research was provided by the Iranian National Center for Ocean Hazards (INCOH), affiliated to Iranian National Institute for Oceanography and Atmospheric Science (INIOAS). The authors appreciate from this support.

8. References

1- www.DTIC.mil, Official site of Defense Technical Information Center.

2- Kranzer, H.C. and Keller, J.B., (1959), *Water Waves Produced by Explosions*, AIP Publishing, Journal of Applied Physics, Vol.(3), p. 398.

3- Falade, A. and Holt, M., (1978), *Surface waves generated by shallow underwater explosions*, AIP Publishing, Physics of Fluids, Vol. 21(10), p. 1709.

4- Bottin, R.R., (1990), *Impulsive waves generated by falling weights in shallow water*, Final Technical Report CERC-90-9, Coastal Engineering Research Center, DEPARTMENT OF THE ARMY, Waterways Experiment Station, Corps of Engineers, 3909 Halls Ferry Road, Vicksburg, Mississippi 39180-6199.

5- LeMehaute, B. and Wang, S., (1996), *Water waves generated by underwater explosion*, World Scientific, River Edge.

6- Whalin, R.W., (1965), *Water waves produced by underwater explosions: propagation theory for regions near the explosion*, Journal of Geophysical Research, Vol.70(22), p. 5541-5549.

7- Kolsky, H., Lewis, J.P., Sampson, M.T., Shearman, A.C. and Snow, C.I., (1949), *Splashes from Underwater Explosions*, Proceeding of Royal Society of London, Vol. 196, p. 379-402.

8- Kirkwood, J.G. and Seeger, R.J., (1950), *Surface waves from an underwater explosion*, Underwater Explosion Research, Vol. II, ONR, Dept. of Navy, p. 707-760.

9- Fuchs, R.A., (1952), *Theory of surface waves produced by underwater explosions*,Technical Report Series No. 3, Issue No. 335, University of California, Institute of Engineering Research, Berkeley, California.

10- Kozachenko, L.S. and Khristoforov, B.D., (1972), *Surface events during underwater explosions*, Translated from Fizika Goreniya i Vzryva, Vol. 8(3), p. 433-438.

11- Crespo, A.J.C., Altomare, C., Dominguez, J.M., Suzuki, T., Verwaest, T. and Gomez-Gesteira, M., (2015), *SPH modeling in coastal engineering*, E-proceedings of the 36th IAHR World Congress, Hague, The Netherlands.

12- Altomare, C., Crespo, A.J.C., Rogers, B.D., Dominguez, J.M., Gironella, X. and Gomez-Gesteira, M., (2014), *Numerical modelling of armour block sea breakwater with smoothed particle hydrodynamics*, Computers & Structures, Vol. 130, p. 34-45.

13- Altomare, C., Crespo, A.J.C., Dominguez, J.M., Gomez-Gesteira, M., Suzuki, T. and Verwaest, T., (2015), *Applicability of Smoothed Particle Hydrodynamics for estimation of sea wave impact on coastal structures*, Coastal Engineering Journal, Vol. 96, p. 1-12.

14- Barreiro, A., Crespo, A.J.C., Domínguez, J.M. and Gómez-Gesteira, M., (2013), *Smoothed Particle Hydrodynamics for coastal engineering problems*, Computers & Structures Vol. 120, p. 96-106.

15- Swegle, J.W. and Attaway, S.W., (1995), *On the feasibility of using smoothed particle hydrodynamics for underwater explosion calculations*, Comp. Mech. Vol. 17, p. 151-168.

16- Crespo, A.J.C., Domínguez, J.M., Gómez-Gesteira, M., Barreiro, A., Rogers, B.D., Longshaw, S., Canelas, R. and Vacondio, R., (2013), *User Guide for DualSPHysics v3.0*.

17- www.SPHysics.org, Official site of SPHysics software.

18- Gomez-Gesteira, M., Rogers, B.D., Crespo, A.J.C., Dalrymple, R.A., Narayanaswamy, M. and Dominguez, J.M., (2012), *SPHysics - development of a free-surface fluid solver – Part 1: Theory and formulations*, Computers & Geosciences Vol. 48, p. 289-299.

19- Gomez-Gesteira, M., Rogers, B.D., Crespo, A.J.C., Dalrymple, R.A., Narayanaswamy, M. and Dominguez, J.M., (2012), *SPHysics - development of a free-surface fluid solver – Part 2: Efficiency and test cases*, Computers & Geosciences Vol. 48, p. 300-307.

20- www.dual.SPHysics.org, Official site of DualSPHysics software.

21- Domínguez, J.M., Crespo, A.J.C., Gómez-Gesteira, M. and Marongiu, J.C., (2011), *Neighbour lists in Smoothed Particle Hydrodynamics*, International Journal for Numerical Methods in Fluids, Vol. 67(12), p. 2026-2042.

22- Domínguez, J.M., Crespo, A.J.C. and Gómez-Gesteira, M., (2013), *Optimization strategies for CPU and GPU implementations of a smoothed particle hydrodynamics method*, Computer Physics Communications, Vol. 184(3), p. 617-627.

23- Monaghan, J.J. and Gingold, R.A., (1983), *Shock simulation by the particle method SPH*, Journal of computational Physics, Vol. 52, p. 374-389.

24- Penney, W.G., (1950), *Gravity waves produced by surface and underwater explosions*, Underwater Explosion Research, Vol. II-The gas globe, Office of Naval Research, Department of the Navy, p. 679-700.

25- Bryant, A.R., (1950), *Surface waves produced by underwater explosions Comparison of the theory of W.G. Penney with experimental results for a 32-lb. charge*, Underwater Explosion Research, Vol. II, ONR, Dept. of Navy, p. 701-706.

26- Mader, C.L., (1976), *Calculations of waves formed from surface cavities*, Proc. of 15th Conf. on Coastal Engineering, Vol. 15, p. 1079-1092.

27- Prins, J.E., (1957), *Water waves due to a local disturbance*, Proc. of 6th Conf. on Coastal Engineering, Vol. 6, p. 147-162.

28- Noda, E.K., (1971), *Water waves generated by a local surface disturbance*, Journal of Geophysical Research Vol. 76, p. 7389-7400.